Elastocapillarity:
Adhesion and Large Deformations of Thin Sheets

Till Jakob Wenzel Wagner

Gonville & Caius College

A dissertation submitted to the University of Cambridge
for the degree of Doctor of Philosophy

January 2013

For my parents

Preface

The research described in this thesis was performed in the Polar Ocean Physics Group, Department of Applied Mathematics and Theoretical Physics at the University of Cambridge between October 2009 and November 2012 and was supervised by Professor Peter Wadhams. Much of the research presented was conducted under guidance by Doctor Dominic Vella (formerly of DAMTP, now at Oxford University). No part of this thesis has been submitted for any qualification other than the degree of Doctor of Philosophy at the University of Cambridge.

This thesis is the result of my own work and includes nothing which is the outcome of work done in collaboration, except where specifically indicated in the text and acknowledgements.

The work described in this thesis is believed to be original, except where reference is made to the work of others. In particular, section 1.3 constitutes largely review material.

Cambridge, January 2013

Acknowledgements

First, I must express my gratitude to my supervisor Peter Wadhams, for giving me the opportunity of pursuing a Ph.D. and his continued support over the past three years.

Next, to Dominic Vella, who, it seems, has taught me everything I know.

I would like to thank Anthony Anderson for many insightful discussions, for a great number of enjoyable lunchtimes and for helpful comments on a draft version of this thesis. Thanks also go to John Fletcher, the best office mate I could have hoped for and to the other members of the Polar Ocean Physics Group, Nick Toberg and Joao Rodriguez, for many interesting and helpful conversations. I further want to express my gratitude to Grae Worster for feedback and support throughout.

I would also like to thank the many people I have worked with on sea ice matters, in particular Ted Maksym, Jeremy Wilkinson and Hanumant Singh, for great field trips and tense games of scrabble.

Away from work, I am forever indebted to my parents and my sister, Lena, who have always been there for me. And I would like to thank my friends, in Germany, England and elsewhere, for believing in me and making every break from work so rewarding – in particular my housemates Annika, Simon and Kate who had to put up with me the past few months.

Financial support from EPSRC, DAMTP, Gonville & Caius College and the Cambridge Philosophical Society are gratefully acknowledged.

Abstract

This thesis is concerned with the deformation and adhesion of thin elastic sheets that come into contact with an underlying substrate. The focus of this work is on the interplay between material and geometric properties of a system and how this interplay determines the equilibrium states of sheet and substrate, particularly in the regime of geometrically nonlinear deformations.

We first consider the form of an elastic sheet that is partially adhered to a rigid substrate, accounting for deflections with large slope: the Sticky Elastica. Starting from the classical Euler Elastica we provide numerical results for the profiles of such blisters and present asymptotic expressions that go beyond the previously known, linear, approximations. Our theoretical predictions are confirmed by desktop experiments and suggest a new method for the measurement of material properties for systems undergoing large deformations.

With the aim to gain better understanding of the initial appearance of blisters we next investigate the deformation of a thin elastic sheet floating on a liquid surface. We show that, after the appearance of initial wrinkles, the sheet delaminates from the liquid over a finite region at a critical compression, forming a delamination blister. We determine the initial blister size and the evolution of blister size with continuing compression before verifying our theoretical results with experiments at a macroscopic scale.

We next study theoretically the deposition of thin sheets onto a grooved substrate, in the context of graphene adhesion. We develop a model to understand the equilibrium of the sheet allowing for partial conformation of sheet to substrate. This model gives physical insight into recent observations of 'snap-through' from flat to conforming states and emphasises the crucial role of substrate shape in determining the nature of this transition.

We finally present a theoretical investigation of stiction in nanoscale electromechanical contact switches. Our model captures the elastic bending of the switch in response to both electrostatic and van der Waals forces and accounts for geometrically nonlinear deflections. We solve the resulting equations numerically to study how a cantilever beam adheres to a fixed bottom electrode: transitions between free, pinned and clamped states are shown to be discontinuous and to exhibit significant hysteresis. The implications for nanoscale switch design are discussed.

Summary of Frequently Used Quantities

Variable	Meaning	Definition
γ_{AB}	surface energy per unit length	(1.11), (2.5), fig 2.3
$\Delta\gamma$	strength of adhesion per unit length	(1.12)
δ	blister height *	(2.10)
	draft of floating sheet *	(3.6)
	substrate groove height	fig 4.1
	switch height	fig 5.1
ϵ_0	permittivity of free space	
ψ	applied voltage *	(5.7)
λ	blister width *	(2.10)
	point of delamination	fig 4.1, fig 5.1
ν	Poisson ratio	
θ	tangent angle of arc-length	fig 2.2, fig 3.2
θ_0	maximum tangent angle	fig 2.2
ρ	density of sheet or beam	
ρ_l	density of liquid	
ρ_s	density of substrate	
τ	in-plane stress in sheet *	(2.10), (3.23)
η	vertical stress in sheet *	(5.7)
Γ	strength of adhesion *	(3.12), (4.6)
b	width of blister on liquid	fig 3.2
d	blister height	fig 2.2
	switch height *	(5.6)
g	acceleration due to gravity	
h	sheet/beam thickness	
ℓ	blister width	fig 2.2
ℓ_{ec}	elastocapillary length	(1.18)
ℓ_w	wrinkling length	(3.4)
l	length of sheet or beam	fig 2.3, fig 5.1
l_b	arc-length of blister	fig 2.2
Δl	horizontal compression	fig 2.2, fig 3.2, (3.2)
m	mass per unit length	
s	arc-length	
w	height profile of blister/switch	fig 3.2, fig 4.1
w_s	substrate surface profile	fig 4.1
w^*	van der Waals radius	(1.9)

Variable	Meaning	Definition
A_{H}	Hamaker constant	(1.8)
B	width of blister on liquid *	(3.5)
$\mathcal{B}$	Bending stiffness	(2.2)
E	Young's modulus	
H	sheet/beam thickness *	(4.10)
L	sheet/beam length *	(2.10)
L_b	length of blister *	(3.5)
ΔL	horizontal compression *	(2.6)
S	arc-length *	
R	typical radius of curvature *	(4.6)
T	in-plane stress in sheet	(2.7)
U	free energy	(2.1), (3.11), (4.3)
$\mathcal{U}$	free energy *	
V	applied voltage	fig 5.1
W	height profile *	(2.20)
W_S	substrate surface profile *	fig 4.3 – 4.5
Y	sheet–substrate distance *	(4.10)

* denotes dimensionless quantities

Contents

Chapter 1

Introduction

1.1. Motivation

Thin sheets surround us: flags flying in the wind, paper posters on a wall, protective screens on our smartphones. Their sizes range from the tiniest cell membranes to the icy crust that covers Jupiter's moon Europa. And as varied as the scales they cover are their physical properties: thin sheets can be made of materials that are brittle or flexible, stiff or soft, elastic or viscous. Because of their ubiquity and their countless different guises, thin sheets are studied by scientists of almost every description; by biologists and geophysicists, by engineers and mathematicians.

A thin sheet as such, in its unstressed state, is not particularly interesting – it is, almost by definition, simply straight and flat. But the instant that a force acts on it, a multitude of different phenomena can unfold: under stress, rubber sheets can stretch or bend, paper will crumple and fold, metal beams and even continental plates will flex and buckle, skin can wrinkle, crease or blister (see figure 1.1).

Inspired by nature and spurred on by technological applications, scientific interest in these phenomena has increased significantly over the last decade. They are linked to many fields of research – ranging from the flexure of the earth's lithosphere in plate tectonics (Brotchie & Silvester, 1969; Ribe, 2009; Greve & Blatter, 2009) to the bending of electric

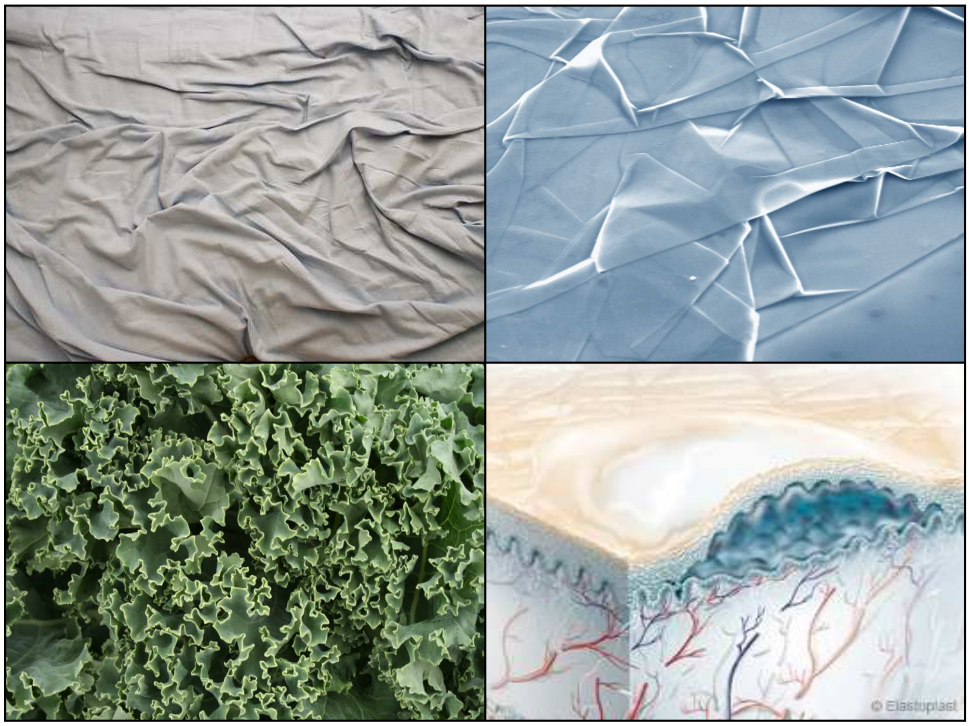

Figure 1.1.: Free and adhered sheets in different states of deformation, clockwise from top left: creased bed sheets, crumpled graphene, graphic of blistered skin (with wrinkles at the interface), curly kale.

devices in nano-scale technologies, (Sun *et al.*, 2006; Jiang *et al.*, 2007*b*; Rogers *et al.*, 2010) from bio-medical applications (Diamant *et al.*, 2001) to the art of origami (Conti & Maggi, 2008; Balkcom & Mason, 2008; Hawkes *et al.*, 2010).

In this thesis we study how thin elastic sheets deform, and in particular, how they respond to adhesive interactions. The study of deformed sheets can be split up into (a) systems of free sheets (such as the wrinkling of leaves) and (b) sheets that are in contact with a substrate. A sheet can be fully in contact with its substrate, such as a smoothly laid out bathmat, or it can be partially detached, like a carelessly placed sticker. Contact can either be imposed upon the system by external forces (such as gravity in the example of a bathmat) or may be due to adhesion between the sheet and the substrate, where minimizing the surface energies determines the state of a system. This thesis is concerned with the latter: the question of how thin elastic sheets partially or fully adhere to a substrate and how this adhesion is governed by the interplay of material and geometric properties of the system.

Adhesive interactions are becoming increasingly important in technological applications. In many applications, such as paint coatings on cars or protective films on smartphone screens, flawless adhesion is highly desired. In other applications, adhesion may instead

be a hindrance, for example in small scale electromechanical systems where irreversible stiction causes devices to fail. In a third range of applications, scientists strive to integrate reversible transitions between adhered and de-adhered states into their systems. An example of this is flexible electronics, where the intentional delamination of electric circuits extends the range of deformation that a device can experience without failure. Some examples of such applications are shown in figure 1.2.

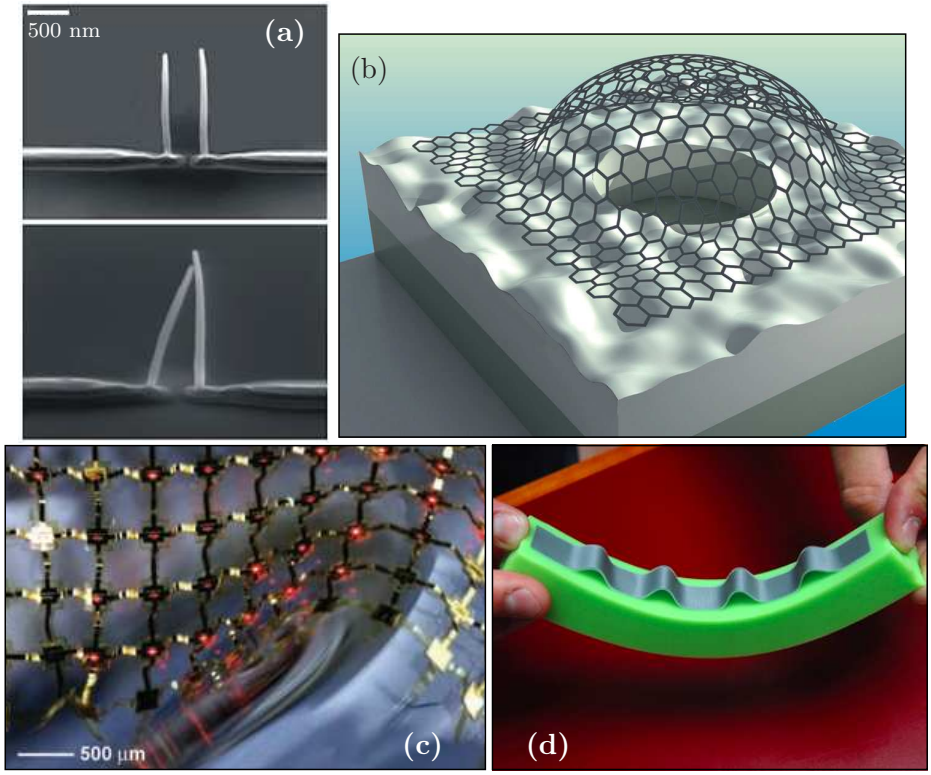

Figure 1.2.: Adhesion of thin elastic sheets in different experimental settings: (a) undeflected (top) and 'pinned' (bottom) states of a nanoelectromechanical contact switch (Lundgren, 2012), (b) partial delamination in a pressurized 'graphene blister test' (Huang, 2011), (c) buckling of electric circuit micro-ribbons (Park *et al.*, 2009), (d) macroscale delamination blisters due to a mismatch in the elastic response between sheet and substrate (photo: Donna Coveney).

Material scientists aim to improve control over the adhesion or de-adhesion of a system by manipulating the physical properties of cohesive bonds between materials. In this thesis, on the other hand, we investigate how the adhesion of thin sheets is affected by the geometric conditions of the system, for given material properties. For example, at what point will a sheet delaminate from a sticky substrate if the ensemble is compressed? What can we learn about the material properties and/or the strength of adhesion of a sheet by looking at its equilibrium shape? What geometric constraints are required to prevent irreversible stiction in a system? How can we alter such constraints to transition between adhered and de-adhered states? These are all questions that are closely linked to

applications such as the ones discussed above, be it flexible electronics, graphene coatings, or electromechanical switch design. By answering these questions we hope to improve our understanding of the physics that governs the behaviour of the systems at hand, as well as gain insight into the adhesion driven deformation of thin elastic sheets in general.

In this thesis we study how the deformation and adhesion of thin elastic sheets is determined by the balance of the restorative bending forces in the sheet and the adhesive strength between sheet and substrate. This balance is governed by the interplay between material properties and geometric conditions of a system, together with any externally applied forces. A better understanding of this interplay is the central aim of this work. As becomes clear from figure 1.2, the problems we consider commonly feature deformations that are *geometrically non-linear* – where slopes cannot be assumed small – an area of great scientific interest that still poses many open questions.

1.2. Structure of the thesis

In the last part of this chapter we provide some theoretical background that forms the basis of much of the research presented later on. The concept of a uniform elastic sheet that undergoes large bending deformations is intimately linked to that of the *elastica* - the family of curves describing the one-dimensional shape of an elastic lamina (Levien, 2008). We give a brief introduction to the elastica problem and discuss its link to the Calculus of Variations. As an application of the Calculus of Variations, we derive a *delamination condition* which gives a condition on the discontinuity of curvature required at a point of adhesive contact between an elastic sheet and a rigid substrate. We further discuss the concepts of molecular and macroscopic surface energies and how they give rise to adhesion phenomena.

In Chapter 2 we present one of the simplest possible systems: an elastic loop adhered to a rigid substrate – the 'Sticky Elastica'. In contrast to previous studies of the shape of delamination 'blisters' (Vella *et al.*, 2009*a*; Aoyanagi *et al.*, 2010), we develop a theory that accounts for geometrically nonlinear deflections. Starting from the classical Euler Elastica we provide numerical results for the dimensions of such blisters for a variety of geometric confinements and develop corresponding asymptotic expressions. Interestingly, we find that the width of such blisters does not grow monotonically with increased confinement. Our theoretical predictions are confirmed by simple desktop experiments and suggest a new method for the measurement of the *elastocapillary length* (Bico *et al.*, 2004) for deformations that cannot be considered small. This work has important implications for applications such as flexible electronics (Sun *et al.*, 2006; Rogers *et al.*, 2010), where delamination and buckling are intentionally integrated into circuit design.

Sheets that are fully adhered to an elastic substrate tend to first wrinkle and then blister as the substrate is compressed (Pocivavsek *et al.*, 2008; Diamant & Witten, 2010). Understanding the transition between the two states is made difficult by the non-trivial elastic interaction between sheet and substrate (Vella *et al.*, 2009*a*). A way around this difficulty is to consider a thin elastic sheet floating on a liquid surface. This is the subject of Chapter 3. We show that the sheet delaminates from the liquid over a finite region at a critical compression: it forms a delamination blister. The transition from wrinkled to blistered states occurs when delamination becomes energetically favourable compared to wrinkling. We determine the initial blister size and the evolution of blisters with continuing compression before verifying our theoretical results with experiments at a macroscopic scale.

Moving from flat to patterned substrates, we consider the problem of the deposition of planar sheets onto adhesive, but non-planar, substrates in Chapter 4. Recent experiments on graphene adhesion have shown a discontinuous 'snap-through' transition between adhered and de-adhered states for certain substrate geometries (Scharfenberg *et al.*, 2012). We develop a model to understand the equilibrium of the sheet allowing for partial conformation of sheet to substrate. This model gives physical insight into the observations of a 'snap-through' from flat to conforming states (Scharfenberg *et al.*, 2012) and emphasises the crucial role of substrate shape in determining the nature of this transition. Finally we propose a substrate shape that should exhibit a continuous, rather than 'snap-through', transition.

In Chapter 5 we consider the phenomenon of stiction failure in nanoelectromechanical (NEM) switches. An undesirable side-effect of smaller and smaller electronic systems is the increasing importance of adhesive van der Waals forces: in NEM switches, stiction failure (where the switch gets stuck in its ON state) is thus a major design problem (Jensen *et al.*, 2005; Loh *et al.*, 2011; Loh & Espinosa, 2012). We develop a mathematical model that captures the elastic bending of a contact switch in response to both electrostatic and van der Waals forces. In contrast to previous studies (Mastrangelo & Hsu, 1993; Dequesnes *et al.*, 2002), the theory developed accounts for deflections with large slope. We solve the resulting equations numerically to study how a cantilever beam adheres to a fixed bottom electrode: transitions between free, 'pinned' and 'clamped' states are shown to be discontinuous and to exhibit significant hysteresis. These results have interesting implications for NEM switch design and will hopefully help engineers to avoid irreversible stiction.

Chapter 6, finally, presents a summary of our findings and a discussion of some possibilities for future research that could follow on from the work presented here.

Each of the chapters above is essentially self-contained (with some of the theoretical considerations being based on the concepts discussed in the following section). Each problem is introduced with a specific motivation and an overview of the relevant scientific literature. At the end of each chapter, we further aim to place the problem into a wider context and highlight its relevance to modern applications.

1.3. Theoretical background

1.3.1. The Elastica

The general definition of the elastica is '...the family of curves arising from an elastic band of arbitrary given length, and arbitrary given tangent constraints at the endpoints' (Levien, 2008). The first attempt at mathematically describing the *lamina elastica* was published more than 300 years ago by James Bernoulli (1692) who was trying to find

> ...the bendings or curvatures of beams, drawn bows, or of springs of any kind, caused by their own weight or by an attached weight or by any other compressing forces... .

However, he only succeeded in solving the specific case of an elastica whose ends are perpendicular to one another – the rectangular elastica. It was another 50 years before Leonhard Euler found a way to solve the problem in its general form. His solution was prompted by a letter from Daniel Bernoulli in 1742, who wrote the energy of a bent curve in the form $\int \frac{\mathrm{d}s}{RR}$, where s is the arc-length of the curve and R the local radius of curvature. Today, this would more commonly be written as $\int {\theta_s}^2 \, \mathrm{d}s$, where $\theta(s)$ is the angle (measured to the horizontal) of the tangent to the curve and $()_s = \mathrm{d}/\mathrm{d}s$. In 1744, Euler solved for the state of the elastica by minimizing the corresponding energy functional in his *Methodus Inveniendi Lineas Curvas* (Euler, 1744). Even though the formulation of the Variational Principle has been attributed to Maupertuis (1744), Euler's *Methodus* is commonly hailed as the advent of the Calculus of Variations.

Today, the equation of equilibrium for the elastica is often derived using the balancing of moments, as in Love (1944), for example. However, here it will be convenient to make use of the variational methods, since this lends itself to straight-forward formulations of problems involving adhesion.

The elastica equation is found as follows. Consider a thin rod or sheet of length l and uniform cross-section, which is straight in its unstressed state. The sheet is bent by displacing one end by a horizontal distance Δl and a vertical distance Δd. In the case of the elastica, as with the problems studied in the following chapters, the sheet is assumed

to deform much more easily by bending *out-of-plane*, rather than compressing *in-plane*. Integrating over the length of the sheet we write $\int \mathrm{d}s = l$, i.e. the contour length of the deformed sheet is the same as its natural length; the sheet is said to be *inextensible*. The bending is restricted to a principal plane, so that no twisting occurs. Denoting the bending stiffness in this plane by $\mathcal{B}$, the Lagrangian of the sheet can be written as

$$U = \int_0^l \tfrac{1}{2}\mathcal{B}\theta_s^2 \,\mathrm{d}s + \alpha\big[\Delta l - \int_0^l (1-\cos\theta)\,\mathrm{d}s\big] + \beta\big[\Delta d - \int_0^l (1-\sin\theta)\,\mathrm{d}s\big], \tag{1.1}$$

where $[x(s), w(s)]$ are the coordinates of the sheet, with $\mathrm{d}x = \cos\theta \mathrm{d}s$ and $\mathrm{d}w = \sin\theta \mathrm{d}s$. α and β are Lagrange multipliers (Gelfand & Fomin, 2000) which enforce the geometric constraints

$$\Delta l = \int_0^l (1-\cos\theta)\ \mathrm{d}s, \quad \Delta d = \int_0^l (1-\sin\theta)\ \mathrm{d}s. \tag{1.2}$$

The equation of equilibrium is obtained by setting the variation in the energy, δU, to be zero – this corresponds to an extremum of the functional. To compute δU we take $\theta \to \theta + \delta\theta$, $\alpha \to \alpha + \delta\alpha$ and $\beta \to \beta + \delta\beta$. The latter two variations yield the constraints (1.2). The variation in θ, on the other hand, results in the elastica equation

$$\mathcal{B}\theta_{ss} = \alpha\sin\theta + \beta\cos\theta, \tag{1.3}$$

Strictly speaking, the family of elastica shapes is usually restricted to those undergoing compression along the x-axis only. In this case the last term of (1.3) disappears and α is defined as $\alpha = -T$, the in-plane stress in the sheet that results from the initial displacement (Love, 1944). Solutions to these equations can be found by making use of elliptical integrals. This will be discussed in some detail in Chapter 2.

It is instructive to further consider the case of highly deformed sheets subjected to a general external force, rather than simply an imposed end displacement. A familiar example of such a system is the cantilever beam. We assume that the applied force is a function of the vertical deflection of the beam, writing the corresponding energy density as $G = G(w)$. The Lagrangian functional in this case is given by

$$U = \int_0^l \big\{\tfrac{1}{2}\mathcal{B}\theta_s^2 + G(w) + \beta(s)[w_s - \sin\theta]\big\}\,\mathrm{d}s, \tag{1.4}$$

where the Lagrange multiplier $\beta(s)$ is now dependent on s (rather than a constant as above). It enforces the geometric relation $w_s = \sin\theta$ and corresponds to the vertical component of the stress in the sheet. Additionally to the variations in θ and β, we now also take $w \to w + \delta w$ and write $G(w) \to G(w+\delta w) \simeq G(w) + \delta w\, G_w$. This results in the

following equation of equilibrium

$$\mathcal{B}\theta_{ss} = -\beta(s)\cos\theta, \tag{1.5}$$

subject to the constraints $\beta_s = G_w$ (and $w_s = \sin\theta$).

Example: cantilever deflected under its own weight. The beam is presumed clamped at its origin, with $\theta(0) = 0$, and free at the other end, with $\theta_s(l) = 0$ and $\beta(l) = 0$. The gravitational energy is then written as $G(w) = \rho g h w$, with ρ being the density of the beam, h its thickness and g the acceleration due to gravity. In this case $\beta_s = \rho g h$ and $\beta = \rho g h(s - l)$. Equation (1.5) then reduces to the heavy elastica equation (Wang, 1986)

$$\mathcal{B}\theta_{ss} = \rho g h(l - s)\cos\theta. \tag{1.6}$$

This simplification, made possible due to the integrability of β_s, is somewhat fortuitous. Instead of using the method of Lagrange multipliers it is in fact also possible to obtain (1.6) using integration by parts (Vella *et al.*, 2009*b*). We note that in the small deformation limit (where $\mathrm{d}w/\mathrm{d}x \ll 1$), equation (1.6) reduces to the familiar cantilever beam equation $\mathcal{B}\frac{\mathrm{d}^4 w}{\mathrm{d}x^4} = \rho g h$.

In Chapter 5, the case of a cantilever subjected to a combination of van der Waals and electrostatic forces is studied. We shall see that this results in an energy $G(w, \theta)$, explicitly dependent on w and θ, adding a term $-G_\theta$ to the right hand side of (1.5).

More than 250 years after the publication of his *Methodus*, Euler's Calculus of Variations is still called upon to investigate (amongst numerous other things) the physics of deformed sheets and, in particular, the problem most relevant to this thesis: an elastic sheet that is partially adhered to a substrate. Before proceeding to discuss the interplay between elastic bending and adhesion (in section 1.3.3.), it will be instructive to consider the concept of adhesion in itself, and the related concept of surface energies.

1.3.2. Surface energies and adhesion

The surface tension of a liquid has the most striking effects. It causes liquids to form drops and allows water striders to walk on water. Surface tension arises because a liquid molecule at the surface is in an energetically unfavourable state, compared to a molecule in the bulk liquid. This is due to the bulk molecule being completely surrounded by attractive neighbours, whereas the surface molecule experiences only half of that attraction (De Gennes *et al.*, 2003). Creating a surface is thus energetically costly for a liquid and

the ensuing minimization of surface area manifests itself in many different phenomena – such as the spherical nature of drops, capillary effects and the floating of dense objects (Vella, 2007).

Much the same physical considerations apply to surfaces of solids – but what is known as surface tension for liquids is commonly referred to as *surface energy* in the case of solids. Understanding the concept of surface energies is helped by 'zooming in' to the molecular level: on this level the adhesion between two surfaces is due to short-range forces, predominantly van der Waals forces, acting between molecules. In this thesis, we are mainly concerned with the adhesion of thin sheets to non-polar substrates. The interaction energy between a sheet molecule and a substrate molecule may then be written (Israelachvili, 1992)

$$U_{m-m} = -C\left(\frac{1}{r^6} - \frac{D}{r^{12}}\right), \tag{1.7}$$

with r the distance between the two molecules and C and D material dependent parameters. C is referred to as the 'Interaction Constant' or 'London Constant' and has units Jm^6, whereas D can be related to the van der Waals radius, which decribes the equilibrium contact distance between two objects (see below).

For the case of small angles, $\theta(s) \ll 1$, (1.7) yields the following van der Waals energy (per unit area) for a sheet of thickness h, whose mid-plane is at a height $w(s)$ above a flat substrate (a derivation of this result is given in section 4.A):

$$U_{vdW}(s) = -\frac{A_{\mathrm{H}}}{12\pi}\left[\left(\frac{1}{(w(s)-h/2)^2} - \frac{1}{(w(s)+h/2)^2}\right) - \frac{D}{30}\left(\frac{1}{(w(s)-h/2)^8} - \frac{1}{(w(s)+h/2)^8}\right)\right]. \tag{1.8}$$

Where $A_{\mathrm{H}} \equiv \pi^2 C\rho\rho_s$ is known as the Hamaker constant, and ρ and ρ_s are the densities of sheet and substrate, respectively. Many standard treatments of thin sheets interacting with a semi-infinite substrate assume that $w(s) \gg h$, for all values of s (see for example Oyharcabal & Frisch (2005)). In that case, the van der Waals interaction reduces to the familiar form $U_{vdW}(s) = -a\left[w(s)^{-3} - bw(s)^{-9}\right]$, where $a = A_{\mathrm{H}}h/6\pi$ and $b = 2D/15$.

However, in the cases studied in this thesis, the approximation $w(s) \gg h$ breaks down when the sheet is 'in contact' with the substrate and the full expression (1.8) is required. Here, a given part of the sheet is 'in contact' if it is in energetic equilibrium close to the substrate, where the equilibrium distance is determined by minimizing the van der Waals energy (1.8). We define the van der Waals radius as

$$w^* = w_0 - h/2, \tag{1.9}$$

where w_0 is the equilibrium contact distance between the mid-plane of the sheet and the substrate surface. w^* is thus the distance between the bottom of the sheet and the top of the substrate, when in contact. Typical values for w^* are $\sim 2-3$ Å (see Chapter 4), which is much smaller than any of the sheet thicknesses considered. We can therefore assume that $w^* \ll h$, in what follows. Minimizing the energy in (1.8), we find that $D \simeq (15/2){w^*}^6$.

In the following paragraphs, we discuss how the macroscopic concept of adhesion can be related to the molecular van der Waals forces. The *adhesion energy*, $\mathcal{E}_{adh}$ is commonly defined as the energy required to bring surfaces together from infinity to the contact distance w_0 (Israelachvili, 1992). It is negative by convention. In the limit $w^* \ll h$, we obtain for the adhesion energy per unit area

$$\mathcal{E}_{adh} = -\int_{\infty}^{w_0} f_{vdW}\ \mathrm{d}w \simeq -\frac{A_{\mathrm{H}}}{16\pi}\frac{1}{{w^*}^2}, \tag{1.10}$$

where $f_{vdW} = -\mathrm{d}U_{vdW}/\mathrm{d}w$, is the van der Waals force acting between the two surfaces.

Surface energy on the other hand is defined as a positive quantity. We consider the solid–vapour and solid–solid surface energies per unit area, γ_{sv} and γ_{ss}. For the bottom surface of a sheet and the top surface of a substrate, an infinite distance apart, the combined surface energy per unit area is given by

$$\gamma_\infty = \gamma_{sv}^{(\mathrm{sub})} + \gamma_{sv}^{(\mathrm{sheet})} \tag{1.11}$$

For a sheet and a substrate of unit area in contact, on the other hand, only one surface needs to be considered, namely the sheet–substrate interface, carrying energy γ_{ss}. In removing the sheet from contact to infinity this energy is lost and γ_∞ is gained. We define the *strength of adhesion* as

$$\Delta\gamma \equiv \gamma_\infty - \gamma_{ss} = \gamma_{sv}^{(\mathrm{sub})} + \gamma_{sv}^{(\mathrm{sheet})} - \gamma_{ss}, \tag{1.12}$$

and note that, from the definition of the adhesion energy, we have $\Delta\gamma = -\mathcal{E}_{adh} = A_{\mathrm{H}}/16\pi{w^*}^2$. This establishes a relation between the macroscopic concept of adhesion and the molecular van der Waals forces, parametrized by A_{H} and w^*.

For adhesive materials, $\Delta\gamma$ is always positive, and from (1.12) it is clear that for strong adhesion we require $\gamma_{sv}^{(\mathrm{sub})} + \gamma_{sv}^{(\mathrm{sheet})} \gg \gamma_{ss}$. It is also instructive to consider the special case of two identical surfaces, where $\gamma_{sv}^{(\mathrm{sub})} = \gamma_{sv}^{(\mathrm{sheet})} \equiv \gamma$. Upon contact, both solid–vapour surfaces are lost and $\gamma_{ss} = 0$, since all molecules are now entirely surrounded by attractive neighbours. It follows that $\Delta\gamma = 2\gamma$, i.e. the surface energy is exactly half the strength of adhesion.

Typical values for the Hamaker constant are $A_{\mathrm{H}} \approx 10^{-19}$ J and for the van der Waals radius $w^* \approx 0.2$ nm (Israelachvili, 1992). For a sheet resting on a substrate, this gives $\Delta\gamma \approx 0.049$ J/m^2, which is comparable to the surface tension of water ≈ 0.072 J/m^2. However, the effects of solid surface energies are less commonly observed in everyday life, due to the macroscopic surface roughness of most solid objects. Since solid objects are usually much less conforming than liquids, the energetic gain is smaller when two rough solid surfaces are brought into contact (since their roughness prevents true interfacial contact for most of the surface area). However, for very smooth or conforming surfaces, or on small enough scales, the energy gain can be large – resulting in strong adhesion.

1.3.3. The delamination boundary condition

Following recent work by Majidi (2007), we present in this section a derivation of the natural boundary condition at the adhesive boundary using the variational principle above. This calculation leads to a result previously derived by Obreimoff (1930) on physical grounds. However, the variational formulation will be of use more generally.

Take a one-dimensional curve, parametrised by the arc-length $s \in [0, l]$ and intrinsic angle $\theta(s)$. $\theta(s)$ conforms to a known function $\theta^{(0)}(s)$ (the substrate in our case) such that $\theta(s) \equiv \theta^{(0)}(s)$ in a given region $\mathbf{a} = \{s | s \in [0, \lambda]\}$ and is free in region $\mathbf{b} = \{s | s \in [\lambda, l]\}$. We wish to find the function $\theta(s)$ that minimizes the energy functional

$$U = \int_0^\lambda f_{\mathbf{a}}(\theta, \theta_s)\, \mathrm{d}s + \int_\lambda^l f_{\mathbf{b}}(\theta, \theta_s)\, \mathrm{d}s, \tag{1.13}$$

with $f_{\mathbf{a}}, f_{\mathbf{b}}$ being the Lagrangian densities in the regions $\mathbf{a}$ and $\mathbf{b}$, respectively. Note that in general the point of delamination, λ, is not known a priori.

We are therefore dealing with the classical elastica problem, subject to the additional constraint that the elastica conforms to the substrate up to the point λ at which contact is lost. Calling again on the Calculus of Variations we minimize the energy of the system by considering the variation $\theta \to \theta + \delta\theta$ and setting $\delta U / \delta\theta = 0$ (since $\theta^{(0)}(s)$ is given). The shape of the elastica in the free region, $\theta(s)$, is then determined simply by the solution of the usual Euler–Lagrange equation

$$\frac{\partial f_{\mathbf{b}}}{\partial \theta} - \frac{\mathrm{d}}{\mathrm{d}s}\left(\frac{\partial f_{\mathbf{b}}}{\partial \theta_s}\right) = 0. \tag{1.14}$$

However, this differential equation is supplemented by an adhesion boundary condition, which determines the point of contact/loss of contact, λ. This boundary condition arises

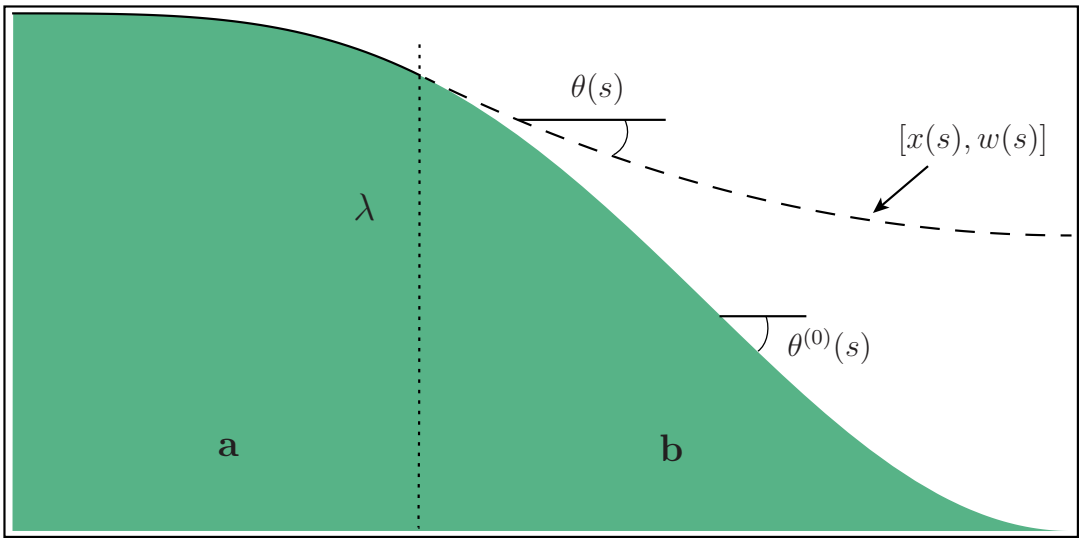

Figure 1.3.: Schematic representation of a curve, with intrinsic equation $\theta(s)$, partially conforming to a substrate, given by $\theta^{(0)}(s)$. The curve is conformal to the substrate in region **a** (solid line), for $s < \lambda$ and free in region **b**, for $\lambda < s < l$ (dashed).

from considering the variation in the position of the contact line, i.e. $\delta U/\delta\lambda = 0$, and is found to be (Landau & Lifschitz, 1970; Majidi, 2007):

$$0 = \left[\theta_s^{(0)}(\lambda) - \theta_s(\lambda)\right] \left.\frac{\partial f_{\mathbf{b}}}{\partial \theta_s}\right|_{\lambda} + [[f]]_{\mathbf{a}}^{\mathbf{b}}, \tag{1.15}$$

with $[[f]]_{\mathbf{a}}^{\mathbf{b}} \equiv f_{\mathbf{b}}(\lambda^+) - f_{\mathbf{a}}(\lambda^-)$.

Consider an elastic beam of stiffness $\mathcal{B}$ which is free for $\lambda < s < l$ but conforms to a substrate for $0 < s < \lambda$ due to the presence of a constant adhesion $\Delta\gamma$. We make use of (1.15) to determine the point of contact, λ. The energetic penalty due to bending is $(\mathcal{B}/2)\theta_s^{(0)}(s)^2$ in region **a** and $(\mathcal{B}/2)\theta_s(s)^2$ in **b**. In region **b** a surface energy penalty $\Delta\gamma$ per unit length must be paid since in this region the two materials have been separated and surface created. We thus have

$$f_{\mathbf{a}} = \frac{\mathcal{B}}{2}\theta_s^{(0)}(s)^2, \qquad f_{\mathbf{b}} = \frac{\mathcal{B}}{2}\theta_s(s)^2 + \Delta\gamma. \tag{1.16}$$

Using (1.14), the equilibrium state of the free part of the sheet is given by $\mathcal{B}\theta_{ss} = 0$. Substituting the energy densities from (1.16) into (1.15) gives

$$\left[\theta_s^{(0)}(\lambda) - \theta_s(\lambda)\right]^2 = 2\Delta\gamma/\mathcal{B}. \tag{1.17}$$

The quantity on the right hand side may be expressed in terms of an important characteristic length of the system, the *elastocapillary* length (Bico *et al.*, 2004), which is defined

as

$$\ell_{ec} = \sqrt{\mathcal{B}/\Delta\gamma} \tag{1.18}$$

and is a measure of the relative strengths of the bending stiffness of the sheet and the sheet-substrate adhesion. We therefore write (1.17) as $|\theta_s^{(0)}(\lambda) - \theta_s(\lambda)| = \sqrt{2}/\ell_{ec}$.

In Chapters 2 and 5 we will consider the specific case of a flat substrate, where $f_{\mathbf{a}} = 0$. In this case (1.17) reduces to (Obreimoff, 1930; Landau & Lifschitz, 1970; Glassmaker & Hui, 2004; Majidi, 2007)

$$|\theta_s(\lambda)| = \sqrt{2}/\ell_{ec}.$$

In Chapter 4 we will consider the case of non-flat substrates in the limit of small deformations $\theta \ll 1$ for which $\theta_s(s) \simeq w_{xx}(x)$, with $w(x)$ being the vertical displacement of the sheet from its flat reference state. Condition (1.17) then reduces to

$$|w_{xx}^{(0)}(\lambda) - w_{xx}(\lambda)| = \sqrt{2}/\ell_{ec}. \tag{1.19}$$

Chapter 2

Delamination Blisters: from Small to Large Deformations

Synopsis

We consider the form of an elastic loop adhered to a rigid substrate: the 'Sticky Elastica'. In contrast to previous studies of the shape of delamination 'blisters', the theory we develop accounts for deflections with large slope (i.e. geometrically nonlinear). Starting from the classical Euler Elastica we provide numerical results for the dimensions of such blisters for a variety of end-to-end confinements and develop asymptotic expressions that reproduce these results well, even up to the point of self-contact. Interestingly, we find that the width of such blisters does not grow monotonically with increasing confinement. Our theoretical predictions are confirmed by simple desktop experiments and suggest a new method for the measurement of the *elastocapillary length* for deformations that cannot be considered small and has implications for applications such as flexible electronics, which we discuss.

2.1. Introduction

Delamination blisters are often the undesired consequence of an adhesive film placed imperfectly on a substrate. They are the nemesis of anyone trying to wrap Christmas presents using sticky tape and regularly frustrate smartphone users who want to put a protective film on their phone screen. Blisters appear when an adhered film is subject to an in-plane compressive strain relative to the substrate. Such a strain can result from a differential compression (for example due to heating) or because of a mismatch between substrate and film geometries (Gioia & Ortiz, 1997; Faulhaber *et al.*, 2006; Vella *et al.*, 2009*a*; Aoyanagi *et al.*, 2010). Even small mismatches can give rise to significant blisters, which can, in turn, greatly affect the functionality of the adhering film in applications from protective coatings to the conduction characteristics of Few Layer Graphene sheets (Kim & Castro Neto, 2008; Schniepp *et al.*, 2008; Li *et al.*, 2009).

In spite of some of the negative connotations of delamination, historically, delamination blisters have found application as a simple means of measuring the strength of adhesion between two materials, namely in a series of techniques known as *blister tests* (Obreimoff, 1930; Jensen, 1991; Wan, 1999; Chopin *et al.*, 2008; Koenig *et al.*, 2011). However, more recently, it has been proposed that partial delamination and buckling of thin adhesive sheets can be intentionally integrated into the design of flexible electronic devices (Sun *et al.*, 2006; Khang *et al.*, 2009; Rogers *et al.*, 2010; Cheng *et al.*, 2011).

In flexible electronics, thin electronic circuits are imprinted on a flexible substrate, usually made from elastic materials such as polyethylene or polyimide (Wong & Salleo, 2009). These composite systems are designed to elastically accommodate high degrees of bending without failure. This has many obvious technological applications such as bendable screens (Schwesig *et al.*, 2004), or on-skin medical labs, measuring a person's vital signs (Ma, 2011). One of the main design difficulties in contemporary flexible electronics arises from the mismatch in elastic response between the soft substrate and the stiffer electronic circuits. The large strains of the substrate can often not be supported by the circuit, causing the system to fail. The studies mentioned above attempt to avoid such failure by allowing the circuits to accommodate strains by buckling, rather than compressing in-plane.

In these devices, the conducting components are only adhered to the substrate in some regions and not others; this 'blistered' shape allows them to accommodate the flexure of the substrate without deforming plastically – see figure 2.1b. In current flexible electronic applications the form of these blisters is controlled by patterning the substrate with a periodic variation in adhesive strength – see figure 2.1a. However, such techniques may suffer from the spontaneous formation of delamination blisters with a well-defined size

(Sun *et al.*, 2006; Ebata *et al.*, 2012; Vella *et al.*, 2009*a*); understanding the size and form of such blisters is important since the conducting components can be damaged if curvatures become too large, as illustrated in figure 2.1c (Chen *et al.*, 2002; Sun *et al.*, 2006).

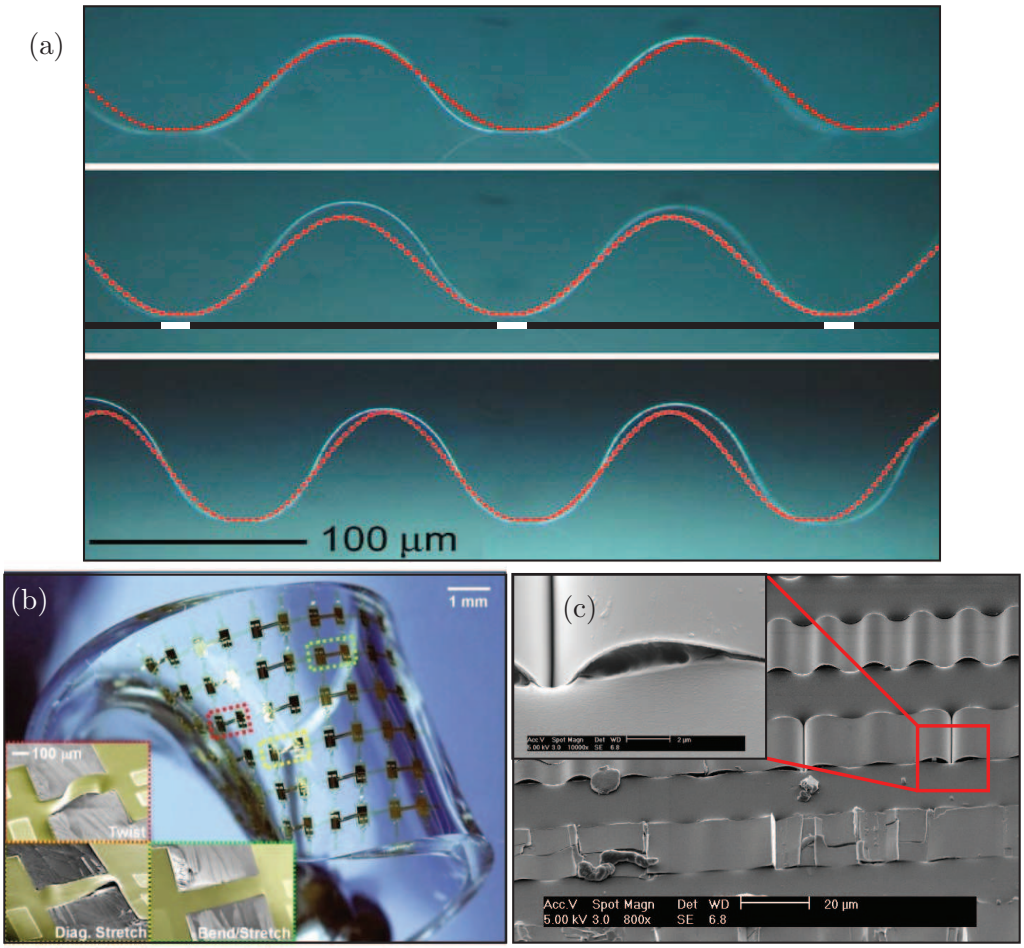

Figure 2.1.: Delamination blisters as observed in flexible electronic applications. (a) Image of experiments with GaAs thin films deposited on a patterned PDMS substrate (reproduced from Jiang *et al.* (2007*b*)). The substrate is composed of alternating segments of high and low adhesion (with widths 10 μm and 90 μm, respectively). The segments are highlighted by white and black bars in the central panel (added by author). The delamination blisters are obtained by pre-straining the substrate, then depositing the film in its flat state and subsequently relaxing the pre-strain in the substrate. The red curves show the cosine profile, provided by small deformation theory. (b) Application of buckled sheets in flexible electronics (reproduced from Rogers *et al.* (2010)). (c) Image showing Si films on a patterned PDMS substrate, illustrating various modes of failure due to extreme strains (reproduced from Jiang *et al.* (2007*a*)). The inset highlights cohesive failure where the film has partially delaminated from the high adhesion segments of the substrate, leading to a crease in the sheet.

While the formation of delamination blisters is a classical problem, previous analyses have focussed on the limit of blisters with a small slope (small deformations). However,

in many new applications and particularly for flexible electronics, this restriction is inappropriate. This can be clearly seen in the examples shown in figure 2.1. While the highly deformed shape of an elastic strip is well-known, namely the elastica, there is a need to extend the classical theory of delamination blisters to large deformations. In particular, the combination of adhesion and large deflection elasticity seems only to have been considered for the case of self-contacting 'rackets' (Glassmaker & Hui, 2004; Cohen & Mahadevan, 2003).

In this chapter, therefore, we consider the form of a blister without the restriction of small slopes — the 'Sticky Elastica'. Using a combination of numerical, asymptotic and experimental techniques we show how the results of previous small deformation analyses may be modified to take into account these large deformations and suggest how experimental data might best be analysed in the light of our results.

An article based on the work described in this chapter has been published in *Soft Matter*, (Wagner & Vella, 2013). The research was performed under the supervision of Dominic Vella.

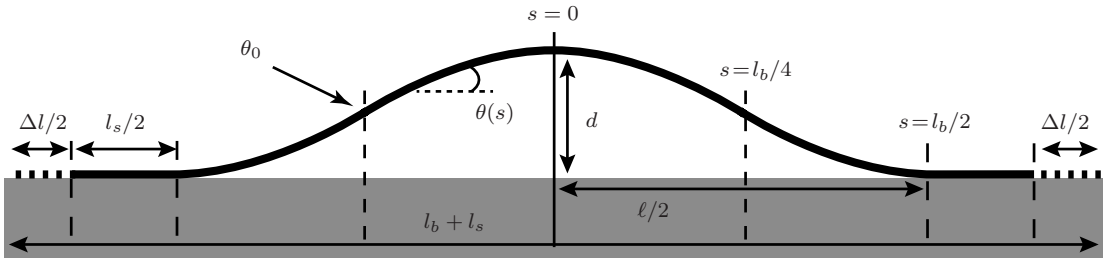

Figure 2.2.: Schematic of a thin sheet resting on an adhesive substrate and subject to an end-to-end compression Δl. The result is a blister with arc-length l_b and dimensions d and ℓ, symmetric around $s = 0$.

2.2. The 'Sticky Elastica' equation

We consider an inextensible elastic sheet, resting on a semi-infinite, rigid substrate. The sheet is subjected to an in-plane compression Δl which results in a delamination blister of height d and width ℓ (figure 2.2). We assume that this compression is applied quasi-statically so that we may neglect dynamic effects. The shape of the blister is defined by the intrinsic angle $\theta(s)$, (s being the arc-length). A point on the blister has coordinates $[x(s), w(s)]$ with x and w given by the geometric relationships $\mathrm{d}x = \cos\theta\,\mathrm{d}s$ and $\mathrm{d}w = \sin\theta\,\mathrm{d}s$. The delaminated portion has arc-length l_b, which is initially unknown. The end-points of the delaminated regions are then given by $s = \pm l_b/2$; we assume that the

system is symmetric about $s = 0$. Since the sheet remains smooth, we must have that $\theta(\pm l_b/2) = \theta(0) = 0$.

We use a variational approach to derive a governing equation for the shape of the blister and corresponding boundary conditions. In this formulation of the problem, we consider the energy of the system to be composed of a contribution from the bending energy of the sheet and another term from the sheet-substrate adhesion energy, $\Delta\gamma$, as discussed in section 1.3.3. (We neglect the effect of the weight of the delaminated portion of the sheet for simplicity. This assumption is valid provided that $l_b\rho gh/\Delta\gamma \ll 1$, in which ρ is the sheet density, h its thickness and g the acceleration due to gravity – see Appendix 2.A.) We must minimize this combined energy subject to the constraint of an imposed end-to-end displacement Δl. Supplementing the energy (measured relative to the flat, fully adhered, state) with a Lagrange multiplier to enforce this constraint, the problem reduces to the minimization of

$$U = \int_{-l_b/2}^{l_b/2} \left(\tfrac{1}{2}\mathcal{B}\theta_s^2 + \Delta\gamma\right) \mathrm{d}s - \alpha\Big[l_b - \Delta l - \int_{-l_b/2}^{l_b/2} \cos\theta \; \mathrm{d}s\Big]. \tag{2.1}$$

This is essentially the expression given in equation (1.1) with an additional adhesive term and no vertical displacement of the sheet ends. The sheet has Young's modulus E and Poisson ratio ν so that the bending stiffness is (Landau & Lifschitz, 1970)

$$\mathcal{B} = \frac{Eh^3}{12(1-\nu^2)}. \tag{2.2}$$

The second term in the first integral represents the surface energy due to delamination (see following section). The third term corresponds to the geometric constraint due to compression, (1.2), which is enforced by the Lagrange multiplier α.

2.2.1. Surface energy

The surface energies per unit area associated with the different surfaces are γ_{ss} (substrate–sheet), $\gamma_{sv}^{(\mathrm{sub})}$ (substrate–vapour) and $\gamma_{sv}^{(\mathrm{sheet})}$ (sheet–vapour). We consider first the reference state of a planar sheet (see figure 2.3) for which the total surface energy is

$$E^{(0)} = \gamma_{ss} l + \gamma_{sv}^{(\mathrm{sub})}(l_{\mathrm{sub}} - l) + \gamma_{sv}^{(\mathrm{sheet})} l, \tag{2.3}$$

where l and l_{sub} are the lengths of the sheet and substrate, respectively.

We compare this energy with that of a sheet whose ends are first confined by bringing them a distance Δl together. In this case both l and l_{sub} remain constant but sheet–vapour and substrate–vapour surfaces of length l_b are created, and a substrate–sheet surface over

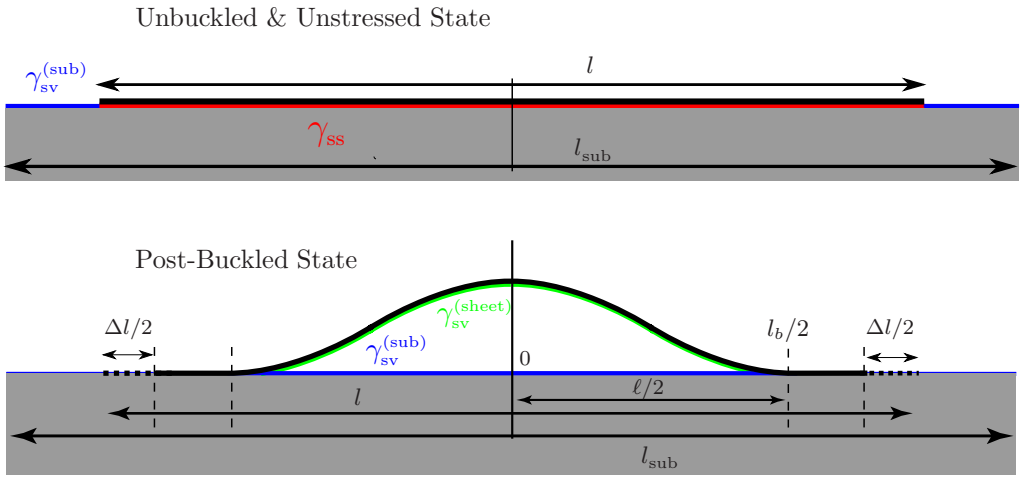

Figure 2.3.: Diagram of unbuckled and buckled states, illustrating the change in surface energies due to delamination (see text).

the same distance is lost. The total surface energy of the post-buckled state is therefore written as

$$E^{(1)} = \gamma_{ss}(l - l_b) + \gamma_{sv}^{(\text{sheet})} l_b + \gamma_{sv}^{(\text{sub})} \left[l_{\text{sub}} - (l - l_b) \right] + \gamma_{sv}^{(\text{sheet})} l. \tag{2.4}$$

The change in surface energy from the planar to the buckled configuration is

$$\Delta E = E^{(1)} - E^{(0)} = -l_b(\gamma_{ss} - \gamma_{sv}^{(\text{sheet})} - \gamma_{sv}^{(\text{sub})}) \equiv l_b \Delta\gamma, \tag{2.5}$$

where $\Delta\gamma = \gamma_{sv}^{(\text{sheet})} + \gamma_{sv}^{(\text{sub})} - \gamma_{ss}$. We anticipate that $\Delta\gamma > 0$ since de-adhering is energetically unfavourable.

The above calculation assumes that the substrate is incompressible, i.e. l_{sub} is constant. For the case of a *compressible* substrate, in which the ends of the sheet remain fixed with respect to the substrate, it is important to note that an amount of substrate–vapour surface of length Δl is lost in compression. In this case, the energy change from flat to buckled states is given by

$$\Delta E = l_b \Delta\gamma - \Delta l \gamma_{sv}^{(\text{sub})}. \tag{2.6}$$

However, we will see in the next section that the change in surface energy ΔE only affects the shape of the blister via the variation in the blister length δl_b. The last term in (2.6) can be treated as a constant which does not enter the variational minimization of (2.1) and can subsequently be ignored. Our account is therefore valid for both incompressible and compressible substrates.

The simple energetic picture presented here should really take account of the fact that delamination is generally composed of fracture in a combination of modes I and II. The interfacial energy $\Delta\gamma$ is therefore a function of the relative amounts of each mode present

in a given scenario. However, for blisters much larger than the thickness of the sheet, this fraction is independent of shape and so $\Delta\gamma$ may be assumed constant (Hutchinson & Suo, 1992).

2.2.2. Governing equation and delamination condition

The Calculus of Variations allows us to determine equations for the shape of the delaminated blister, $\theta(s)$, and the length of the delaminated portion, l_b, that extremize the functional U given in (2.1), as discussed in section 1.3.3. The requirement that $\delta U/\delta\theta = 0$ yields the classical elastica equation for a sheet subject to a compressive stress T (Love, 1944; Audoly & Pomeau, 2010):

$$\mathcal{B}\theta_{ss} = -T\sin\theta, \tag{2.7}$$

where the Lagrange multiplier $\alpha \to -T$. The requirement that $\delta U/\delta l_b = 0$ yields the delamination condition on the curvature at contact,

$$|\theta_s(\pm l_b/2)| = \sqrt{2}/\ell_{ec}, \tag{2.8}$$

where ℓ_{ec} is the *elastocapillary* length of the system, as defined in (1.18). We note that (2.7) is the classic elastica equation and hence that the shape of the delamination blister is precisely that of an elastica with the same arc-length l_b and compression Δl. The crucial difference between the classic elastica and the 'Sticky Elastica' is that the former has a fixed arc-length while the arc-length of the latter changes in response to compression to ensure that the curvature at the end point satisfies (2.8).

2.2.3. Linear Considerations

It is well known that it is possible to make analytical progress for the nonlinear equation (2.7), which also describes the motion of a constant length pendulum (with arc-length replaced by time). We shall see that this approach is useful here, too. However, it is instructive to consider first the linearized problem, i.e. the small deformation limit. In this limit, $\theta(s) \ll 1$ and geometrical considerations give us that $\theta \sim d/\ell$ where d is the blister height and ℓ its width. Since (2.8) gives us that $\theta_s \sim 1/\ell_{ec}$ and $\ell \approx l_b$ (for small deformations) we then have that $d/\ell^2 \sim 1/\ell_{ec}$. A more careful analysis shows (Vella *et al.*, 2009*a*) that, in fact,

$$d/\ell^2 \approx \frac{1}{2^{1/2}\pi^2}\ell_{ec}^{-1}. \tag{2.9}$$

Referring to the quantity d/ℓ^2 as the typical curvature of the blister we see that, for small deformations at least, the typical curvature is a constant multiple of ℓ_{ec}^{-1}, independently of the dimensions of the blister (Vella *et al.*, 2009*a*; Aoyanagi *et al.*, 2010). This result is therefore a simple, yet useful method for measuring the elastocapillary length of a system. The question arises, however, of how this result is modified for blisters beyond the small deformation limit. On dimensional grounds d/ℓ^2 must still scale like ℓ_{ec}^{-1} but, as we shall see, the (dimensionless) aspect ratio d/ℓ also plays a role.

2.3. Large deflection analysis

To facilitate our analysis, we first non-dimensionalize the system by letting

$$\tau = T/\Delta\gamma, \quad \delta = d/\ell_{ec}, \quad \lambda = \ell/\ell_{ec}, \quad S = s/\ell_{ec}, \quad L = l_b/\ell_{ec}, \quad \text{etc..} \tag{2.10}$$

The elastica equation (2.7) then becomes

$$\theta_{SS} = -\tau \sin\theta, \tag{2.11}$$

with boundary condition $|\theta_S(\pm L/2)| = \sqrt{2}$.

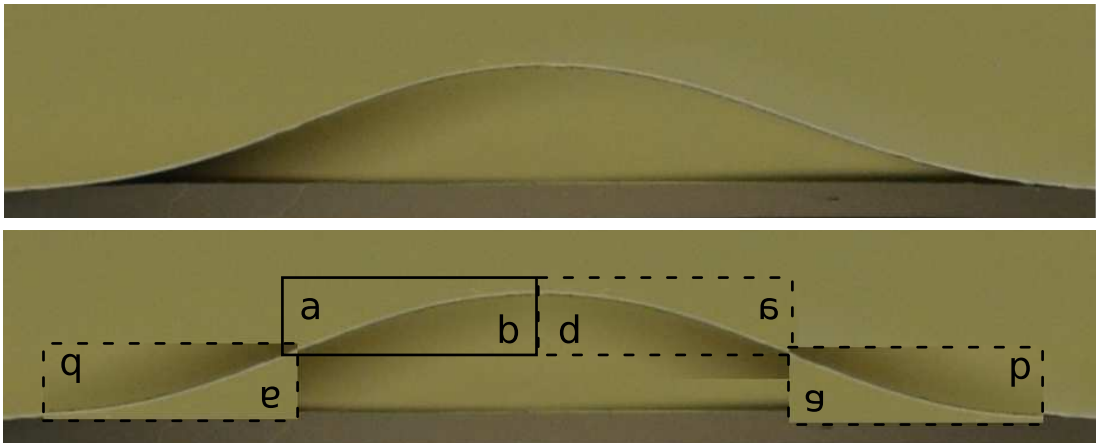

Figure 2.4.: *Top:* Experimental blister ($\ell_{ec} \approx 0.76$ cm), with $\Delta l = 0.03$ cm ($\Delta L \approx 0.04$), leading to $d = 0.17$ cm, $\ell = 1.16$ cm, ($\delta \approx 0.22$, $\lambda \approx 1.53$). *Bottom:* Illustration of the four-fold symmetry of the elastica; the image in the top panel is reconstructed by taking the segment $-l/4 < s < 0$, (solid frame) and rotating and reflecting to form the other images — inversions of the letters **a** and **b** illustrate the different reflexions. Here the sheet thickness is $h = 42$ μm.

Integrating (2.11) once gives

$$\tfrac{1}{2}{\theta_S}^2 = \tau\left(\cos\theta - \cos\theta_0\right), \tag{2.12}$$

where θ_0 is defined as the angle at which the curvature vanishes. Since $\theta = 0$ at the boundary and $\cos\theta$ is a decreasing function, θ_0 is also the maximum value of θ within the sheet. The family of curves that feature such maxima in slope are known as *inflexional* elastica (Love, 1944).

Imposing the delamination condition, we find that the compressive stress τ and maximum angle θ_0 are related by

$$\tau = 1/(1 - \cos\theta_0), \tag{2.13}$$

giving, from (2.12),

$$\theta_S^2 = 2\frac{\cos\theta - \cos\theta_0}{1 - \cos\theta_0}. \tag{2.14}$$

By symmetry, we have that $\theta(-L/2) = \theta(0) = \theta(L/2) = 0$. The angle θ must therefore increase from 0 at $S = -L/2$ up to θ_0 and subsequently decrease from θ_0 to match $\theta = 0$ at $S = 0$. The symmetry of the problem therefore dictates that an inflection point $\theta_S = 0$ must occur at $S = \pm L/4$ so that

$$\theta_S = \sqrt{2}\left(\frac{\cos\theta - \cos\theta_0}{1 - \cos\theta_0}\right)^{1/2} \times \begin{cases} -1, & 0 \leqslant |S| < L/4, \\ +1, & L/4 \leqslant |S| \leqslant L/2. \end{cases} \tag{2.15}$$

We note that this requires that the blister is not only symmetric around $S = 0$ but, further, that the segment $L/4 < |S| < L/2$ is a rotation by 180° of the segment $0 < |S| < L/4$. This rotational and reflectional symmetry (illustrated in figure 2.4) is easily appreciated when considering the analogy between the motion of a pendulum and the shape of an elastica (Levien, 2008). Within this analogy, the four segments of the elastica correspond to the four phases of the pendulum, which are clearly symmetric around the pendulum's lowest point and time reversed around its highest point.

To make further progress requires the determination of the unknown angle θ_0, which in turn requires a relationship between the compression applied, ΔL, and θ_0. Using the symmetry of the problem discussed above, we have that

$$\Delta L = 4\int_0^{L/4} (1 - \cos\theta)\ \mathrm{d}S. \tag{2.16}$$

Making use of the substitution $\mathrm{d}S = \mathrm{d}\theta/\theta_S$ and integrating from $\theta = 0$ to $\theta = \theta_0$, this can be written as

$$\Delta L = 2^{3/2}(1 - \cos\theta_0)^{1/2} \int_0^{\theta_0} \frac{1 - \cos\theta}{\sqrt{\cos\theta - \cos\theta_0}}\ \mathrm{d}\theta.$$

Further letting $\theta = 2\zeta$ and making use of the double angle formulae gives

$$\Delta L = 2^{7/2}\sin(\tfrac{\theta_0}{2}) \int_0^{\theta_0/2} \frac{\sin^2\zeta}{\sqrt{\sin^2\theta_0 - \sin^2\zeta}}\ \mathrm{d}\zeta,$$

which can be written in terms of elliptical integrals as

$$\Delta L = 2^{5/2}(1-\cos\theta_0)\left(F\left[\mathbf{q}\right]-E\left[\mathbf{q}\right]\right), \tag{2.17}$$

where $\mathbf{q} = (\frac{\theta_0}{2}, \csc^2\frac{\theta_0}{2})$, and $F[...]$ and $E[...]$ are the elliptical integrals of the first and second kinds, respectively (Olver *et al.*, 2010), defined by

$$F(\phi,q) = \int_0^\phi \left(1-q\sin^2\theta\right)^{-1/2}\mathrm{d}\theta,$$
$$E(\phi,q) = \int_0^\phi \left(1-q\sin^2\theta\right)^{1/2}\mathrm{d}\theta.$$

The expression (2.17) allows us to obtain the maximum angle as a function of the end-to-end compression, $\theta_0 = \theta_0(\Delta L)$, numerically. Once θ_0 is determined, it is straight-forward

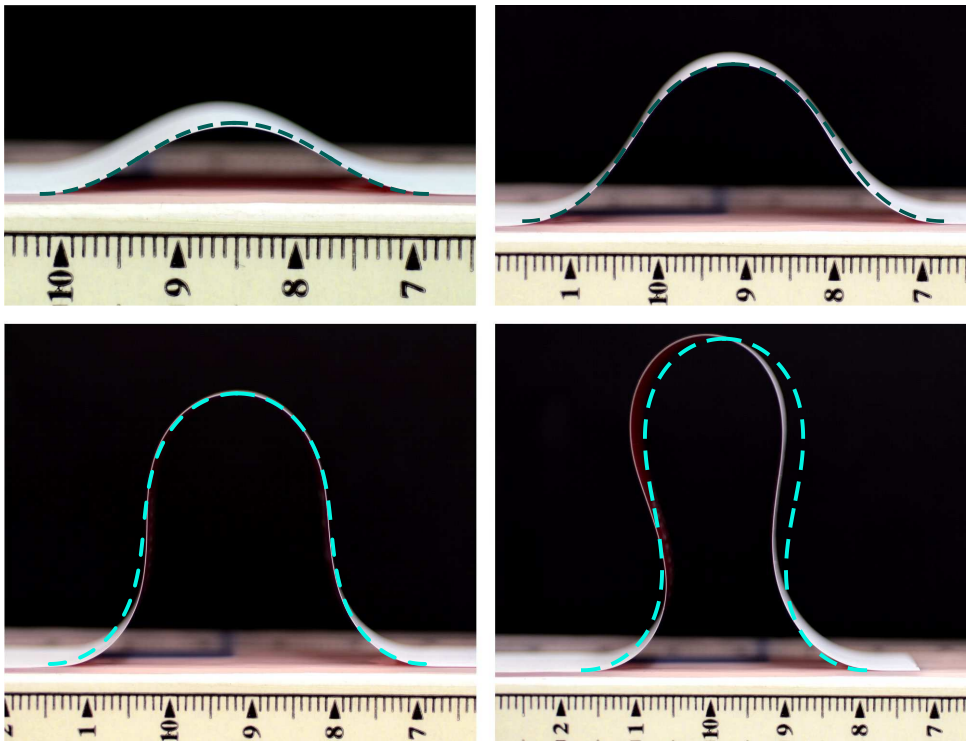

Figure 2.5.: The *'Sticky Elastica'* for $\Delta L = 0.18,\ 1.12,\ 3.25,\ 5.63$, ($\ell_{ec} = 1.35$ cm). In each case the theoretical prediction obtained using the experimentally measured value of Δl gives a good account of the experimentally observed blister shape (dashed curves). Here the sheet thickness $h = 70\ \mu$m, corresponding to black triangles in figures 2.6 and 2.8. Note that there is a loss of symmetry for the largest compression. We believe this to be an effect of the small, but finite, weight of the sheet since the 'heavy' elastica is subject to just such an instability (Domokos *et al.*, 2003; Vella *et al.*, 2009*b*).

to calculate the horizontal and vertical dimensions of the blister as

$$\lambda = \int_{-L/2}^{L/2} \cos\theta \, \mathrm{d}S = 2^{5/2} \left\{ (1 - \cos\theta_0) E\left[\mathbf{q}\right] + \cos\theta_0 F\left[\mathbf{q}\right] \right\}, \tag{2.18}$$

$$\delta = \int_{-L/2}^{0} \sin\theta \, \mathrm{d}S = 2^{3/2}(1 - \cos\theta_0). \tag{2.19}$$

Plots of the (numerically determined) evolution of the blister dimensions with increasing compression are shown for $\lambda = \lambda(\Delta L)$ in figure 2.6a and for $\delta = \delta(\Delta L)$ in figure 2.6b.

The shape of the blister $[X(S), W(S)]$ can also be determined using the analogous integrals

$$X(S) = \int_{-L/2}^{S} \cos\theta(S') \, \mathrm{d}S', \quad W(S) = \int_{-L/2}^{S} \sin\theta(S') \, \mathrm{d}S'. \tag{2.20}$$

This can be compared with results from experiments (see figure 2.5), which are discussed below. We also find that at a critical compression $\Delta L^* \approx 8.71949$ (corresponding to $\lambda^* \approx 1.55502$, $\delta^* \approx 4.13610$) the sheet comes into self-contact, forming a perfect double "SƧ" shape.

2.4. Asymptotic results

While the solution in terms of elliptic integrals is relatively simple to implement computationally, it is of limited use in practical situations. We therefore consider the limit $\Delta L \ll 1$ and derive expansions in powers of ΔL for the quantities of interest. We shall see that these give a very good account of the numerical results even up to self-contact, where ΔL is no longer small. Since the blister dimensions λ and δ are given as functions of the maximum angle θ_0, it is convenient to first compute power series in θ_0 and subsequently relate the results to ΔL via (2.17). The asymptotic result in (2.9) emerges from the leading order behaviour. However, it is possible to do better by retaining the higher order terms in the θ_0 power series expansions.

2.4.1. Blister dimensions, as functions of maximum angle θ_0

The expression for the blister height (2.19) may be expanded as a power series in θ_0 to give

$$\delta(\theta_0) \simeq \sqrt{2}\theta_0^2 - \theta_0^4/6\sqrt{2}. \tag{2.21}$$

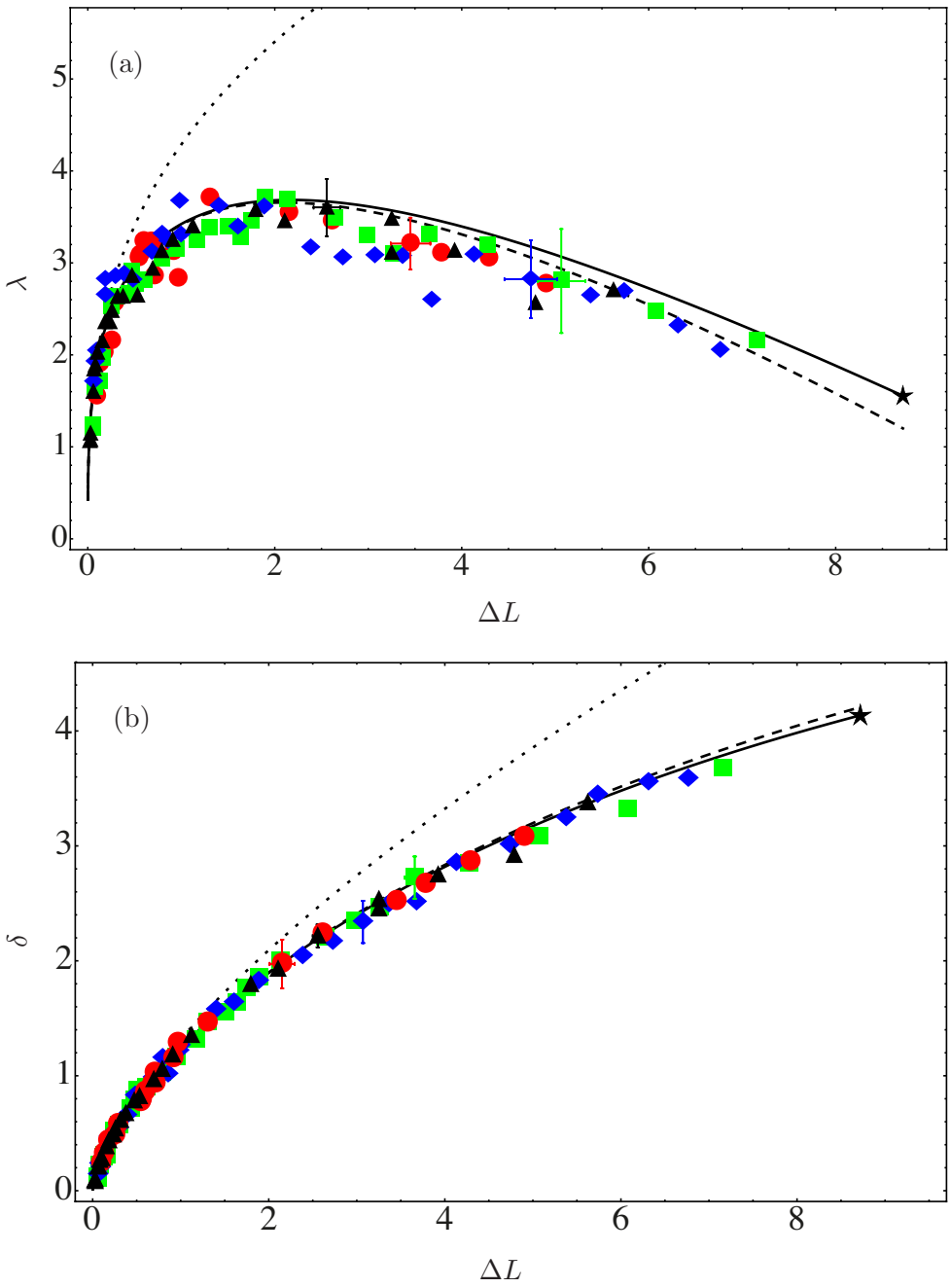

Figure 2.6.: (a) Blister width, λ, as a function of the compression ΔL. The full numerical solution (solid black curve) is partially captured by the first term of the asymptotic expression (dotted). The two term asymptotic approximation (2.28) (dashed) gives a much better prediction and explains the non-monotonic behaviour. Points refer to experimental results obtained with different sheets. Sheet thicknesses are: $h_1 = 52\mu$m (●), $h_2 = 42\mu$m (■), $h_3 = 41\mu$m (◆) and $h_4 = 70\mu$m (▲). Self contact occurs at $\Delta L^* \approx 8.719$, $\lambda^* \approx 1.555$ (★). (b) Blister height, $\delta(\Delta L)$, with asymptotic approximations given by (2.29). The height at self contact is $\delta^* \approx 4.136$. All lengths are non-dimensionalized by ℓ_{ec}, determined using the method described in section 2.5. Typical error bars are shown for each series of experiments.

Rewriting the expression for the blister width, we have

$$\lambda = 2^{3/2}(1-\cos\theta_0)^{1/2}\underbrace{\int_0^{\theta_0}\frac{\cos\theta}{\sqrt{\cos\theta-\cos\theta_0}}\mathrm{d}\theta}_{I(\theta_0)}. \tag{2.22}$$

Letting $u = \sin\theta/\sin\theta_0$, so that $\mathrm{d}u = \mathrm{d}\theta(\sin\theta_0/(1-u^2\sin^2\theta_0)^{1/2})$ and expanding

$$(1-u^2\sin^2\theta_0)^{1/2} \simeq 1-\frac{1}{2}u^2\sin^2\theta_0-\frac{1}{8}u^4\sin^4\theta_0,$$
$$\cos\theta_0 \simeq 1-\frac{1}{2}\sin^2\theta_0-\frac{1}{8}\sin^4\theta_0,$$

we find that

$$I(\theta_0) \simeq \sqrt{2}\int_0^1 \frac{1}{\sqrt{1-u^2}\sqrt{1+\left(\frac{\sin\theta_0}{2}\right)^2(1+u^2)}}. \tag{2.23}$$

Expanding further, we have $1/[1+(\frac{\sin\theta_0}{2})^2(1+u^2)]^{1/2} \simeq 1-\frac{1}{2}(\frac{\sin\theta_0}{2})^2(1+u^2)$ so that $I(\theta_0) = (\pi/\sqrt{2}) - (3\pi/16\sqrt{2})\sin^2\theta_0$. Expanding $\sin^2\theta_0$ about θ_0 we then have

$$I(\theta_0) = \frac{\pi}{\sqrt{2}} - \frac{3\pi}{16\sqrt{2}}\theta_0^2 + \ldots . \tag{2.24}$$

Substituting this result into (2.22) gives a power series expansion for the blister width:

$$\lambda(\theta_0) = \sqrt{2}\pi\theta_0 - \frac{11\pi}{24\sqrt{2}}\theta_0^3 + \ldots . \tag{2.25}$$

Having obtained expressions for $\delta(\theta_0)$ and $\lambda(\theta_0)$ we now seek to eliminate θ_0 in favour of ΔL, since this is the control parameter that is experimentally accessible.

2.4.2. Blister dimensions, as functions of compression ΔL

We have already given an expression for ΔL in terms of elliptical integrals, (2.17). Using procedures analogous to the one in the previous subsection we find the following asymptotic approximations for $F[\mathbf{q}]$ and $E[\mathbf{q}]$:

$$F\left(\frac{\theta_0}{2}, \csc^2\frac{\theta_0}{2}\right) = \frac{\pi}{4}\left(\theta_0 + \frac{\theta_0^3}{48} + \frac{23}{15360}\theta_0^5 + \ldots\right),$$

$$E\left(\frac{\theta_0}{2}, \csc^2\frac{\theta_0}{2}\right) = \frac{\pi}{8}\left(\theta_0 - \frac{\theta_0^3}{96} - \frac{7}{15360}\theta_0^5 - \ldots\right).$$

Substituting this into (2.17) and keeping terms to second order, we have

$$\Delta L \simeq \frac{\pi}{2\sqrt{2}}\left(\theta_0^3 - \frac{1}{32}\theta_0^5\right). \tag{2.26}$$

To invert this expression and find $\theta_0 = \theta_0(\Delta L)$ for $\Delta L \ll 1$, we assume a power series of the form

$$\theta_0 = \left(\frac{2\sqrt{2}}{\pi}\Delta L\right)^{1/3} + \alpha_2 \Delta L^{2/3} + \alpha_3 \Delta L + \dots\,, \tag{2.27}$$

and choose the coefficients α_2, α_3 to satisfy (2.26). We find $\alpha_2 = 0$, $\alpha_3 = 1/24\pi$ giving

$$\theta_0(\Delta L) \simeq \sqrt{2}\left(\frac{\Delta L}{\pi}\right)^{1/3} + \frac{1}{24\sqrt{2}}\left(\frac{\Delta L}{\pi}\right).$$

Substituting this into the asymptotic expressions for $\lambda(\theta_0)$ and $\delta(\theta_0)$ produces the following results:

$$\lambda = 2\pi^{2/3}\Delta L^{1/3} - \frac{7}{8}\Delta L + \dots\,, \tag{2.28}$$

$$\delta = 2\sqrt{2}\left(\frac{\Delta L}{\pi}\right)^{2/3} - \frac{1}{2\sqrt{2}}\left(\frac{\Delta L}{\pi}\right)^{4/3} + \dots\,. \tag{2.29}$$

The one-term and two-term asymptotic expansions for $\lambda(\Delta L)$ and $\delta(\Delta L)$ are shown in figures 2.6a and 2.6b, respectively. These demonstrate that, although only strictly being valid for $\Delta L \ll 1$, the two-term expansion compares extremely well with the numerical results even for $\Delta L \approx 8$, i.e. close to self-contact. That the expressions (2.28) and (2.29) indeed constitute the leading order terms of the respective expansions is supported by figure 2.7. It shows plots of the errors in the asymptotic results $\mathcal{E}_\lambda = \lambda - [2\pi^{2/3}\Delta L^{1/3} - \frac{7}{8}\Delta L]$ and $\mathcal{E}_\delta = \delta - [2\sqrt{2}(\Delta L/\pi)^{2/3} - \frac{1}{2\sqrt{2}}(\Delta L/\pi)^{4/3}]$. As expected, these errors are found to scale linearly with $\Delta L^{5/3}$ and ΔL^2, respectively, which are the scalings of the third order terms in the expansions of λ and δ.

We note that the evolution of $\lambda(\Delta L)$ is non-monotonic (see fig. 2.6a), decreasing for $\Delta L \gtrsim 64\pi/21^{3/2} \approx 2.0894$. While the asymptotic expression for δ likewise predicts a maximum height this only occurs for $\Delta L \approx 8\pi$, which is far beyond the point of self contact, ΔL^*, and hence is not physically realizable. The non-monotonicity of the blister width, λ, is observed in other, related, systems (see next chapter, Wagner & Vella (2011)). However, it is not observed with the classic elastica, for which λ decreases monotonically as the compression is increased. The non-monotonic behaviour observed for the Sticky Elastica is caused by the fact that the arc-length of the blistered region initially increases rapidly with increasing compression; this increasing length of the buckled region overcomes the decrease caused by compression and so λ initially increases with ΔL. However, with

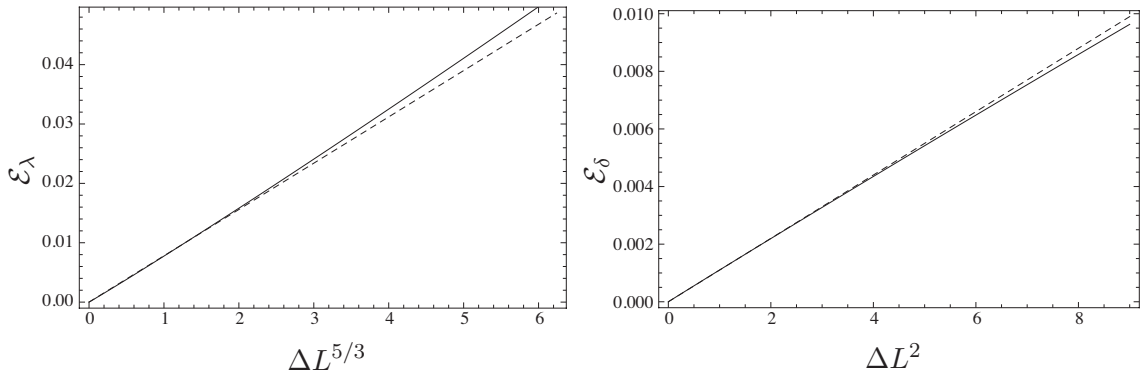

Figure 2.7.: Graphs showing the errors in the asymptotic expansions, $\mathcal{E}_\lambda(\Delta L^{5/3})$ and $\mathcal{E}_\delta(\Delta L^2)$ (solid curves). To a good approximation, the errors scale linearly with $\Delta L^{5/3}$ and ΔL^2 (dashed lines), which are the scalings of the next higher order terms in the asymptotic expansions. The upper limit corresponds to $\Delta L = 3$ for both plots.

still larger compression, the increase of arc-length slows and is not large enough to keep up with the imposed compression: λ reaches a maximum value and begins to decrease. It is also interesting to observe that, except for very small compressions ($\Delta L \lesssim 0.3$), the dependence of blister width on ΔL is relatively weak; we therefore propose that, as a rule of thumb, $\ell \approx 3\ell_{ec}$. This result provides a quick way to get a rough estimate for the elastocapillary length by looking just at the typical width of the blisters in a system. This gives further justification to the assumption that the blister width is roughly constant in delamination buckling, an assumption often called upon in previous analyses of the fracture mechanics of delamination (Hutchinson & Suo, 1992).

Using the asymptotic results from (2.28) – (2.29), we now return to the question of central interest here: how does the typical curvature d/ℓ^2 relate to the elastocapillary length and the aspect ratio of the blisters?

2.4.3. Typical curvature vs aspect ratio

Considering the aspect ratio, δ/λ, bears two major advantages: firstly, it is easily accessible from an experimental viewpoint and secondly, it is a non-dimensional quantity that is known independently of the elastocapillary length. In fact, the non-dimensional nature of the aspect ratio can be exploited to find estimates of ℓ_{ec} for large deformations, as we shall see shortly.

We aim to write the typical curvature as a function of the aspect ratio. To this end we write, from (2.21) and (2.25)

$$\frac{\delta}{\lambda} = \frac{\theta_0}{\pi} + \frac{7}{48\pi}\theta_0^3 + ... \tag{2.30}$$

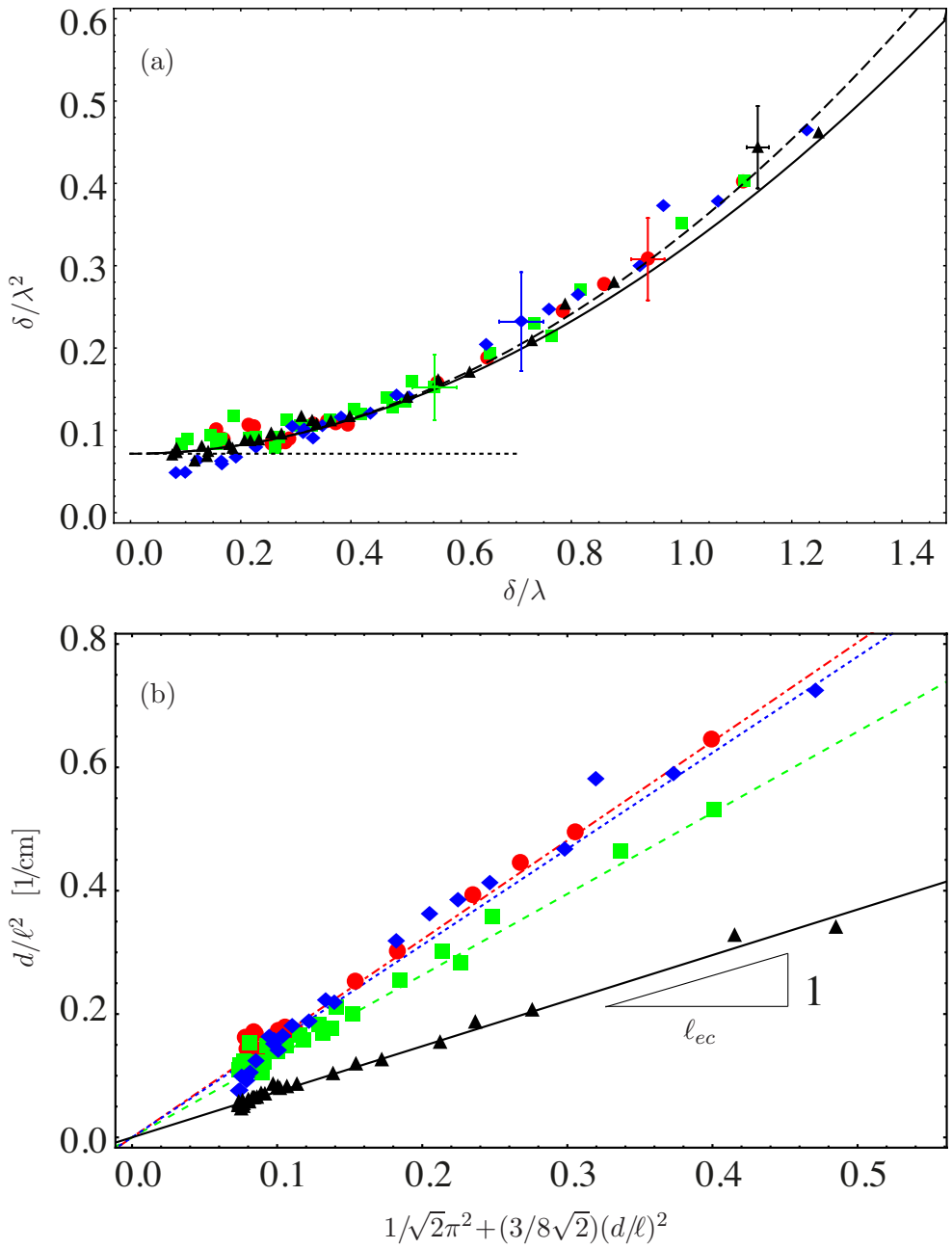

Figure 2.8.: (a) Dimensionless typical curvature of blisters δ/λ^2 as a function of the aspect ratio δ/λ. Shown are the full numerical solution, (solid black), along with the first order (dotted) and second order asymptotic approximations (2.33), (dashed). Points refer to sheets of different thickness: $h_1 = 52\mu$m (●), $h_2 = 42\mu$m (■), $h_3 = 41\mu$m (◆) and $h_4 = 70\mu$m (▲). The point of self contact lies outside the plot range shown, at $\delta^*/\lambda^* \approx 2.660$, $\delta^*/\lambda^{*2} \approx 1.710$. All lengths are non-dimensionalized by ℓ_{ec}. Error bars are representative of each set of experiments. (b) Determination of the elastocapillary length, ℓ_{ec}, from the dimensional value of the typical curvature d/ℓ^2, for the four sets of experiments discussed. The straight lines represent best fits to the raw data whose slope provides an estimate for the quantity $1/\ell_{ec}$ (see text).

while the typical curvature may be written as

$$\frac{\delta}{\lambda^2} = \frac{1}{\sqrt{2}\pi^2} + \frac{3}{8\sqrt{2}\pi^2}\theta_0^2 + \dots \,. \tag{2.31}$$

As in our earlier analysis, we pose the power series expansion

$$\theta_0 = \pi\delta/\lambda + \alpha_2(\delta/\lambda)^2 + \alpha_3(\delta/\lambda)^3 + \dots \tag{2.32}$$

and choose the coefficients α_2, α_3 etc. to satisfy (2.30). We find that $\alpha_2 = 0$, $\alpha_3 = -(7/48)\pi^3$. Substituting (2.32) into (2.31) finally gives

$$\frac{\delta}{\lambda^2} = \frac{1}{\sqrt{2}\pi^2} + \frac{3}{8\sqrt{2}}\left(\frac{\delta}{\lambda}\right)^2 - \dots \,. \tag{2.33}$$

Thus, in the limit of small blisters we recover the result (2.9). However, as δ/λ increases the typical curvature grows roughly quadratically. We also note that the asymptotic relationship (2.33) agrees with the results of the numerical calculations, as shown in fig. 2.8.

2.5. Experiments

I tested the preceding theoretical analysis using a set of desktop experiments at a macroscopic scale. I used plastic sheets of different thicknesses adhered to tacky rubber surfaces (fabricated from Zhermack dental polymer). The sheets used were uniform strips of adhesive tape (thickness $h_1 = 52$ μm, red circles in figures 2.6 and 2.8) and other thin elastic sheets without an adhesive coating, which were obtained from the labels of commonly available drink bottles (Aquafina, $h_2 = 42$ μm, green squares; Copella, $h_3 = 41$ μm, blue diamonds; and Vitamin Water $h_4 = 70$ μm, black triangles in figures 2.6 and 2.8). The Young's modulus of these sheets was measured using the deflection of the sheets under their own weight. It was found that $E_2 \simeq 0.70$ GPa, $E_3 \simeq 0.77$ GPa and $E_4 \simeq 0.75$ GPa. Estimation of E_1 (the sticky tape) was made difficult due to a slight intrinsic curvature of the tape. However, since the differences in the Young's moduli were observed to be within the experimental error, we proceed by taking $E = 0.7 \pm 0.1$ GPa for all sheets.

For the adhesion experiments described here, the sheets were cut into strips of width 1 cm and length 10 cm. The ends of these strips were brought together by a distance Δl and the strip then brought into contact with the substrate. Upon deposition the strip was forced into adhesion beyond its equilibrium state by applying pressure over almost the entire strip (missing out the central blistered part and avoiding the plastic deformations

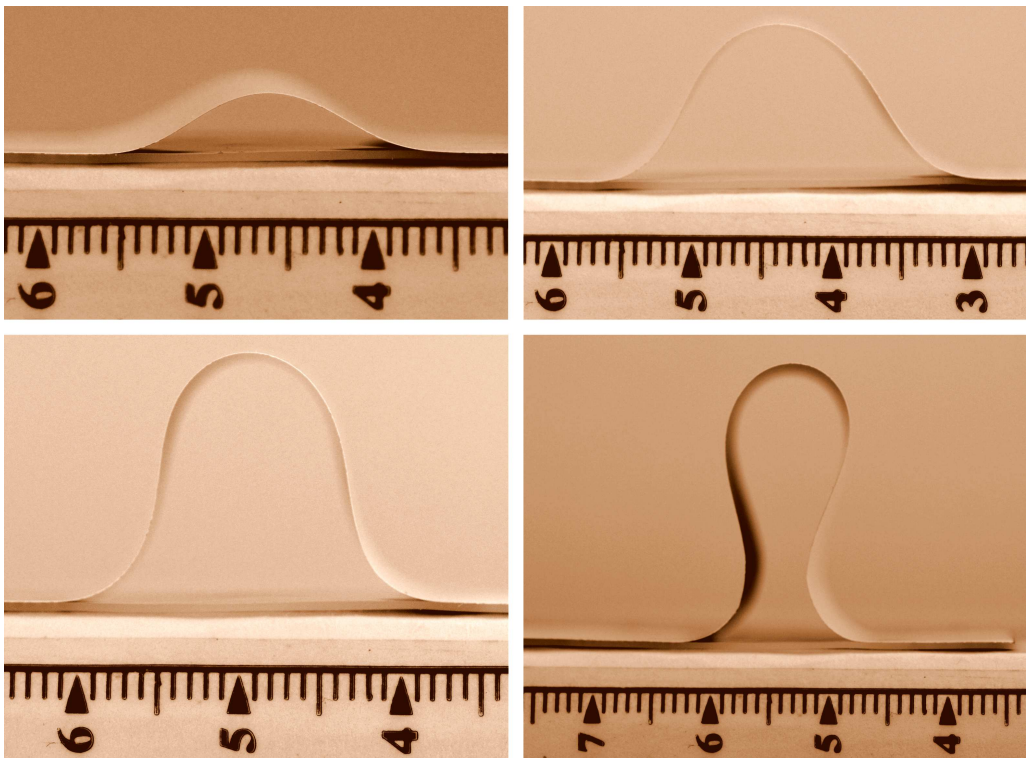

Figure 2.9.: Sticky Elastica experiment with a sheet of thickness $h = 41\ \mu$m, ($\ell_{ec}^{(3)} = 0.64$ cm), corresponding to blue diamonds in figures 2.6 and 2.8. The compressions are $\Delta l = 0.47,\ 1.49,\ 2.61,\ 4.30$ cm. Note again that there is a loss of symmetry for the largest compression due to gravity, as in figure 2.5.

that occur for very high curvatures). Once the external pressure is removed, the strip spontaneously de-adheres until reaching an equilibrium state in which the length of its de-adhered portion, l_b, is well-defined, as shown in figures 2.5, 2.9. The results of experiments performed in this way were robust and reproducible.

The dimensions d and ℓ of the blisters in equilibrium were measured for a range of the end-to-end compression Δl. A comparison of experimental and theoretical predictions is given in figures 2.6 and 2.8. To plot these in dimensionless form the elastocapillary length for each strip-substrate pair had to be determined. This was done by plotting the dimensional values of d/ℓ^2 against the dimensionless quantity $1/\sqrt{2}\pi^2 + (3/8\sqrt{2})(d/\ell)^2$; equation (2.33) leads us to expect that such a plot should yield a straight line with slope $1/\ell_{ec}$ allowing the value of ℓ_{ec} to be estimated. Such a plot is shown in figure 2.8b and demonstrates the expected linear behaviour. We therefore believe that this method represents an effective method for determining the elastocapillary length in scenarios where the aspect ratio d/ℓ is not small. We find for the adhesive tape $\ell_{ec}^{(1)} = 0.62$ cm and for the non-adhesive tapes $\ell_{ec}^{(2)} = 0.76$ cm, $\ell_{ec}^{(3)} = 0.64$ cm and $\ell_{ec}^{(4)} = 1.35$ cm. From this we infer for the adhesive tape $\Delta\gamma^{(1)} \simeq 0.25\ \mathrm{Jm}^{-2}$ and for the non-adhesive tapes

$\Delta\gamma^{(2-4)} \simeq 0.08 - 0.13$ Jm^{-2}. This is comparable to values obtained in similar studies (Vella *et al.*, 2009*a*).

The agreement between theory and experiment shown in figures 2.6 and 2.8 seems to be reasonably robust given the relative difficulty in measuring the exact blister width ℓ (rather than blister height d, which is much easier to measure). This is particularly important in figure 2.8, due to the ℓ^{-2} dependence of the typical curvature and the $(d/\ell)^2$ term in (2.33). We note from both figures that the agreement between experimental and asymptotic results is better than that between experimental and numerical results; we attribute this to the fact that the value of ℓ_{ec} was determined by using the asymptotic result (2.33), rather than the full theoretical solution. Attempts to use higher order asymptotic expansions fail because of the compounding of the error in the measurement of ℓ that occurs when computing $(d/\ell)^4$ and higher order terms.

2.6. Conclusions

In this chapter we have presented numerical results for the shape and dimensions of delamination blisters allowing for the possibility that the slope of the blister may become large. An asymptotic analysis yielded simple expressions for the dimensions of the blisters, which are in excellent agreement with numerical results up to the point of self-contact, where $\Delta L \approx 8$. This is particularly striking, since the asymptotic calculations are only strictly valid in the limit $\Delta L \ll 1$. The success of these asymptotic results also enabled us to propose a straight-forward way to estimate the strength of adhesion based on the geometry of delamination blisters beyond the limit of small deformations. We tested this technique with a series of simple table-top experiments obtaining good agreement between experiment and theory with a single fitting parameter: the elastocapillary length ℓ_{ec}, which relates the bending rigidity of the film and the adhesive energy.

Our study was motivated by the controlled use of delamination in technologies at small scales, most notably in flexible electronics. In these situations, the deformation of the delaminated components is often not small and so we expect that our results would be of use in such applications, albeit provided that a simple adhesion is used, rather than the patterning that is currently common (Sun *et al.*, 2006). In our analysis, we have assumed that there is no relative motion between strip and substrate. In reality, this can be achieved in two ways: (i) the sheet is confined *before* it is brought in contact with the rigid substrate (as in the experiments presented here) or (ii) the (relatively stiff) strip is initially flat and adhered to a compressible substrate. If the *entire* strip-substrate system is then compressed, the strip is forced to buckle out of plane and delaminate from the substrate forming a delamination blister.

The main difference of our work to the canonical studies of delamination (Cotterell & Chen, 2000; Yu & Hutchinson, 2002) is that the width of the blister is not fixed *a priori* but is rather determined by a balance between bending and adhesive forces at a fixed compression Δl. Nevertheless, our analysis shows that, in fact, as the compression is increased the preferred size of this blister changes only very slightly.

An important feature of blisters in flexible electronic applications is that the buckled components should retain a sufficiently small curvature so that they do not deform plastically under repeated flexing. Here, we assume that this condition is satisfied provided that the stress within the beam, σ, does not reach the yield stress, σ_y. From linear elasticity theory, the maximum bending stress within a sheet occurs at the surfaces $z = \pm h/2$ of the sheet. Therefore, if the sheet is deformed to have a maximum curvature $|\theta_s|_{\mathrm{Max}}$ then $\sigma_{\mathrm{Max}} = Eh|\theta_s|_{\mathrm{Max}}/2(1-\nu^2)$ (Mansfield, 1989) and we have that no failure will occur provided that

$$\sigma_y > \sigma_{\mathrm{Max}} = \frac{Eh}{2(1-\nu^2)}|\theta_s|_{\mathrm{Max}}. \tag{2.34}$$

However, our analysis has shown that for the Sticky Elastica, the maximum curvature occurs at $s = 0, \pm l_b/2$ and has value $|\theta_s|_{\mathrm{Max}} = \sqrt{2}/\ell_{ec}$, see (2.8). Buckling will therefore occur without plastic deformation provided that

$$\frac{\sigma_y^2 h}{E\Delta\gamma} > \frac{6}{1-\nu^2}, \tag{2.35}$$

i.e. provided that the thickness is large enough for given material properties, or provided the substrate–strip adhesion is sufficiently weak. We note that this result is precisely the same as that derived previously from linear considerations (Vella *et al.*, 2009*a*) but applies independently of the degree of compression, since the maximum curvature is given solely by the elastocapillary length ℓ_{ec}. In other words, the sheet is no more likely to fail for larger compressions than for the initial delamination event – if it survives the original deformation it can safely be compressed further.

Appendix

2.A. The relative importance of gravity

To consider the effect of gravity on the Sticky Elastica, we note that gravity modifies the classic elastica equation (2.7) to give the heavy elastica equation (Vella *et al.*, 2009*b*)

$$\mathcal{B}\theta_{ss} = -T\sin\theta + \rho g h(l_b/2 - s)\cos\theta, \tag{2.36}$$

which upon non-dimensionalization, using (2.10), becomes

$$\theta_{SS} = -\tau\sin\theta + \frac{\rho g h l_b}{\Delta\gamma}\left(\tfrac{1}{2} - S/L\right)\cos\theta, \tag{2.37}$$

This non-dimensionalization suggests that the effect of gravity is captured by the dimensionless parameter

$$\epsilon \equiv \rho g h l_b/\Delta\gamma, \tag{2.38}$$

which is a measure of the weight of the sheet, relative to the strength of adhesion. In systems where $\epsilon \ll 1$, the last term in (2.36) may be neglected so that we recover the elastica equation

$$\theta_{SS} = -\tau\sin\theta, \tag{2.39}$$

which corresponds to (2.7) above. The values of ϵ in the experiments described here range from $\epsilon_1 \approx 0.03$ (for the adhesive tape, $\rho_1 \approx 650$ kg/m^3, $\Delta\gamma_1 = 0.25$, $l_{b1} = 2.3$ cm, $h_1 = 52$ μm) to $\epsilon_4 \approx 0.15$ (for non-adhesive tape, $\rho_4 \approx 600$ kg/m^3, $\Delta\gamma_4 = 0.13$, $l_{b4} = 5.0$ cm, $h_4 = 70$ μm) and thus largely satisfy the requirement $\epsilon \ll 1$. It is clear that the finite weight of the sheet does have a small effect, since the loss of symmetry for highly compressed states (bottom right of figure 2.5) cannot be explained by the classical elastica equation. For flexible electronic applications ϵ will be significantly smaller than 1.

Chapter 3

Compression-Induced Delamination of Floating Elastic Sheets

Synopsis

We investigate the deformation of a thin elastic sheet floating at the surface of a liquid bath and subject to a uniaxial compression. We show that at a critical compression the sheet delaminates from the liquid over a finite region forming a delamination blister. This blistering regime adds to the wrinkling and localized folding regimes that have been studied previously. The transition from wrinkled to blistered states occurs when delamination becomes energetically favourable in comparison to wrinkling. We determine the initial blister size and the evolution of blister size with continuing compression. We compare our theoretical results with experiments at a macroscopic scale.

3.1. Introduction

The Sticky Elastica, rucks in rugs (Vella *et al.*, 2009*b*; Kolinski *et al.*, 2009), surfactant monolayers lining our lungs (Lipp *et al.*, 1998; Diamant *et al.*, 2001), the formation of mountain ranges (Ramberg & Stephansson, 1964) and flexible electronic devices (Rogers *et al.*, 2010; Wang *et al.*, 2010) — all exhibit variants of Euler's classic beam buckling with two additional features: buckling takes place on a substrate and the structure that results has a length scale that is not simply the system size. In the cases of the Sticky Elastica and the ruck in a rug, the substrate is essentially undeformable and the buckled region has a finite size because of additional forces that are acting on the system: the adhesion between sheet and substrate for the Sticky Elastica, the gravitational bending of the beam due to its own weight for the ruck in a rug. In the other cases, the substrate is deformable and the degree of this deformability controls the characteristic size of the buckling pattern that results (Groenewold, 2001). Recently, systems featuring deformable substrates have seen a sharp rise of interest (Reis *et al.*, 2009; Leahy *et al.*, 2010; Brau *et al.*, 2011), motivated by a wealth of new applications, for example in optical devices (Bowden *et al.*, 1998) or the measurement of elastic moduli in thin films (Stafford *et al.*, 2004).

At its simplest, we may envisage an elastic sheet floating on the surface of a liquid and subject to uniaxial compression. It is well known that, for compressive forces above a critical value, the sheet wrinkles with a wavelength determined by a balance between resistance to bending (which penalizes short, highly curved wrinkles) and the gravitational energy of the displaced liquid (which penalizes long, large amplitude wrinkles) (Landau & Lifschitz, 1970).

Recently, the appearance of localized features, known as folds, has seen a great deal of attention. Folds supersede wrinkles at large compressions (Pocivavsek *et al.*, 2008; Brau *et al.*, 2011). When folding, the sheet remains completely adhered, and folds are most commonly observed to 'grow into' the substrate; as shown in figure 3.1b. Considering a linear elastic sheet on a neo-Hookean substrate, recent numerical experiments have found that folds can also 'grow out of' the substrate, lifting part of the substrate up as they form (Cao & Hutchinson, 2012). In this case, they are sometimes referred to as 'ridges'.

One of the subjects of recent theoretical work has been a debate over whether these localized structures, i.e. folds, emerge from uniformly wrinkled states at a critical compression (Pocivavsek *et al.*, 2008) or continuously. Diamant & Witten (2010) argue that the appearance of folds at a critical compression is a result of the finite size of the system and that, for an infinite system, the localized state is always energetically favourable.

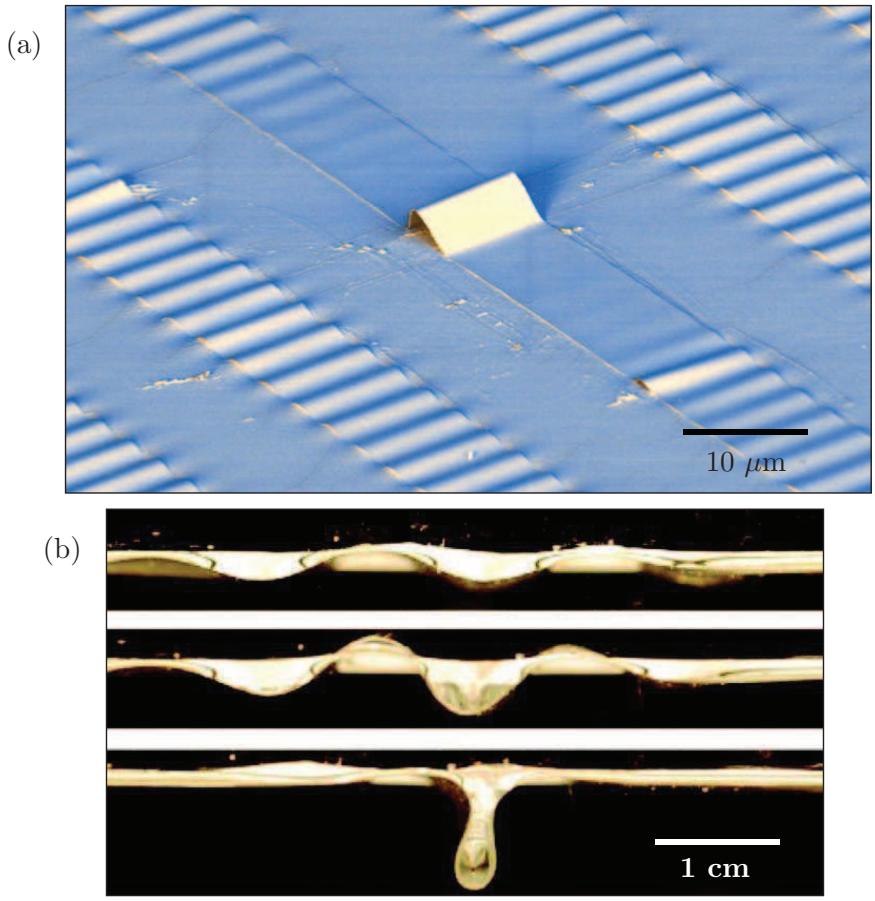

Figure 3.1.: (a) Wrinkle to blister transition for a GaAs film deposited on an elastic PDMS substrate (reproduced from Rogers & Huang (2009)). The image illustrates how the occurrence of a localized blister is accompanied by a relaxation of wrinkles on either side. (b) Wrinkle to fold transition for increasing compression ΔL for a polyester film on water, reproduced from Pocivavsek *et al.* (2008).

They subsequently presented a closed-form solution for the shape of geometrically nonlinear folds in an elastic sheet floating on the surface of a liquid bath (Diamant & Witten, 2011).

Previous studies of the wrinkle-to-fold transition have assumed that the sheet remains in contact with the liquid everywhere along its length. However, if the liquid is replaced by a soft elastic solid, it is often observed that the thin sheet delaminates from the substrate forming delamination 'blisters' (Parry *et al.*, 2005; Mei *et al.*, 2007; Vella *et al.*, 2009*a*), much like those discussed in Chapter 2. The formation of these localized blisters is a discontinuous process occuring at a finite compression. The relevance of the wrinkling-to-blistering transition to modern technologies is illustrated in figure 3.1a, which shows a setup relevant for flexible electronics applications (Rogers *et al.*, 2010). Here the blistering is crucial for the proper functioning of the device. However, a comprehensive theoretical

study of when the blistering transition occurs is complicated by the nonlinear response of the elastic substrate to deformation (Groenewold, 2001; Parry *et al.*, 2005; Brau *et al.*, 2011). In this chapter we show that an analogous transition occurs in the case of a sheet floating at a liquid surface. This demonstrates a new response of such systems, and the simple mechanical response of a liquid bath allows us to characterise this transition theoretically. We confirm our theoretical results with experiments at a macroscopic scale.

A paper based on the work described in this chapter has been published in *Physical Review Letters*, (Wagner & Vella, 2011). The work was performed under the supervision of Dominic Vella. Experiments were performed with help from Roiy Sayag (supplying the potassium carbonate solutions) and David Page-Croft (assistance with the manufacture of the thin elastic sheets).

3.2. Theoretical formulation

We consider an elastic sheet of density ρ and thickness h, floating on a liquid of density ρ_l (see figure 3.2). The length of the sheet is l and the two ends of the sheet are clamped. The ends are then brought closer together by an amount Δl. We proceed by first considering each of the possible states of the system (wrinkled and blistered) separately. Subsequently, we compare the energy of each state to determine the transition between them.

3.2.1. Wrinkled states

Take a sheet that is in contact with the liquid over its entire length. We denote the coordinates of a point on the centreline of the sheet by $[x(s), w(s)]$ where s is the arc-length, measured from the midpoint of the centreline. The deformed shape of the sheet can be found by minimizing the energy of the system,

$$U = \int_{-l/2}^{l/2} \left\{ \tfrac{1}{2}\mathcal{B}\theta_s^2 + \rho g h w + \tfrac{1}{2}\rho_l g w^2 \cos\theta \right\} \, \mathrm{d}s, \tag{3.1}$$

subject to the familiar geometric constraint

$$\Delta l = \int_{-l/2}^{l/2} (1 - \cos\theta) \, \mathrm{d}s. \tag{3.2}$$

In (3.1), the first two terms correspond to the bending and gravitational potential energies of the sheet, respectively, with $\mathcal{B}$ the bending stiffness, and g the acceleration due to gravity. The third term corresponds to the gravitational potential energy of the displaced

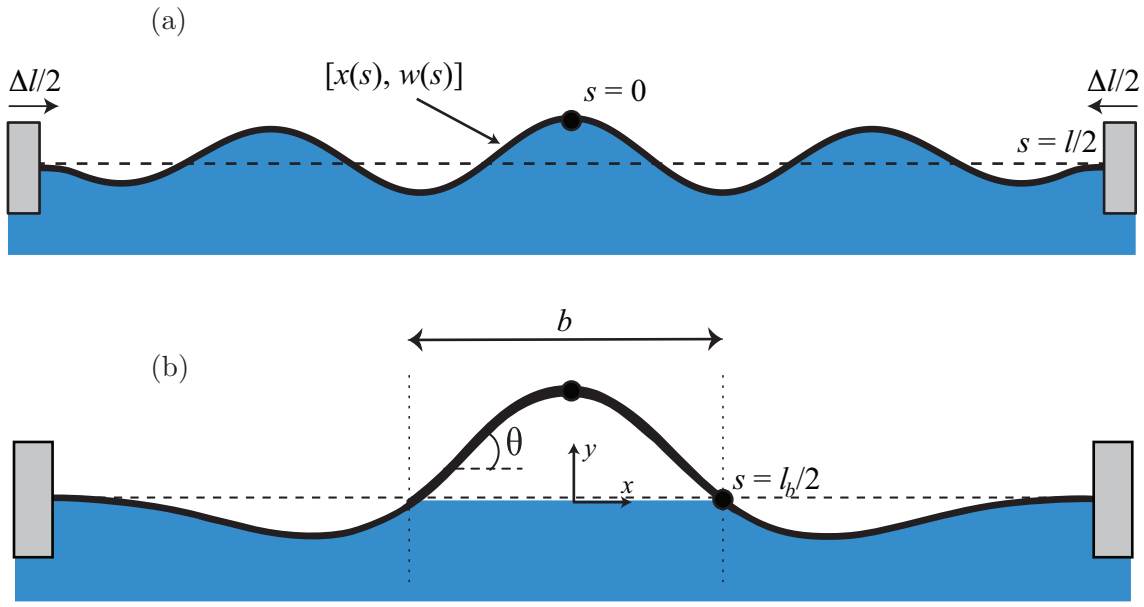

Figure 3.2.: Schematic diagram of a sheet floating on the surface of a liquid bath and subject to a uniaxial compression Δl. (a) The sheet exhibits symmetric wrinkling, extending over the length of the sheet. (b) The compression is such that the sheet delaminates from the liquid over a horizontal distance b, forming a delamination blister.

liquid. For a liquid element of area $\mathrm{d}x\mathrm{d}y$, displaced by a height y, this energy is $\rho_l g y \mathrm{d}x\mathrm{d}y$. The total hydrostatic energy from the displaced liquid is then

$$U_l = \int_{x(-l/2)}^{x(l/2)} \int_0^w \rho_l g y \ \mathrm{d}y \ \mathrm{d}x = \int_{-l/2}^{l/2} \tfrac{1}{2}\rho_l g w^2 \cos\theta \ \mathrm{d}s.$$

Before applying the Euler-Lagrange equations to extremize the energy (3.1) with constraint (3.2), we first rewrite the integrand in terms of w and its derivatives alone. To do this we make use of the relations $x_s = \cos\theta$ and $w_s = \sin\theta$, which allow us to write $\theta_s = w_{ss}/x_s = w_{ss}/\sqrt{1-w_s^2}$.

From this we find the equation of equilibrium,

$$\mathcal{B}\left[\left(\frac{w_{ss}}{1-w_s^2}\right)_s - \frac{w_{ss}^2 w_s}{(1-w_s^2)^2}\right]_s + T\left(\frac{w_s}{\sqrt{1-w_s^2}}\right)_s + \rho g h = -\rho_l g\left[\left(\frac{w^2 w_s}{2\sqrt{1-w_s^2}}\right)_s + w\sqrt{1-w_s^2}\right],$$

which is identical to the result given in Diamant & Witten (2010) plus the additional gravity term $\rho g h$ (taking into account the finite weight of the sheet, in contrast to the previous work). Here, T is the compressive force applied, which emerges as the Lagrange multiplier associated with the geometric constraint, (3.2).

Resubstituting θ, this can be simplified to give

$$\left(\frac{\mathcal{B}\theta_{ss} + T\sin\theta + \rho g h s\cos\theta}{\cos\theta}\right)_s = -\frac{\rho_l g}{2w_s}\left(\frac{w^2}{\cos\theta}\right)_s \tag{3.3}$$

The balance between bending stiffness and hydrostatic pressure leads to a natural length-scale for floating sheets,

$$\ell_w \equiv (\mathcal{B}/\rho_l g)^{1/4}. \tag{3.4}$$

Physically, the length ℓ_w is related to the wavelength of the wrinkling instability that occurs when a floating sheet is compressed (Landau & Lifschitz, 1970). We use ℓ_w to non-dimensionalize lengths so that

$$S = s/\ell_w, \quad X = x/\ell_w, \quad B = b/\ell_w, \quad \Delta L = \Delta l/\ell_w, \quad \text{etc..} \tag{3.5}$$

However, we let $W = (w - w_\infty)/\ell_w$ where $w_\infty \equiv h(1/2 - \rho/\rho_l)$ is the depth of the centreline below the liquid when freely floating; W measures deflections of the sheet centreline from its equilibrium floating position. We also introduce a dimensionless compressive force $\tau = T/(\mathcal{B}\rho_l g)^{1/2}$.

The balance between gravity and bending stiffness of the sheet leads to a second characteristic length-scale, the elasto-gravitational length, $\ell_g = (\mathcal{B}/\rho g h)^{1/3}$. It is a measure of the typical length that a sheet requires to deform under its own weight (Vella *et al.*, 2009*b*). The two lengths ℓ_w and ℓ_g combine to introduce an important parameter,

$$\delta \equiv (\ell_w/\ell_g)^3 = \rho h/\rho_l \ell_w, \tag{3.6}$$

where δ is the dimensionless draft of the sheet.

The dimensionless version of (3.3) is then written as

$$\left(\frac{\theta_{SS} + \tau\sin\theta + S\delta\cos\theta}{\cos\theta}\right)_S = -\frac{1}{2W_S}\left(\frac{W^2}{\cos\theta}\right)_S. \tag{3.7}$$

Assuming symmetric wrinkling, we restrict the problem to $0 \le S \le L/2$ and impose the symmetry conditions

$$\theta(0) = \theta_{SS}(0) = 0, \qquad X(0) = 0, \tag{3.8}$$

together with clamped boundary conditions at $S = L/2$,

$$\theta(L/2) = W(L/2) = 0. \tag{3.9}$$

Equation (3.7), together with $X_S = \cos\theta$ and $W_S = \sin\theta$, describes a system of one third order ODE, two first order ODEs and one unknown parameter, τ. This system is completely determined by the set of five boundary conditions (3.8) – (3.9) plus the constraint (3.2) and can be solved using numerical boundary value problem solvers, such as the MATLAB routine `bvp4c`.

Away from the clamped boundaries the solutions are found to be periodic of the form $w(s) = a\cos(ks)$, where the amplitude $a \sim \ell_w\sqrt{\Delta l/l}$ and $k = 2\pi/\ell_w$. The wrinkles are further found to extend over the whole length of the system. Writing the dimensionless energy as $\mathcal{U} = U/(\mathcal{B}/\ell_w)$, the energy in the wrinkled state can be shown to be

$$\mathcal{U}^{(w)} = 2\Delta L - \Delta L^2/L, \tag{3.10}$$

to second order in ΔL (Cerda & Mahadevan, 2003; Diamant & Witten, 2010).

3.2.2. Blistered states

We now envisage that a symmetrical delamination blister forms in the region $-L_b/2 \leq S \leq L_b/2$, (figure 3.2b) whose shape is to be determined along with the shape of the sheet in the region that is still wetted, $L_b/2 < |S| < L/2$. The (non-dimensional) energy of the system is now written as

$$\mathcal{U} = \int_{-L/2}^{L/2} \left\{ \tfrac{1}{2}\theta_S^2 + W\delta + \tfrac{1}{2}\, W^2 \cos\theta \mathcal{H}(|S| - L_b/2) \right\}\, \mathrm{d}S, \tag{3.11}$$

where the Heaviside step-function $\mathcal{H}(x)$ ensures that liquid is only displaced in the region $L_b/2 < |S| < L/2$. Furthermore, the length constraint (3.2) still applies.

In addition to the elasto-gravitational energy given in (3.11), we need to include the surface energy penalty due to delamination. Assuming that the blistered part remains wet, as has been reported in related problems (Chopin *et al.*, 2008), this surface energy is (in dimensional terms)

$$U_s^{(b)} = \gamma_{lv}(b + l_b)$$

where γ_{lv} is the energy per unit area of the liquid–vapour interface. For non-wetted blisters on the other hand, the surface energy takes the familiar form $U_s^{(b)} = (\gamma_{lv} + \gamma_{sv} - \gamma_{sl})l_b \equiv \Delta\gamma l_b$, where $\Delta\gamma$ is therefore defined as in (1.12), the solid substrate being replaced by a liquid. Note that we omitted the surface energy penalty $\gamma_{lv}\Delta l$, which arises from uncovering liquid of length $\Delta l/2$ on either end upon compression. This is justified since this energy does not affect the shape of the blister, as we shall see shortly. Furthermore, we will only look at the energy difference between wrinkled and blistered states, which

is independent of $\gamma_{lv}\Delta l$, since the sheet undergoes the same 'uncovering' of liquid in the wrinkling regime.

In dimensionless terms, we write the surface energy penalty as

$$\mathcal{U}_s^{(b)} = \Gamma(B + L_b) \tag{3.12}$$

where $\gamma_{lv} \equiv \Delta\gamma\ell_w^2/\mathcal{B}$ is the dimensionless strength of adhesion for a wetted blister. Note that $\Gamma = (\ell_w/\ell_{ec})^2$, so that Γ measures the wrinkle wavelength compared to the elasto-capillary length.

Minimizing the energy (3.11) as in the previous section, we find the non-dimensional equation of equilibrium for the blistered state:

$$\left(\frac{\theta_{SS} + \tau\sin\theta + S\delta\cos\theta}{\cos\theta}\right)_S = \begin{cases} 0, & 0 \le |S| \le L_b/2 \\ -\frac{1}{2W_S}\left(\frac{W^2}{\cos\theta}\right)_S, & L_b/2 \le |S| \le L/2, \end{cases} \tag{3.13}$$

where the equation for the wetted region $L_b/2 \le |S| \le L/2$ is identical to (3.7). Note that in the blistered region $0 \le |S| \le L_b/2$, equation (3.13) may be integrated once to give the equation for a 'ruck in a rug' derived previously (Vella *et al.*, 2009*b*; Kolinski *et al.*, 2009; Wang, 1986), namely

$$\theta_{SS} = -\tau\sin\theta + \delta(L_b/2 - S)\cos\theta. \tag{3.14}$$

Equation (3.13) is to be solved subject to the symmetry conditions

$$\theta(0) = 0, \quad X(0) = 0, \tag{3.15}$$

the clamped conditions at the edges of the sheet,

$$W(L/2) = \theta(L/2) = 0, \tag{3.16}$$

and an imposed displacement $X(L/2) = (L - \Delta L)/2$. An additional condition arises from the fact that the bottom surface of the sheet must touch the liquid surface at its natural level when $S = L_b/2$, i.e.

$$W(L_b^-/2) = W(L_b^+/2) = \delta. \tag{3.17}$$

Finally, we have continuity conditions at the edge of the blister

$$[\theta]_-^+ = [\theta_S]_-^+ = [\theta_{SS}]_-^+ = 0, \tag{3.18}$$

which guarantee continuity in slope, bending moment and shear force at the contact point, respectively. Note that a liquid substrate cannot exert a shear force and so cannot support the discontinuity in θ_S that we have with a solid substrate.

Equation (3.13), together with $x_s = \cos\theta$ and $w_s = \sin\theta$, describes a system of two third order ODEs, two first order ODEs and one unknown parameter, τ. The solution of this ninth order system is completely determined by the set of nine boundary conditions given in (3.15) – (3.18). The problem may again be solved numerically using, for example, `bvp4c`. However, a great deal of understanding can be obtained by considering the linearized theory, which is valid for small deformations $\theta \ll 1$, and letting $L \to \infty$.

3.3. Linearized framework

For small angles, we may take $S \simeq X$ and $L_b \simeq B$. In this limit, (3.13) reduces to

$$\frac{\mathrm{d}^4 W}{\mathrm{d}X^4} + \tau \frac{\mathrm{d}^2 W}{\mathrm{d}X^2} = \begin{cases} -W, & B/2 \le |X| \le L/2 \\ -\delta, & 0 \le |X| \le B/2. \end{cases} \tag{3.19}$$

The linearized system is subject to the symmetry and boundary conditions

$$W_X(0) = W_{XXX}(0) = 0, \quad W(B^-/2) = W(B^+/2) = \delta, \quad W(L/2) = W_X(L/2) = 0, \tag{3.20}$$

and the matching conditions at $X = B/2$

$$[W_X]^+_- = [W_{XX}]^+_- = [W_{XXX}]^+_- = 0. \tag{3.21}$$

Equation (3.19) describes a system of two fourth order ODEs with one unknown parameter, τ. The nine conditions given in (3.20) – (3.21) thus fully determine the state of the system. We consider the limit $L \to \infty$, which is reasonable since the energy of the blistered state is expected to be dominated by that in and around the blister. In this limit, δ can be rescaled out of the problem by letting $\omega = W/\delta$. We find the analytical solution

$$\frac{W}{\delta} = \begin{cases} e^{-\lambda\xi}\left\{\cos\mu\xi + \beta_2 \sin\mu\xi\right\}, & |X| > B/2 \\ \beta_1\left(\cos\tau^{1/2}X - \cos\dfrac{\tau^{1/2}B}{2}\right) + \left(\dfrac{B^2 - 4X^2}{8\tau} + 1\right), & 0 < |X| < B/2, \end{cases} \tag{3.22}$$

where $\xi = X - B/2$, $\lambda = (2-\tau)^{1/2}/2$, $\mu = (2+\tau)^{1/2}/2$, and the constants $\beta_{1,2}$ are given by

$$\beta_1 = \tau^{-3/2}\left[2\lambda\tau + B(\tau-1)/2\right]\csc\tfrac{B\tau^{1/2}}{2},$$
$$\beta_2 = -\frac{B}{2\mu} - \frac{\lambda}{\mu}$$

and the compressive force τ is found as a function of the blister size B from

$$1+\tau-\tau^2+\frac{B\tau}{2}\left(2-\tau\right)^{1/2}=\left[1-\tau-\frac{2\tau}{B}\left(2-\tau\right)^{1/2}\right]\frac{B\tau^{1/2}}{2}\cot\frac{B\tau^{1/2}}{2}. \tag{3.23}$$

In the limit of large blisters, $B \gg 1$, we recover $\tau \approx 4\alpha^2/B^2$, where $\alpha \approx 4.493$ is the smallest positive solution of $x = \tan x$. The limit $B \gg 1$ therefore reduces to the buckling of a heavy elastica, or 'ruck in a rug', because the external compression accommodated in the adhered region is small compared to that accommodated within the blister.

3.4. Wrinkle to blister transition

We anticipate that the blistered state should be observed when it is energetically favourable in comparison to the alternative, i.e. wrinkled, state. We must therefore determine the total energy of the blistered state. For convenience, we measure the dimensionless energy $\mathcal{U}$ relative to the dimensionless energy of an undeformed floating sheet. This requires the subtraction of the isostatic energy, $\delta^2 L$ from that given in (3.11) to give the combined elastic and gravitational energy $\mathcal{U}^{(b)}_{e+g}$. We must add to this energy the surface energy penalty associated with delamination, $\mathcal{U}^{(b)}_s = \Gamma(B + L_b)$,

Blistering is therefore energetically favourable compared to wrinkling with the same compression, ΔL, whenever

$$\mathcal{U}^{(b)}_{e+g} + \mathcal{U}^{(b)}_s < \mathcal{U}^{(w)}, \tag{3.24}$$

where the energy of the wrinkled state, $\mathcal{U}^{(w)}$, is given by (3.10) and we note that in the limit $L \to \infty$ this reduces to $\mathcal{U}^{(w)} = 2\Delta L$. For given values of δ and Γ the critical compression or, equivalently, critical blister size $B = B_c$ at which blistering occurs can be computed numerically. (For a given compression, ΔL, B can be determined from $B = 2X(L_b/2)$). However, it is instructive to consider the limit of small deformations, where the blister profile is given by (3.22) and $B \approx L_b$. In this regime we have $\mathcal{U}^{(b)}_s = 2\Gamma B$ and it is a simple matter to show that $\mathcal{U}^{(b)}_{e+g} = \delta^2 f(B)$ and that $\Delta L = \delta^2 g(B)$ for some functions f and g, that can be computed numerically. Crucially, however, the quadratic dependence of each of these terms on δ shows that the inequality requirement for blistering may be written

$$2\frac{\Gamma}{\delta^2}B + f(B) < 2g(B), \tag{3.25}$$

and hence we see that, for the linear theory at least, the critical blister size $B_c = B_c(\Gamma/\delta^2)$.

Figure 3.3 shows the behaviour of the left hand side of the inequality in (3.25) for Γ/δ^2 =1, 10, and 50, along with the behaviour of the right hand side of (3.25). This

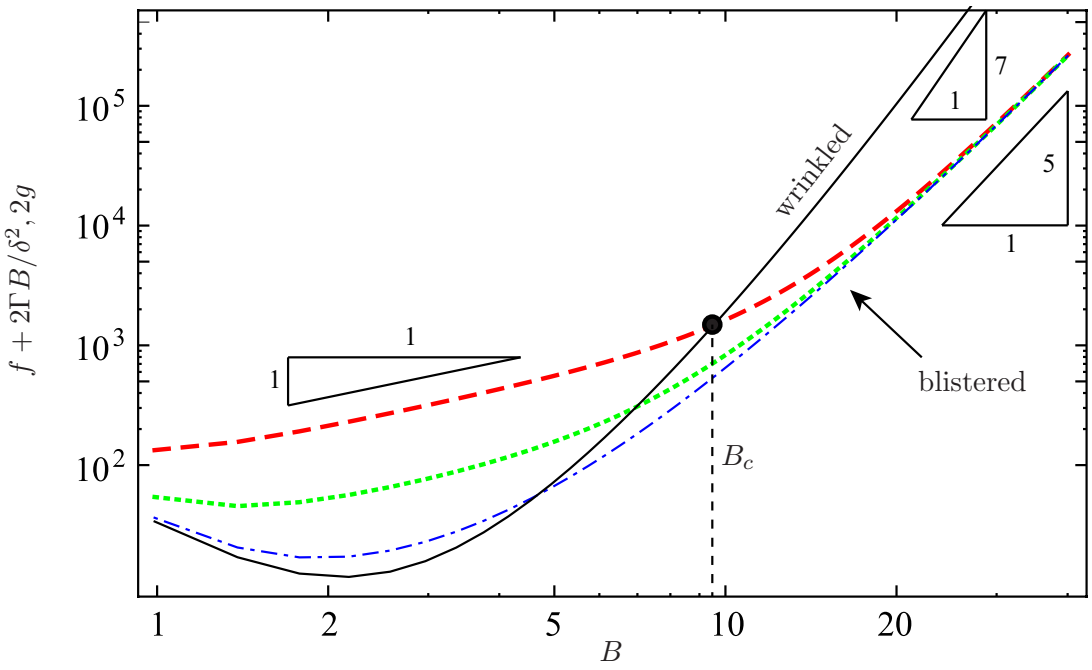

Figure 3.3.: The functions that appear in the energy inequality (3.25), which corresponds to the energy (normalised by δ^2), as a function of blister size B. The black solid curve shows the function $2g(B)$, which represents the energy of the uniformly wrinkled state. The coloured curves show $f(B) + 2\Gamma B/\delta^2$, the energy of blistered states, for $\Gamma/\delta^2 = 50$ (red dashed), 10 (green dotted) and $\Gamma/\delta^2 = 1$ (blue dash-dotted). The critical blister size, B_c is marked for $\Gamma/\delta^2 = 50$. The scaling behaviours of these functions in various limits are also illustrated (see text).

demonstrates that for sufficiently large B (corresponding to sufficiently large compressions ΔL) the formation of a delamination blister becomes energetically favourable compared to wrinkling. Altering the value of Γ/δ^2 essentially gives a shift in the blister energies, altering the observed blister size at onset accordingly.

Figure 3.4 shows the dependence of B_c on Γ/δ^2 obtained from both numerical solutions of the nonlinear problem and the linear theory. It also shows the asymptotic results, obtained from the linear theory (see following section). The numerical data points in the figure are obtained as follows. For a given value of Γ/δ^2, a set of blister shapes for varying values of compression ΔL (and thus blister sizes B) are found by solving (3.13), using the solver `bvp4c`. The values of ΔL are chosen such that B is close to the expected critical value B_c. The total energies of the states, $\mathcal{U}^{(b)}(B)$ are found from (3.11) and (3.12). The calculations are repeated for wrinkled states by solving (3.3) for the same set of compressions ΔL, giving the wrinkling energies $\mathcal{U}^{(w)}$. The critical blister size $B_c(\Gamma/\delta^2)$ is then obtained by extracting the point of cross-over, where $\mathcal{U}^{(b)}(B) \simeq \mathcal{U}^{(w)}(B)$.

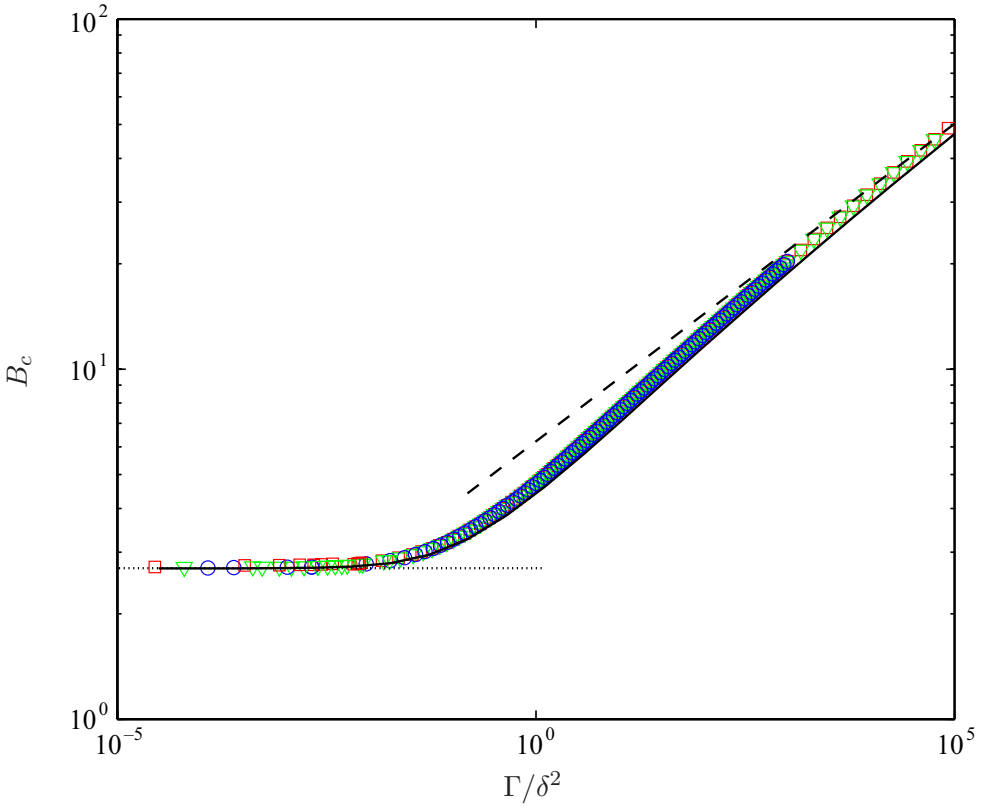

Figure 3.4.: Log-log plot of the critical blister size at onset B_c as a function of Γ/δ^2. Results from numerical solutions are shown as points: $\delta = 10^{-5}$ (○), $\delta = 10^{-4}$ (□) and $\delta = 10^{-3}$ (▽) – see text. The results of the linear theory (solid curve) lead to the asymptotic results (3.30).

3.5. Asymptotic results

It proves insightful to consider the limits $\Gamma/\delta^2 \gg 1$ and $\Gamma/\delta^2 \ll 1$. Writing

$$\Gamma/\delta^2 = \frac{\Delta\gamma}{\rho h^2 g(\rho/\rho_l)},$$

it becomes apparent that Γ/δ^2 can be interpreted as a measure of the strength of adhesion relative to the weight of the sheet, independent of the bending stiffness, $\mathcal{B}$. In the following we discuss in turn the limits of adhesion dominated scenarios ($\Gamma/\delta^2 \gg 1$) and gravity dominated ones ($\Gamma/\delta^2 \ll 1$).

3.5.1. $\Gamma/\delta^2 \gg 1$

As mentioned above, for $B \gg 1$ the ruck in a rug solution (Vella *et al.*, 2009*b*; Kolinski *et al.*, 2009) is recovered. The elasto-gravitational energy of the blistered sheet in the

linear limit is then given by

$$\mathcal{U}_{e+g}^{(b)} = \int_{-B/2}^{B/2} \left(\tfrac{1}{2} W_{XX}^2 + W\delta\right) \mathrm{d}X.$$

Note that in this limit, the energetic contribution of the wetted part (where $|X| > B/2$) can be neglected, since it is small compared to the energy stored in the blister. Using the solution (3.22), this integrates to

$$\begin{aligned}\mathcal{U}_{e+g}^{(b)} = \delta^2 \frac{1}{48\tau^2} \Big\{ & 4\left[B^3\tau + 96\lambda\tau + 6B(2\tau(2+\tau) - 3)\right] + \\ & 3\sqrt{\tau}\csc^2(B\sqrt{\tau}/2)\left[B(\tau-1) + 4\lambda\tau\right] \times \\ & \left[B\sqrt{\tau}(B(\tau-1) + 4\lambda\tau) + \sin(B\sqrt{\tau})(B(\tau-5) + 4\lambda\tau)\right] \Big\},\end{aligned}$$

where $\tau \to 4\alpha^2/B^2$. Performing a series expansion in B, we find to leading order

$$f(B) \sim \tfrac{1}{192\alpha^4}\left(4\alpha^2 + 15\alpha\cot\alpha + 3\alpha^2\csc^2\alpha - 18\right) B^5 \approx 0.0018057 B^5, \tag{3.26}$$

Similarly, an asymptotic expression for $g(B)$ can be obtained, giving rise to the asymptotic result

$$g(B) \sim \tfrac{1}{768\alpha^6}\left(2\alpha^2 + 9\alpha\cot\alpha + 3\alpha^2\csc^2\alpha - 12\right) B^7 \approx 0.00001597 B^7. \tag{3.27}$$

Substituting these expressions into (3.25) we find that $B \gg 1$ only if $\Gamma/\delta^2 \gg 1$. This provides a further explanation of why the ruck in a rug is approached in this limit: we require $\delta \to 0$ to have $\Gamma/\delta^2 \gg 1$, which is achieved when $\rho_l \to \infty$, i.e. when the substrate becomes rigid. The inequality (3.25) then reduces to $(\Gamma/\delta^2)B < g(B)$, in this limit. Rewriting this in terms of ΔL, we find that blistering is energetically preferable for

$$\Delta L > 6.302 \Gamma^{7/6} \delta^{-1/3}. \tag{3.28}$$

3.5.2. $\Gamma/\delta^2 \ll 1$

On the other hand, for $\Gamma/\delta^2 \ll 1$, equation (3.25) reduces to $f(B) < 2g(B)$ and it is clear that we require $B > B_c$ with $B_c = \mathcal{O}(1)$. The asymptotic considerations in this case are somewhat more cumbersome, since (a) the energy of the adhered parts, where $|X| > B/2$, cannot be ignored and (b) $\tau = \tau(B)$ has to be computed as a function of the blister width from (3.23). A numerical computation (using, for example, MATHEMATICA) reveals that this requires a critical compression

$$\Delta L_c \approx 6.597 \delta^2. \tag{3.29}$$

We point out that the critical compression (as well as the critical blister size (3.30)) is independent of Γ in this limit . Writing $\Gamma/\delta^2 = \Delta\gamma\rho_l/\rho^2 h^2 g \ll 1$, it is easily appreciated that in this limit the surface energy penalty due to delamination is small relative to the weight of the sheet; it is therefore unsurprising that in this limit adhesion does not affect the transition behaviour.

The compression thresholds (3.28) and (3.29) correspond to critical blister sizes

$$B_c \approx \begin{cases} 2.627, & \Gamma/\delta^2 \ll 1 \\ 6.302(\Gamma/\delta^2)^{1/6}, & \Gamma/\delta^2 \gg 1. \end{cases} \tag{3.30}$$

We note from figure 3.3 that these asymptotic limits are recovered by both the linear and nonlinear computations.

3.6. Experiments

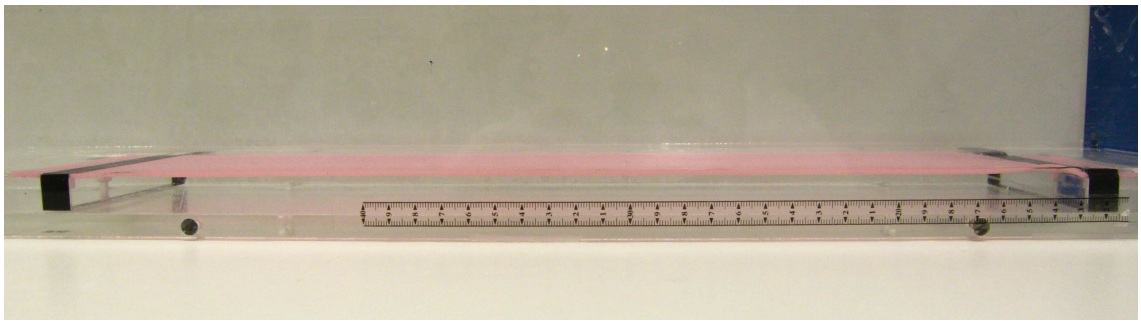

Figure 3.5.: The experimental setup showing a rubber sheet (pink) in its uncompressed state ($\Delta L = 0$), fixed to transparent perspex blocks at either end with black tape, resting in a perspex tank which is filled with water to the height of the blocks. The ruler shown is adhered to the tank wall for reference and has large divisions of 1 cm and small divisions of 1 mm.

The theoretical analysis presented in the last section was tested with a series of macroscopic experiments. Rubber sheets were fabricated from Vinylpolysiloxane (Zhermack), hardness Shore 8, with length 40 cm, width 10 cm and different thicknesses in the interval 0.6 mm $\lesssim h \lesssim$ 1.6 mm. Due to the fabrication process, there were small thickness variations within a given sheet. These variations had standard deviations between 0.04 and 0.1 mm and were incorporated in experimental error bars.

The bending rigidity $\mathcal{B}$ was measured by means of the elastic loop test (Stuart, 1966). Assuming $\nu \approx 0.5$ (as is typical of rubbers) the measured values of $\mathcal{B}$ correspond to $E = 220 \pm 10$ kPa, consistent with earlier measurements (Vella *et al.*, 2009*a*).

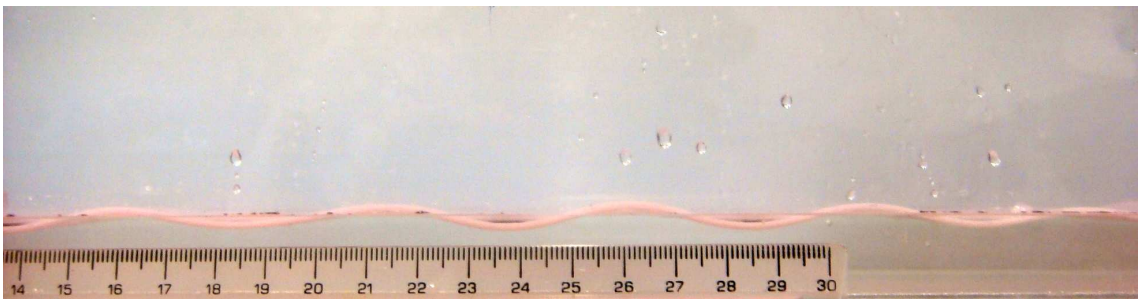

Figure 3.6.: Extended wrinkles, as commonly predicted in the literature (see, for example, Huang & Suo (2002); Vella *et al.* (2004)), observed for values of end-end compression $\Delta L \lesssim \Delta L(B_c)$. Sheet thickness in this case is $h = 0.65$ mm (appears thicker due to flashing at the edges).

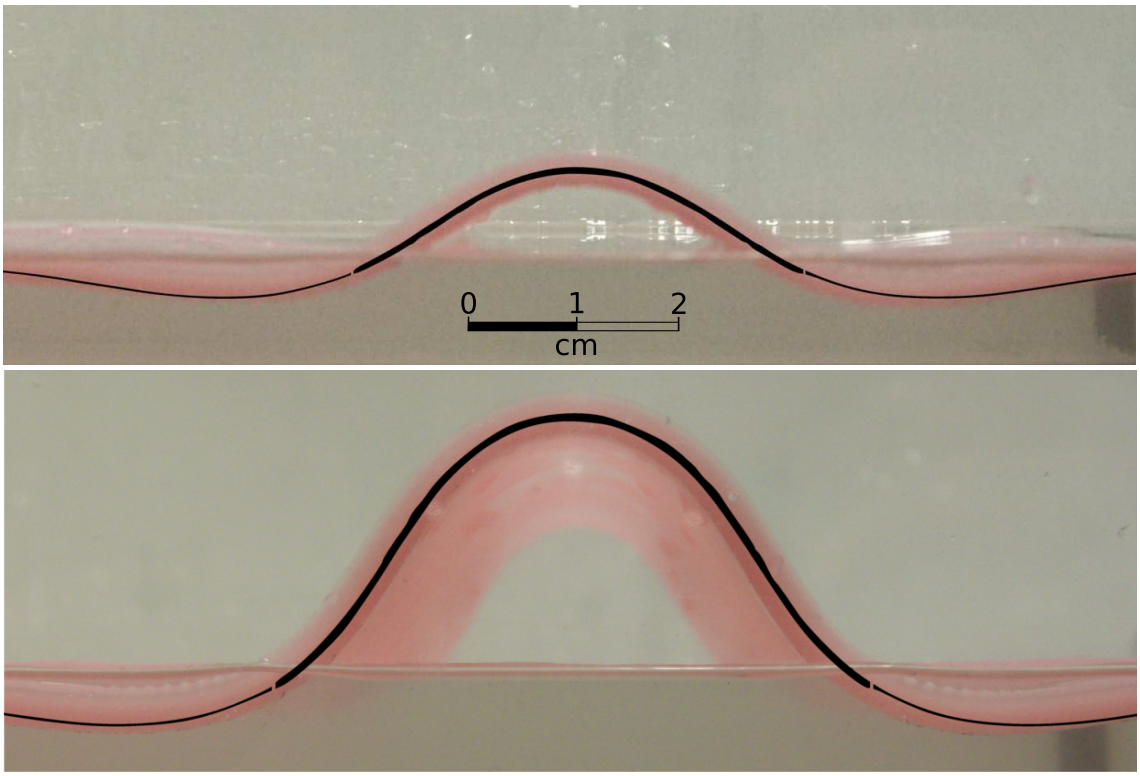

Figure 3.7.: Profile of blistered sheet ($h = 1.6$ mm) for end-to-end compressions $\Delta L = 0.6$ cm (top) and 2.0 cm (bottom). Photographs show the experimentally observed shapes while solid curves show the theoretically predicted shapes with the same values of ΔL. The theoretical shapes were calculated using the nonlinear heavy elastica equation (3.13) within the blistered region and the linear form (3.19) in the adhered region. These curves are plotted at a height $h/4$ above the base of the sheet (rather than over the apparent centreline) because flashing (an artefact of fabrication) at the edge of the sheet increases the apparent thickness of the sheet at the edge.

Experiments were performed with two different liquid substrates: water ($\rho_l = 1000$ kgm^{-3}) and a 49% solution of potassium carbonate (K_2CO_3, $\rho_l = 1520$ kgm^{-3}). The surface tension coefficient for pure water is well known to be $\gamma_{lv} = 72$ mNm^{-1} at room temperature,

while for 49% potassium carbonate solutions, tables give $\gamma_{lv} = 102$ mNm^{-1} (Armand, 2008). The experiments were performed in a perspex tank measuring 70 cm $\times$ 15 cm and filled to a depth of 3 cm with the appropriate liquid. To impose clamped boundary conditions the ends of the rubber sheets were taped to perspex blocks at a depth corresponding to $w \approx 0$. These blocks were then moved together quasi-statically, compressing the sheet using a laboratory jack. The experimental setup is shown in figure 3.5. The value of ΔL imposed was found by measuring the displacement of the sheet edge relative to its original position in photographs of the experiment. For small values of ΔL, wrinkles that extended over the whole length of sheet were observed – as shown in figure 3.6. As expected from the preceding calculations, a delamination blister forms spontaneously at a critical compression. Two typical blister shapes are shown in figure 3.7 and compared to those predicted theoretically. In all comparisons that follow, we use the nonlinear heavy elastica equation (Vella *et al.*, 2009*b*; Wang, 1986) to model the deformation of the blistered part of the sheet, though the adhered part is modelled using the linear theory (3.19) since it is found to be only slightly deformed. We observe good agreement between experiment and theory in these instances.

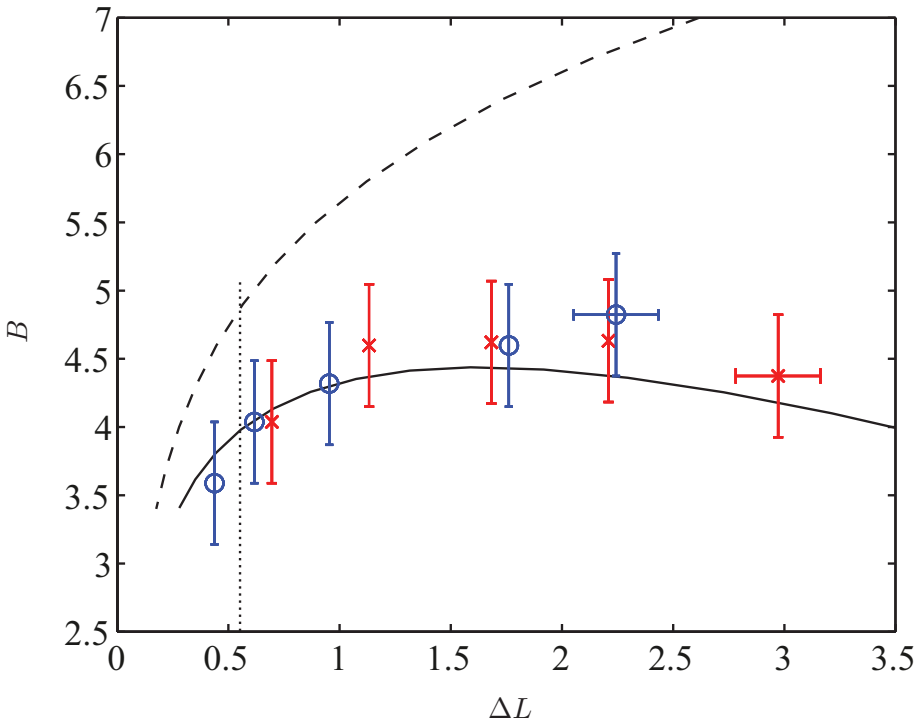

Figure 3.8.: The (dimensionless) evolution of B with varying compression ΔL. Experimental results are shown for compression (×) and relaxation (◯) with the results of the nonlinear theory (solid curve) and the linear result $B \approx 4.844\Delta L^{1/7}$(Vella *et al.*, 2009*b*) (dashed curve). The vertical dotted line represents the predicted onset of blistering, ΔL_c.

An experimentally accessible quantity is the size of the delamination blister B as a function of the end-to-end compression ΔL. A comparison between measured values of B and those predicted by numerical simulations is plotted in figure 3.8. This is the floating sheet equivalent to figure 2.6a. This figure demonstrates good agreement between theory and experiment. We note that in this situation experiments in both compression and relaxation are repeatable and reproduce the same critical compression for the appearance/ disappearance of the blister – there is very little observable hysteresis in our problem, unlike that observed in related problems (Vella *et al.*, 2009*a*). Furthermore, the nonlinear heavy elastica equation is able to explain a feature of the experiment that is not predicted by the simple linear theory: we observe that both experiments and nonlinear theory show a non-monotonic relationship between the blister size B and the compression so that the blister becomes narrower as the sheet is compressed more, just as observed in the case of the Sticky Elastica.

Another accessible parameter is the critical blister size at onset, b_c, as the sheet properties vary. Figure 3.9 shows experimentally measured values of b_c for different sheet thicknesses in comparison with that predicted from numerical simulations and again demonstrates good agreement.

The errorbars in figures 3.8 and 3.9 arise mainly from three factors: the aforementioned variations in sheet thickness, the liquid meniscus at the tank wall (making an accurate measurement of the natural liquid surface level difficult) and the liquid meniscus at the sheet-liquid contact line inside the blister. The first gives errors in h of order ± 0.1 mm and the latter two combine to cause errors in b of order ± 0.5 cm. The horizontal errorbars in figure 3.8 are only representative and illustrate setup inaccuracies (error in clamping conditions, non-uniformity in the plane of the liquid surface, ± 0.2 cm) as well as an error in the value of Δl_c due to the dynamic nature of the experiment: it is only possible to measure the critical value of ΔL_c to within ± 0.15 cm.

3.7. Conclusions

We have introduced a new type of deformation for uniaxially compressed floating sheets: over a region of well-defined size the sheet de-adheres from the liquid, forming a delamination blister. This new instability was studied under the assumption that the vertical deformations remain small and we showed that this 'blistering' is a discontinuous process that occurs at a well-defined compression ΔL_c and is manifested by the appearance of a blister with a well-defined size B_c. This transition occurs when the energy required to accommodate a given displacement by wrinkling exceeds that required to accommodate the same displacement by blistering. We have shown that, within the linear theory, the blister

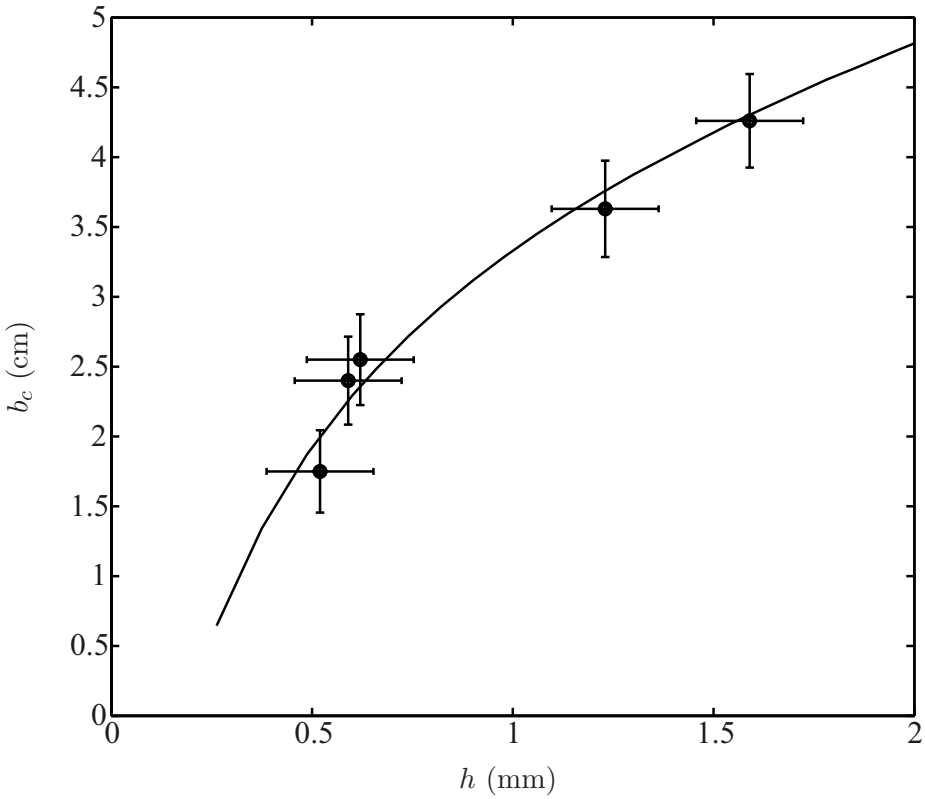

Figure 3.9.: Blister size at onset, b_c, for different sheet thicknesses, h, measured experimentally (points) and compared to the prediction from numerical computations (solid curve).

size at onset, B_c, is a function of the rescaled surface energy Γ/δ^2 only and characterised this dependence with scaling laws in the limits $\Gamma/\delta^2 \ll 1$ and $\Gamma/\delta^2 \gg 1$. In dimensional terms these scaling laws show that

$$b_c \sim \begin{cases} \left(Eh^3/\rho_l g\right)^{1/4}, & \gamma_{lv} \ll \rho^2 g h^2/\rho_l \\ \left(\gamma_{lv}^2 E^3 h^5/\rho_l \rho^4 g^5\right)^{1/12}, & \gamma_{lv} \gg \rho^2 g h^2/\rho_l. \end{cases} \tag{3.31}$$

That the blister size observed at onset increases with the surface energy γ_{lv} is both surprising and in contrast to what has been found for the case of a sheet delaminating from a soft elastic substrate (Vella *et al.*, 2009*a*). However, this behaviour is simple to understand qualitatively: for stronger adhesion a greater compression needs to be applied to cause delamination (as is also the case for a sheet delaminating from a soft substrate (Vella *et al.*, 2009*a*)). In the case of a floating sheet this causes a larger blister to be formed. Nevertheless, we note that the observed dependence is relatively weak, $b_c \sim \gamma_{lv}^{1/6}$.

The theory developed in this chapter is a first step towards understanding delamination more generally. The restoring force that is provided by hydrostatic pressure is relatively

simple to model and is analogous to the response of thin elastic substrates, or Winkler foundations. Hence the delamination of thin films from a thin elastic layer of thickness h_l and with Lamé constants λ and μ should be described by the theory presented here with $\rho_l g$ replaced by a stiffness $(\lambda + 2\mu)/h_l$ (Skotheim & Mahadevan, 2004). For thick substrates more detailed analysis is required but may yield new insights beyond those obtained from fully numerical approaches such as the finite element method (Parry *et al.*, 2005; Yu & Hutchinson, 2002).

Many features of these systems remain to be understood, such as the dynamic onset of blisters, which are observed to propagate from the edge of the sheet towards the centre (violating our assumption that the behaviour in the plane is uniform). It also remains to understand fully the regimes in which the different scenarios of wrinkling, blistering and folding are found. Here we obtained analytical results in the limit of infinite system size, $L \to \infty$, in which case blistering is ultimately energetically more favourable than wrinkling. However, with a finite system size the energy of the wrinkled state includes a non-linear term that acts to decrease the elastic energy and hence may suppress the blistering instability. This is likely to be particularly pertinent in the limit of large surface tension, $\Gamma/\delta^2 \gg 1$. For example, using the relevant values for thin polyester films floating on water (Pocivavsek *et al.*, 2008) we find that $\Gamma/\delta^2 \approx 4\times10^4$ and $\ell_w = 2.5$ mm. According to (3.30) blisters will only occur in these systems if the compression $\Delta l > 10$ cm, which is significantly larger than the compressions required to observe folding in these systems (Pocivavsek *et al.*, 2008; Diamant & Witten, 2010). However, in less confined systems subject to large stresses — e.g. floating sea ice sheets — the delamination presented here might naturally be observed. Indeed, Arctic explorer Julius Payer offers a tantalizing allusion to this, writing in his diary: '... immeasurable pressure causes [the ice floes] to bend like arcs, yes, in *blisters* they rise, a terrifying sign of the elasticity of the ice ...' (von Payer, 1876).

Chapter 4

The Deposition of a Sheet onto an Adhesive, Corrugated Substrate

Synopsis

We present a theoretical study of the deposition of an elastic sheet onto a grooved substrate incorporating adhesion between substrate and sheet. We develop a model to understand the equilibrium of the sheet allowing for partial conformation of sheet to substrate. This model gives physical insight into recent observations of 'snap-through' from flat to conforming states of Few Layer Graphene sheets and emphasises the crucial role of substrate shape in determining the nature of this transition. Our analytical results are consistent with numerical simulations using a van der Waals-like interaction. Finally we propose a substrate shape that should exhibit a continuous, rather than 'snap-through', transition.

4.1. Introduction

4.1.1. The role of substrate geometry in adhesion problems

The proceeding chapters have illustrated how the interplay between material properties and sheet geometry determine the delamination behaviour of a system. On a practical level, knowledge of the shape of the delaminated sheet can provide information about material parameters, such as Young's modulus or the strength of the sheet-substrate adhesion, and vice versa. In the case of the Sticky Elastica, for example, the width and height of the delamination blisters alone give an accurate estimate of the system's elastocapillary length. Even carelessly deposited sheets featuring essentially random blister landscapes, can in this way provide insight into the properties of the system (Aoyanagi *et al.*, 2010).

However, in many cases, a careful control over the exact morphology of a system is desired. From an experimental point of view, such control becomes increasingly difficult as scales become smaller. This is, in particular, a problem for delamination experiments, since for thin enough sheets the strength of the sheet may be insufficient to allow for the usual blister tests – the sheet may tear rather than delaminate (Sen *et al.*, 2010). This means that a sheet, once brought into contact with the substrate, is often irreversibly stuck, leaving little room for experimental adjustments. If the sheet does not exhibit the desired deformations, the experimentalist usually has no choice but to start afresh.

One way around these issues, commonly used in *blister tests* (Jensen, 1991; 1998), is to deposit the thin unstressed sheet onto a perforated substrate. Blisters are then created in a controlled way either by varying the pressure of the system (Wan & Lim, 1998; Koenig *et al.*, 2011) or by applying a shaft load through the perforation of the substrate (Wan, 1999).

In the present chapter we model a different experimental approach that also avoids the difficulty of controlling the geometry of the sheet. Instead of envisaging a perforated base, the surface topography of the substrate is altered. In the case considered here, the sheet is brought into contact with a regularly corrugated substrate. Depending on the substrate geometry and the material characteristics of the system, the sheet will adopt a well-defined, partially (or fully) adhered state. This scenario resembles an 'inverted' delamination blister and again we can infer material properties from the shape of the sheet (and vice versa). The advantage of this approach is that the geometry of the substrate is in many cases easier to design and manipulate than the geometry of the sheet.

The theoretical model presented here is motivated by recent experiments on the deposition of thin graphene flakes. One of the main mechanical difficulties in using graphene

is that its free (non-adhered) state is highly unstable (Meyer *et al.*, 2007) and prone to crumpling (see figure 1.1), restacking (Horiuchi *et al.*, 2004) and scrolling (Shioyama, 2001; Viculis *et al.*, 2003). This is why in experimental studies the graphene is commonly deposited on a substrate first.

4.1.2. Graphene 'snap-through'

Recently, considerable research effort has focussed on characterizing the mechanical properties of Few Layer Graphene (FLG) sheets — from their elasticity and strength (Poot & van der Zant, 2008; Lee *et al.*, 2008) to their ultrastrong adhesion to substrates (Koenig *et al.*, 2011; Kusminskiy *et al.*, 2011). Understanding these properties is important for a number of potential applications since they influence the form taken by sheets, which in turn can influence its electrical characteristics (Kim & Castro Neto, 2008). While standard adhesive tests have been applied with some success to measure adhesion, it has also been proposed that deposition onto a corrugated substrate may provide a simpler assay for such measurements (Zhang & Li, 2011). For a given substrate geometry and material properties, we expect that a sheet deposited onto a substrate will adopt one of three configurations (illustrated schematically in figure 4.1). For relatively weak adhesion, we expect a nonconformal (Aitken & Huang, 2010; Gao & Huang, 2011) configuration, in which the sheet sits above the substrate with very little deflection. For very strong adhesion, we expect the sheet to be significantly deflected and to adopt essentially the form of the substrate – the conformal scenario shown in figure 4.1 (right).

Previously, it has been assumed that the transition from nonconformal to conformal morphologies is sudden, leading to this transition being referred to as 'snap-through'. Indeed, such a 'snap-through' transition has recently been observed in FLG sheets, as illustrated in figure 4.2 (Scharfenberg *et al.*, 2012). However, in principle a third, intermediate, config-

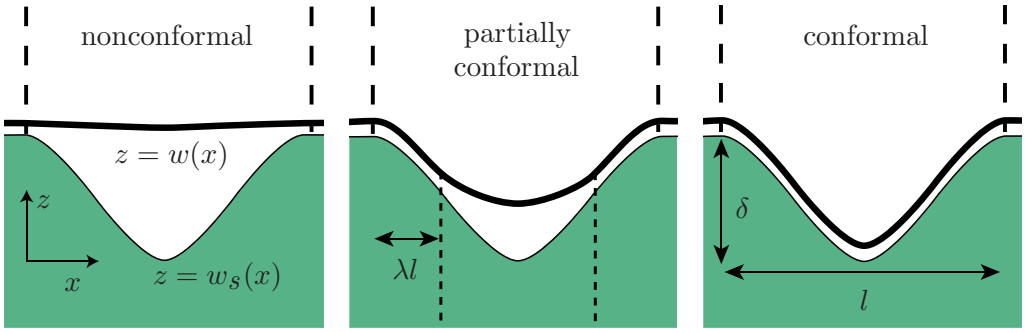

Figure 4.1.: Schematic representation of the three possibilities for FLG morphology on a corrugated substrate. *Left:* no adhesion and the FLG sheet remains approximately flat, *Centre:* partial adhesion in which the FLG sheet is out of contact with the substrate in the region $\lambda l < X < (1-\lambda)l$, *Right:* complete adhesion with the FLG sheet , completely conforming to the substrate topography.

uration exists, which we term 'partially conformal' (see figure 4.1, centre), with the sheet conforming to the substrate over a finite portion of its length but not everywhere. In this chapter, we study the transition from nonconformal to conformal morphologies theoretically. The question of principal interest is whether this transition is sudden (i.e. occurs at a critical adhesive strength) or, rather, whether there is a range of adhesive strengths for which a partially conformal morphology may be observed. For simplicity we consider a single groove in the substrate rather than a fully corrugated substrate.

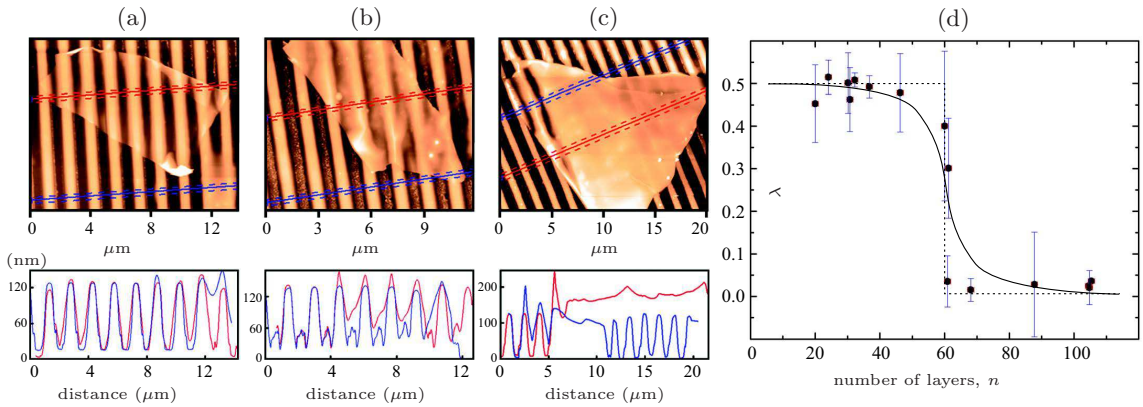

Figure 4.2.: Experimental results for FLG sheets deposited onto a corrugated substrate, reproduced from Scharfenberg *et al.* (2012). Subfigures (a)-(c) show AFM height data (top images) and line scans (bottom) for: (a) a fully conformal 46-layer graphene flake, (b) a partially conformal flake with number of layers, $n = 60$ and (c) a nonconformal state ($n = 88$). (d) illustrates the transition from conformal ($\lambda = 0.5$) to nonconformal states ($\lambda = 0$) as n is increased. The dotted curve corresponds to a 'snap-through', the solid curve to a smooth transition (curves added by author). The experimental data appears to be inconclusive.

A letter based on the work described in this chapter has been published in *Applied Physics Letters* (Wagner & Vella, 2012). The work was performed under the supervision of Dominic Vella.

4.2. Theoretical analysis

4.2.1. Governing equations

We model the FLG sheet as an elastic beam with bending stiffness $\mathcal{B}$ and thickness h. The position of the beam's centreline is given by $z = w(x)$. To allow for analytical progress we consider a substrate with a single two-dimensional groove of width l and depth δ; the shape of the groove is given by $z = w_s(x)$, (note that, in this chapter, the subscript s indicates 'substrate', rather than d/ds). Throughout this chapter we assume that the typical slope of the substrate is small, i.e. $\delta/l \ll 1$. This restricts the model to the linear

regime of classical beam theory, where $\mathrm{d}w/\mathrm{d}x \ll 1$. To determine whether the sheet is conformal for a given set of parameters, we must determine the shape of the sheet $w(x)$ and compare this with $w_s(x)$. In regions where the sheet is conformal with the substrate we have, by definition, that $w(x) = w_s(x)$. In regions where the sheet is not conformal with the substrate its shape satisfies the beam equation (Landau & Lifschitz, 1970)

$$\mathcal{B}\frac{\mathrm{d}^4 w}{\mathrm{d}x^4} = 0, \tag{4.1}$$

where, for simplicity, we neglect the possibility of a tension within the membrane. The neglect of the tension within the FLG sheet amounts to neglecting a frictional interaction with the substrate; the inclusion of such a friction would complicate the analysis and require the *ad hoc* assumption that the sheet be on the point of sliding everywhere. To further avoid any edge effects we do not impose a length constraint, but assume that the sheet extends to infinity in both x-directions. We assume that the groove is symmetric about $x = l/2$ and denote the position of the contact points between sheet and substrate by $x = \lambda l$ and $x = (1-\lambda)l$. The shape of the FLG sheet is thus

$$w(x) = \begin{cases} a_0 + a_2(l/2 - x)^2, & |l/2 - x| < |1/2 - \lambda| l \\ w_s(x), & |l/2 - x| > |1/2 - \lambda| l, \end{cases} \tag{4.2}$$

where the constants a_0, a_2 and the value of λ are determined by boundary conditions that we will discuss shortly.

We envisage that the deflection of the free portion of the sheet is caused by the adhesive interaction energy per unit area, $\Delta\gamma$, between the substrate and sheet. In particular, we expect that the value of λ (which determines the contact points) will be determined to minimize the energy of the system. This energy, U, comprises of the bending energy of the sheet (caused by its curvature, which resists the sheet conforming to the substrate) and the energy released by the sheet coming into contact with the substrate over a portion of its length, which drives the sheet to conform to the substrate. We have that the energy of the system is

$$U = \int_0^{\lambda l} \mathcal{B}\left[w_s''(x)\right]^2 \mathrm{d}x + \int_{\lambda l}^{l/2} \mathcal{B}\left[w''(x)\right]^2 \mathrm{d}x - 2\lambda l \Delta\gamma, \tag{4.3}$$

where we take the nonconformal state to be the ground state of energy. As discussed in section 1.3.3, we make use of the calculus of variations to find the solution $w(x)$ that minimizes the energy (4.3). $w(x)$ is then found by solving the beam equation (4.1) subject to the boundary condition, (1.19), which here reads

$$|w''(\lambda l) - w_s''(\lambda l)| = \sqrt{2\Delta\gamma/B} = \sqrt{2}/\ell_{ec}. \tag{4.4}$$

The continuity of the sheet's displacement and slope at the contact point ($[w]^+_- = [w']^+_- = 0$) require that the constants a_0 and a_2 in (4.2) be

$$\begin{aligned} a_0 &= w_s(\lambda l) - a_2 l^2 (1/2 - \lambda)^2, \\ a_2 &= -w_s'(\lambda l)/l(1 - 2\lambda), \end{aligned}$$

which may be substituted into (4.4) to give a single equation for λ for a given substrate shape, namely

$$-w_s''(\lambda l) - \frac{2w_s'(\lambda l)}{l(1-2\lambda)} = \sqrt{2}/\ell_{ec}. \tag{4.5}$$

4.2.2. Strength of adhesion and the role of substrate geometry

In what follows, it will be useful to rescale vertical dimensions by the depth of the substrate groove, δ and horizontal dimensions by the groove width, l, i.e. $W = w/\delta,\ X = x/l$, etc.. This non-dimensionalization introduces, via (4.4), the dimensionless strength of adhesion

$$\Gamma = (l^4/\delta^2)\Delta\gamma/\mathcal{B} = (R/\ell_{ec})^2, \tag{4.6}$$

where $R = l^2/\delta$ is the typical radius of curvature of the substrate. In physical terms the parameter Γ tells us whether the adhesive energy is strong enough to overcome the bending energy penalty resisting the sheet conforming to the substrate. It remains to be seen, however, whether, for a given substrate shape $W_s(X)$ the transition between nonconformal ($\lambda = 0$, small Γ) and conformal ($\lambda = 1/2$, large Γ) is smooth or, rather, a discontinuous 'snap-through' transition. We couch our study in terms of varying the dimensionless adhesion strength Γ. Experimentally, Γ may be varied by fixing the bending stiffness $\mathcal{B}$ and varying $\Delta\gamma$ or by holding $\Delta\gamma$ constant and varying $\mathcal{B}$. In the case of FLG sheets the latter approach has been achieved experimentally by varying the number of molecular layers (Scharfenberg *et al.*, 2012).

Non-dimensionalizing (4.5), we have

$$(2\Gamma)^{1/2} = -W_s''(\lambda) - \frac{2W_s'(\lambda)}{(1-2\lambda)} \equiv \mathcal{G}(\lambda). \tag{4.7}$$

For a given substrate shape $W_s(X)$ and dimensionless adhesion strength Γ we therefore have a single equation for λ. Here we shall consider in detail three substrate shapes, chosen to illustrate some of the different behaviours that can be observed. These are

$$W_s = \begin{cases} W_s^{(1)} = \frac{1}{2}\left(1 + \cos 2\pi X\right), \\ W_s^{(2)} = 1 - \sin^4 \pi X, \\ W_s^{(3)} = 1 - \left(1 - |1 - 2X|\right)^3, \end{cases} \tag{4.8}$$

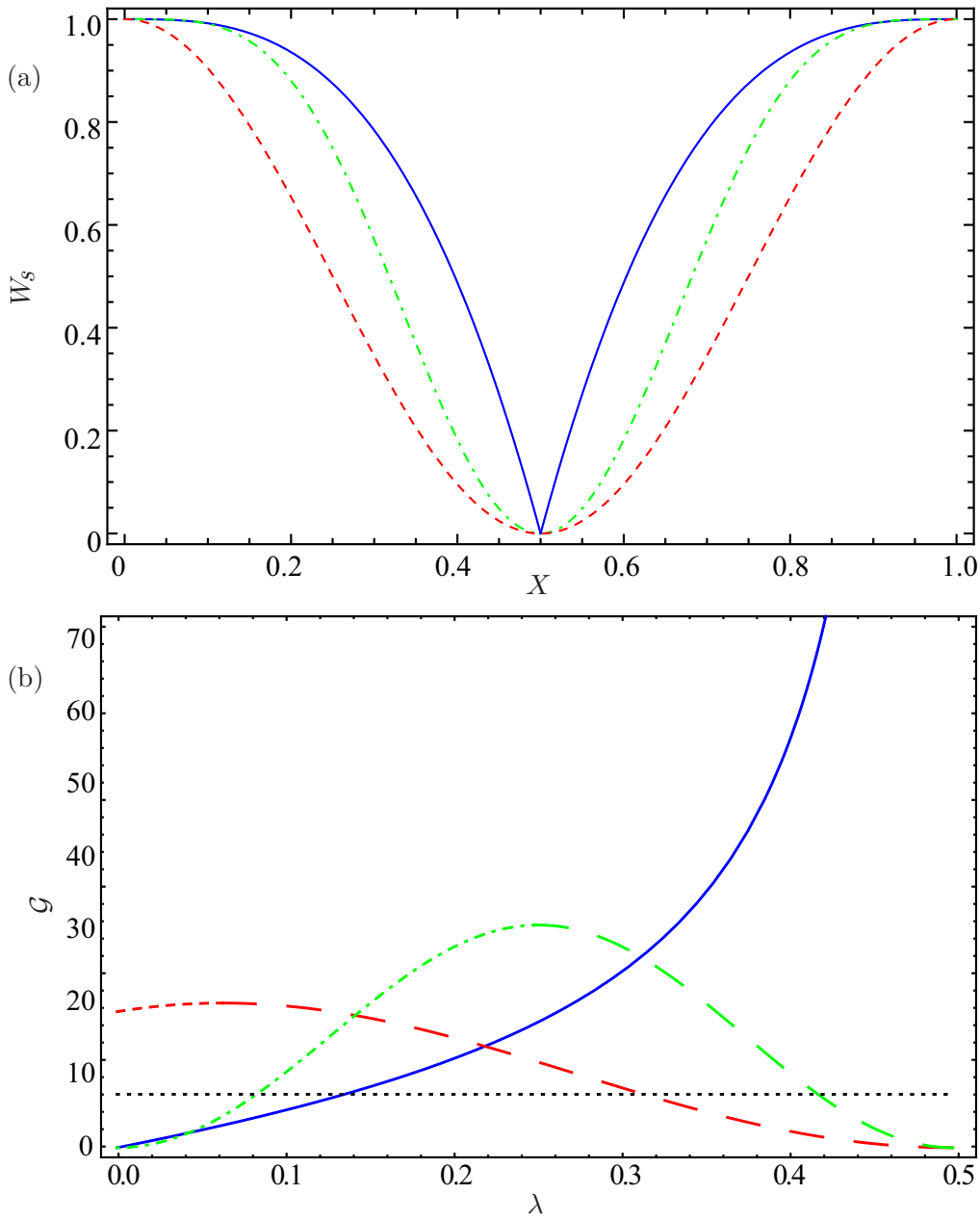

Figure 4.3.: (a) The three different substrate shapes considered here: $W_s^{(1)}$ (red dashed), $W_s^{(2)}$ (green dash-dotted) and $W_s^{(3)}$ (blue solid). (b) The function $\mathcal{G}(\lambda)$ defined in (4.7) for the different substrate shapes in (a). The intersection of these curves with the horizontal black dotted line, $(2\Gamma)^{1/2}$, illustrates the values of λ satisfying (4.7); these points correspond to maxima (long-dashed portions of the curves) and minima (red dashed, green dash-dotted and blue solid curves) of the energy $\mathcal{U}$ (see text).

for $0 \leq X \leq 1$ (outside this interval $W_s = 1$ in each case). For each of these substrate shapes it is a simple matter to plot the behaviour of the RHS of (4.7) as a function of λ (see figure 4.3b). We see that for a given value of Γ there are typically $0, 1$ or 2 values of λ that satisfy (4.7). The different behaviours shown in figure 4.3b influence the nature of the transition from nonconformal to conformal morphologies, as we shall see shortly.

The roots of equation (4.7) correspond to the extrema of the energy. However, as well as a minimum of energy (corresponding to the contact point we would expect to observe experimentally), there may also be other extrema, i.e. maxima and inflection points. Equation (4.7) does not contain information as to which of its solutions correspond to minima and which are rather maxima or inflection points. In principle, it is possible to obtain this information from the variational approach using the second variation (Gelfand & Fomin, 2000). However, it is also possible for global energy minima to occur with $\lambda = 0$ or $\lambda = 1/2$; since these are not extrema they do not appear as solutions of (4.7) and must be detected by considering the dimensionless energy $\mathcal{U} = U/(\mathcal{B}\delta^2/l^3)$, with U as in (4.3).

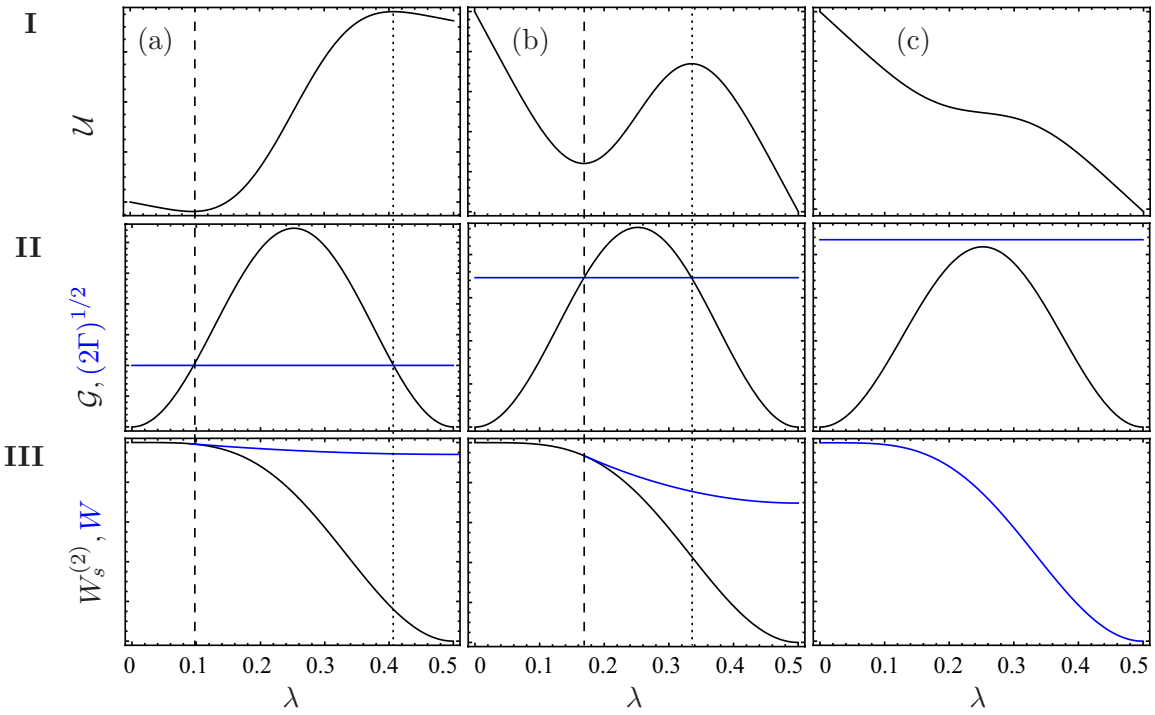

Figure 4.4.: Schematic graphs showing in rows: (I) the λ-dependence of energies $\mathcal{U}$, (II) the functions $\mathcal{G}, (2\Gamma)^{1/2}$ and (III) the substrate and sheet profiles for different values of Γ, all for the substrate $W_s^{(2)}$. Highlighted are states of energetic minimum (dashed lines) and energetic maximum (dotted lines). Columns correspond to (a) partial adherence for small strength of adhesion, Γ (b) partial adherence for larger value of Γ, (note the additional global minimum at $\lambda = 0.5$, discussed in the text) and (c) fully adhered state for $\Gamma > \Gamma_c$, no local minimum for $\lambda < 0.5$.

This is illustrated for the case of $W_s^{(2)}$ in figure 4.4. The energy plots (top row of

the figure) show that for this substrate, there exists an energetic minimum for partially adhered states (i.e. $\lambda \neq 0, 0.5$) for any strength of adhesion below a critical value, i.e. for $\Gamma < \Gamma_c$. These minima are given by the roots of equation (4.7) (figure 4.4, middle row). However, the energetic minimum does not necessarily represent a global minimum as is clear from figure 4.4, Ib. Here, the global minimum is found at $\lambda = 0.5$, i.e. for the fully adhered state. We further find that any local minimum is lost for $\lambda \neq 0, 0.5$ when $\Gamma > \Gamma_c$ (Ic) – leaving the fully adhered state as the only stable possibility.

We therefore find that, for given parameters, partial conformity (where $\lambda \neq 0, 0.5$) can be deduced from the roots of (4.7) that represent energetic minima, as illustrated in figures 4.3b and 4.4 II. If such roots do not exist, the sheet will be either fully flat or fully conformal, depending on which configuration minimizes the total energy, $\mathcal{U}$. These results will be discussed in further detail in section 4.4, at hand of the three different substrate shapes given in (4.8). We will see that the different shapes result in qualitatively distinct transition behaviour.

4.3. Van der Waals interaction between beam and corrugated substrate

The formulation above allows us to determine the transition behaviour for any substrate $w_s(x)$ by plotting figure 4.3b. However, an alternative approach, which has been adopted, for example, in Aitken & Huang (2010), Gao & Huang (2011), Bodetti *et al.* (2012), is to model the molecular forces of adhesion directly by means of a medium range attractive and short range repulsive van der Waals force. This approach provides its own insights and gives another viewpoint on the above results. As discussed in section 1.3.2, for a thin sheet, or beam, resting on a nonpolar substrate the interaction energy between a molecule within the sheet and another molecule within the substrate is given by

$$U_{m-m} = -C\left(\frac{1}{r^6} - \frac{D}{r^{12}}\right), \tag{4.9}$$

with r the distance between the two molecules and C and D material dependent parameters. To obtain the full interaction energy between the FLG sheet and the substrate, (4.9) is integrated over the semi-infinite substrate and the full thickness of the sheet, giving (1.8) in the limit of small slopes $\delta/l \ll 1$. For a sheet of thickness $H = h/\delta$ and with the distance between the mid-plane of the sheet and the surface of the substrate denoted by $Y(X) = W(X) - W_s(X)$ the beam equation (4.1) is modified to become, in dimensionless form,

$$\frac{\mathrm{d}^4 W}{\mathrm{d}X^4} + \alpha\left[\frac{1}{(Y - H/2)^3} - \frac{1}{(Y + H/2)^3} - \beta\left(\frac{1}{(Y - H/2)^9} - \frac{1}{(Y + H/2)^9}\right)\right] = 0, \tag{4.10}$$

(see Appendix 4.A for a derivation of this result).

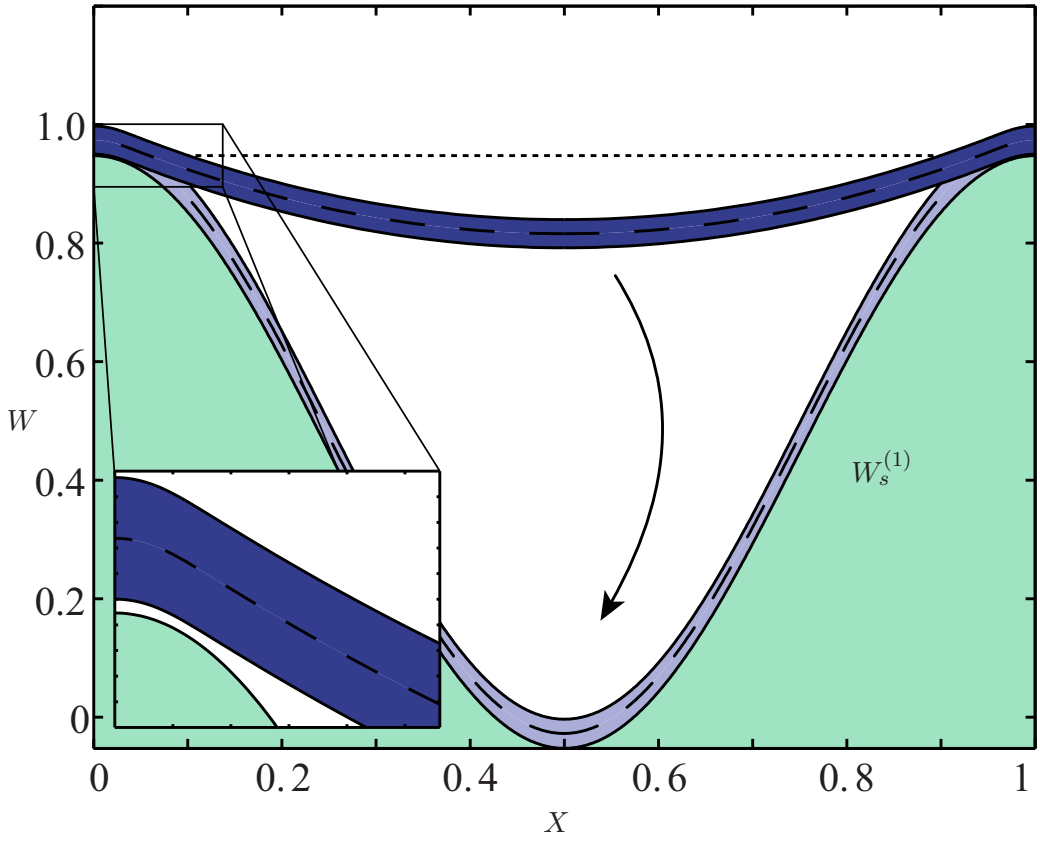

Figure 4.5.: Dimensionless substrate with geometry $W_s^{(1)}$ and sheet profiles, computed numerically from the modified beam equation (4.10). The parameters here are $H = 0.05$, $Y^* = 0.0025$. The dark blue profile shows the sheet for $\Gamma \simeq 90$, i.e. shortly before 'snap-through' (see text). The light blue profile gives the fully conformal state ($\Gamma > 97.4$). Inset: detailed view of the point of delamination close to $\lambda = 0$. Note the finite distance Y^* between the adhered sheet and the substrate – this allows for the small deflection before 'snap-through' in the numerical case. The analytic solution for the substrate $W_s^{(1)}$ allows for no such deflection (dotted line).

The dimensionless constant β is related to the equilibrium distance Y_0 between the centreline of an undeformed sheet and a flat substrate. The dimensionless van der Waals radius is then defined as $Y^* = Y_0 - H/2$, see (1.9). In experiments presented previously (Scharfenberg *et al.*, 2012), $h \gtrsim 6$ nm, $y^* \lesssim 3.3$ Å (Giovannetti *et al.*, 2008) and $\delta = 120$ nm so that $Y_0 \ll 1$, $Y^* \ll H \ll 1$. In the limit $H \gg Y^*$ we find that $\beta \simeq Y^{*6}$. Furthermore the constant α and the adhesive strength Γ are related by $\alpha \simeq -(8/3)Y^{*2}\Gamma$ in this limit. This is the dimensionless analogue of (1.10) for the present setup. Note that the limit $Y_0 \gg 1$ leads to a different simplification of the model, which is appropriate for substrates with small scale roughness (Aitken & Huang, 2010; Gao & Huang, 2011) rather than the relatively large grooves considered here.

The ordinary differential equation (4.10) can be solved using, for example, the MATLAB

boundary value problem solver `bvp4c`. We do so by taking advantage of the symmetry about $X = 1/2$, imposing the symmetry conditions $W'(1/2) = W'''(1/2) = 0$ and solving over the region $X = [-L, 1/2]$ with $L \gg 1$, to avoid any edge effects – as with the analytical model. At the far end, we impose the clamped boundary conditions $W(-L) = Y_0$, $W'(-L) = 0$. An example of a resulting profile for the substrate $W_s^{(1)}$ is shown in figure 4.5.

The results of these numerical simulations can be compared with those of the analytical model by examining the total energy $\mathcal{U}$. We shall see that the results of this analysis and the analytical approach in section 4.2 above are generally in good agreement in the limit $1 \gg H \gg Y^*$.

4.4. Three different ‘snap-throughs’

Having outlined our analytical and numerical approaches, we now consider the ‘snap-through’ characteristics of the three different substrates given in (4.8), using a combination of the analytical and numerical approaches outlined in sections 4.2 and 4.3. We shall see that each of these substrates illustrates a different type of transition; indeed, the transition from nonconformal to conformal may be smooth and not a ‘snap-through’ at all.

4.4.1. Fully discontinuous ‘snap-through’

The substrate topography $W_s^{(1)}$ in (4.8) is of practical interest since it closely represents that used experimentally (Scharfenberg *et al.*, 2012). Examining the corresponding curve for $\mathcal{G}(\lambda)$ in figure 4.3 we see that only for $2\pi^4 \approx 194.8 \leq \Gamma \lesssim 220.2$ do partially adhered states represent local energy minima. From the energy $\mathcal{U}$ for this substrate, we find that a global minimum exists with $\lambda = 1/2$ (i.e. conformal morphology) for $\Gamma > \pi^4 \approx 97.4$. This minimum arises when the release of surface energy in adhesion balances the bending energy of the fully conformal state. Since this threshold is significantly below that at which the small window of partially conformal states exists, we expect the transition to the conformal state to be discontinuous, i.e. a ‘snap-through’ occurs. This is confirmed by the numerical results using a van der Waals attraction (see figure 4.6). There is a slight qualitative difference between numerical and analytical results, however: in the numerical model the sheet deflects slightly before ‘snap-through’ occurs, as shown in figure 4.5; this is due to the finite contact distance between sheet and substrate, Y_0. These results further confirm the assumption made by Scharfenberg *et al.* (2012) that ‘snap-through’ will occur when the surface energy released by conforming is equal to the bending energy penalty required to conform, which amounts to determining when $\mathcal{U} = 0$. This analysis was consistent with the experimental results, reproduced in figure 4.2.

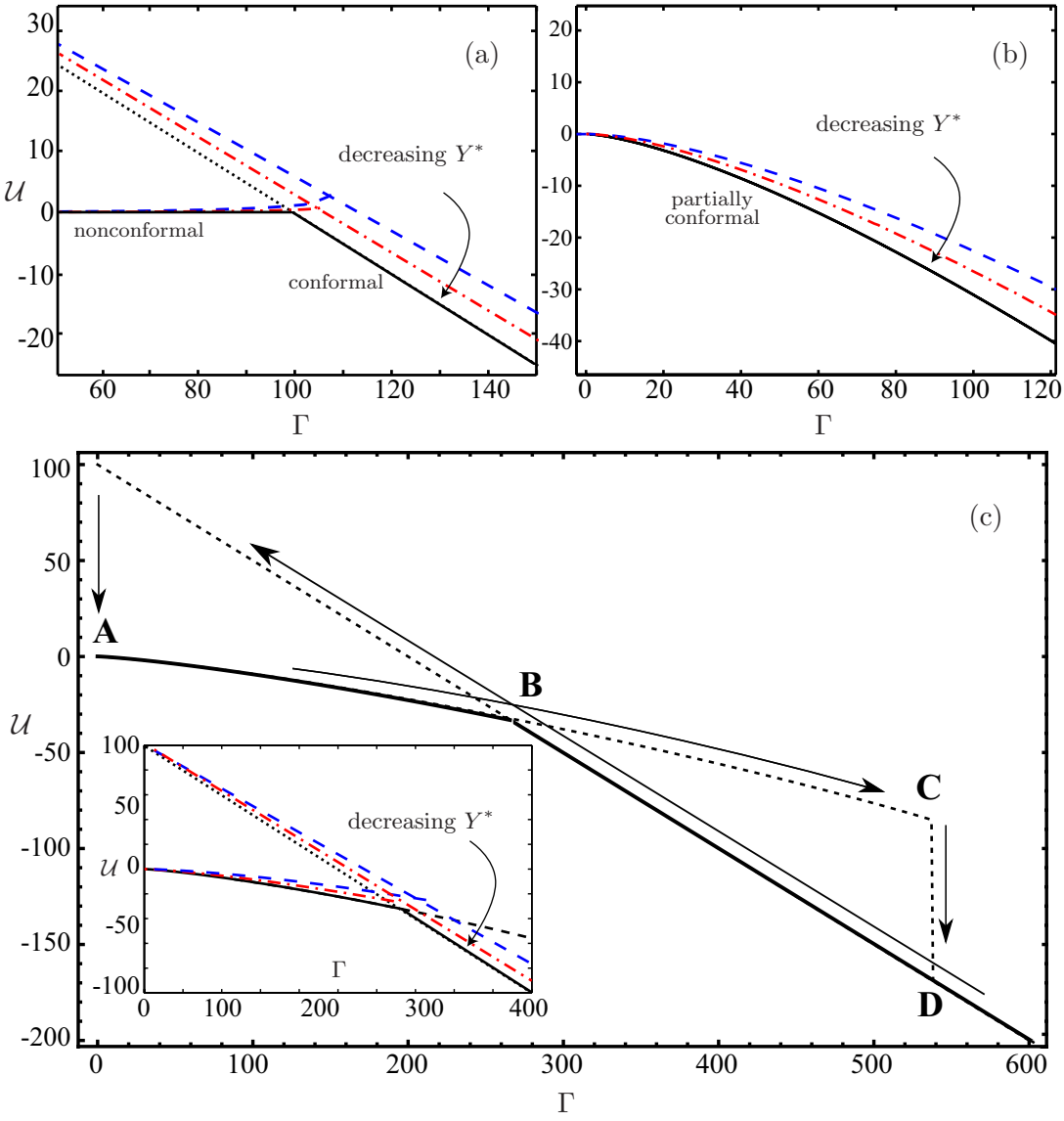

Figure 4.6.: Energy $\mathcal{U}$ of an FLG sheet above various grooved substrates as a function of adhesion strength Γ. Results show the predictions based on the analytic model for the global energy minimum (solid black curves) and local energy minimum (dotted curves) along with the numerical results for the van der Waals-like interaction governed by (4.10) with $Y^* = 10^{-3}$ (blue dashed curves) and $Y^* = 10^{-4}$ (red dash-dotted curves), both with $H = 0.05$. (a) For $W_s^{(1)}$, a 'snap-through' transition is observed analytically (see the discontinuity in slope of black curve at $\Gamma \approx 97.4$) and recovered in numerical simulations as $Y^* \to 0$. (b) For $W_s^{(3)}$, a smooth transition from nonconformal to conformal is observed with both approaches. (c) For $W_s^{(2)}$, partially conformal states are observed before 'snap-through' to the conformal state. Note the onset of a partially conformal morphology (**A**), earliest 'snap-through' (**B**) and final 'snap-through' (**C**), giving rise to a hysteresis loop (arrows). Inset: numerical results for $\mathcal{U}$ in this case.

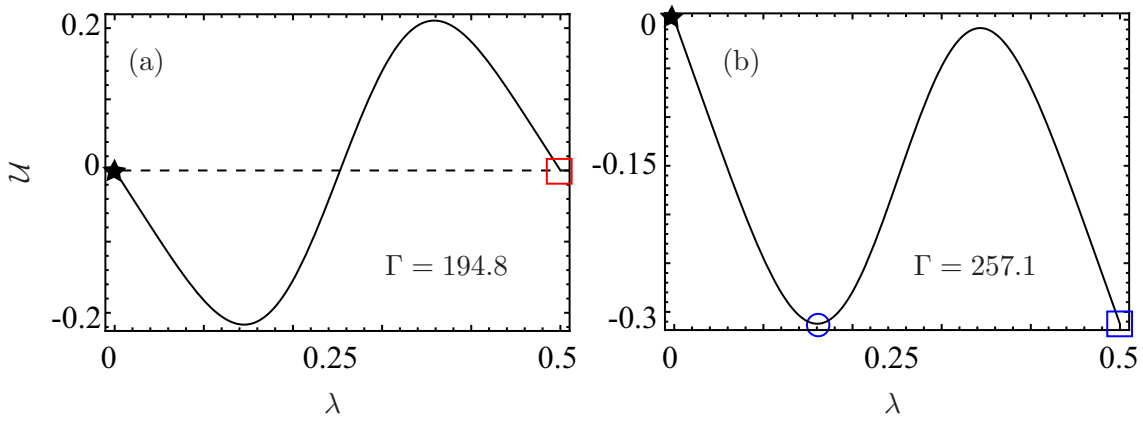

Figure 4.7.: Energy $\mathcal{U}$ as a function of λ, for the substrate $W_s^{(2)}$, for two critical values of Γ. (a) $\Gamma = 194.8$, the energy of the conformal state ($\lambda = 0.5$, □) is the same as that of the nonconformal state ($\lambda = 0$, ★). The global minimum is found for $\lambda \simeq 0.15$. (b) $\Gamma = 257.1$, the energy of the conformal state (□) is equal to that of the partially conformal state (◯), with $\lambda \simeq 0.16$. This value of Γ corresponds to point **B** in figure 4.6c.

4.4.2. Partially conformal states before 'snap-through'

The substrate topography $W_s^{(2)}$ is qualitatively similar to $W_s^{(1)}$, albeit with flatter peaks. However, this modification has a significant influence on the behaviour of $\mathcal{G}(\lambda)$ (see figure 4.3b). We see that in this case a partially conformal state exists as the local energy minimum, provided that $\Gamma \leq 529.3$. A calculation of $\mathcal{U}$ shows that this local minimum is the global minimum for $\Gamma \leq 257.1$, while for $\Gamma \geq 257.1$ it is the conformal state that is the global energy minimum (figure 4.7). We thus expect that for $\Gamma \leq 257.1$ the sheet will adopt a partially conformal morphology but that for $257.1 \leq \Gamma \leq 529.3$ the sheet may adopt *either* the partially conformal or the fully conformal states. Which of these states is realized in practice depends on the details of the experimental setup, including dynamic considerations. This uncertainty is illustrated by a hysteresis loop in figure 4.6c, which is also observed in the numerical simulations because of the use of a continuation scheme. Finally, we note that Scharfenberg *et al.* (2012) assumed that the point of 'snap-through' can be found simply by determining the adhesion energy required to give $\mathcal{U} = 0$. It emerges that this underestimates the value of Γ at 'snap-through' by around 20% in this case, since $\Gamma(\mathcal{U} = 0) = 2\pi^4 = 194.8$. This discrepancy arises because, for this substrate geometry, partially conformal states may have lower energy than the fully conformal state, depending on the value of Γ, as shown in figure 4.7.

4.4.3. A smooth transition

The substrate morphology $W_s^{(3)}$ is qualitatively different to those of $W_s^{(1)}$ and $W_s^{(2)}$ since it has a cusp at the midpoint, $X = 1/2$. The behaviour of the quantity $\mathcal{G}(\lambda)$ is also

qualitatively different to that observed for other substrates. In particular, we see from figure 4.3b that as λ increases towards $\lambda = 1/2$, $\mathcal{G}(\lambda)$ diverges. This divergence means that for all values of Γ there is a unique solution of (4.7); in other words, the transition from nonconformal to conformal morphologies progresses smoothly through partially conformal states; no 'snap-through' occurs. Physically, this happens because the curvature of the substrate diverges at the cusp and so no finite adhesion energy can overcome the bending energy penalty required to adopt a fully conformal morphology.

4.5. Conclusion

In summary, we have presented a theoretical formulation for the adhesion of FLG sheets onto grooved substrates. This formulation provides a simple explanation for why in the experiments presented to date a discontinuous 'snap-through' occurs: the curvature of the peaks of the substrate is so great that the bending energy penalty that has to be paid to conform partially to the substrate is too large. As a result the sheet can only conform fully and even then only once the adhesion energy is large enough. Our formulation highlights the crucial role played by the groove geometry in determining the nature of the transition. We have presented a substrate shape that is qualitatively very similar to the sinusoidal shape used in experiments, but for which we observe very different adhesion behaviour: the sheet now conforms partially to the substrate before snapping-through discontinuously.

We also presented a substrate shape where the discontinuous nature of the 'snap-through' transition disappears entirely to be replaced by a smooth transition from nonconformal to conformal morphologies. Furthermore, we have illustrated that in some cases the adhesion strength at which 'snap-through' occurs cannot in general be determined by setting $\mathcal{U} = 0$ since partially conformed states may be energetically favourable. These findings are supported by numerical simulations of a more traditional van der Waals-type model, which converges rapidly to the analytic result in the limit $Y^* \ll H \ll 1$.

From a practical perspective, it is important to mention the case of a sheet covering multiple substrate grooves, as is the case in the experiments shown in figure 4.2. We expect that qualitative differences between single and multiple grooves would arise mainly due to friction effects. However, since the van der Waals force in our model acts only vertically, there is no horizontal stresses in the sheet and no friction effects appear in the numerics (which is in line with the assumptions of the analytical model). As a result, we observe that the profiles of a sheet extending over a single substrate groove are very similar to those extending over multiple grooves.

Finally, we have proposed a substrate shape, $W_s^{(3)}$, for which the discontinuous 'snap-through' transition is replaced by a smooth family of partially conformal morphologies.

This development may allow for the determination of the strength of adhesion from a single experiment, since the position of the contact points encodes information about the strength of adhesion — it is not necessary to perform a whole series of experiments with different thickness FLG sheets to determine the critical thickness (Scharfenberg *et al.*, 2012). While the shape $W_s^{(3)}$ may seem difficult to fabricate, we note that a qualitatively similar shape is frequently seen at grain boundaries (Style & Worster, 2005; Bouville *et al.*, 2007). The continuous adhesion transition of this groove shape may also be of interest for other experiments on thin layer materials; for example, the high curvature seen near the cusp may give rise to plastic deformations making this a simple system within which to study the plasticity of FLG sheets.

Appendix

4.A. Derivation of the van der Waals-beam equation

In this Appendix, we derive the equation of equilibrium of a thin sheet, or beam, deposited on a non-flat substrate, by considering the attractive van der Waals interaction and the elastic bending response of the beam.

For a beam, resting on a nonpolar substrate the interaction energy between a sheet molecule and a substrate molecule is given by (Israelachvili, 1992):

$$U_{m-m} = -C\left(\frac{1}{r^6} - \frac{D}{r^{12}}\right), \tag{4.11}$$

with r the distance between the two molecules and C and D material dependent parameters. The molecule within the beam has coordinates $(x_b,\ y_b,\ z_b)$ whilst the molecule within the substrate has coordinates $(x_s,\ y_s,\ z_s)$ and the distance between the molecules is $r = \sqrt{\Delta x^2 + \Delta y^2 + \Delta y^2}$, where $\Delta x = x_s - x_b$, etc.. The energy of a beam molecule from the interaction with a volume element $\mathrm{d}x_s\mathrm{d}y_s\mathrm{d}z_s$ of the substrate is

$$\mathrm{d}^3U_m = \mathrm{d}x_s\mathrm{d}y_s\mathrm{d}z_s(-C\rho_s)\left(\frac{1}{\left(\Delta x^2 + \Delta y^2 + \Delta z^2\right)^3} - \frac{D}{\left(\Delta x^2 + \Delta y^2 + \Delta z^2\right)^6}\right),$$

where ρ_s is the density of the substrate.

To obtain the full interaction energy between the beam molecule and the substrate, this must be integrated over the semi-infinite substrate. We first perform the integration $\int_{-\infty}^{\infty}\mathrm{d}y_s$, which gives (Aitken & Huang, 2010)

$$\mathrm{d}^2U_m = \mathrm{d}x_s\mathrm{d}z_s(-C\rho_s\pi)\left(\frac{3}{8}\frac{1}{\left(\Delta x^2 + \Delta z^2\right)^{5/2}} - \frac{63}{256}\frac{D}{\left(\Delta x^2 + \Delta z^2\right)^{11/2}}\right). \tag{4.12}$$

The substrate is defined to occupy the region $-\infty < z_s < w_s(x_s)$. Integrating over the depth of the substrate and introducing $\xi(x_s) = z_b - w_s(x_s)$, the vertical distance between

the beam molecule and the surface of the substrate, we find

$$\mathrm{d}U_m = \mathrm{d}x_s(-C\rho_s\pi) \times$$
$$\left\{ \begin{array}{l} \frac{3}{8}\left(\frac{2}{3}\frac{\sqrt{\Delta x^2+\xi^2}-\xi}{\Delta x^4\sqrt{\Delta x^2+\xi^2}} - \frac{\xi}{3\Delta x^2(\Delta x^2+\xi^2)^{3/2}}\right) - \\ \\ \frac{63D}{256}\left(\frac{1}{315\Delta x^{10}(\Delta x^2+\xi^2)^{9/2}}\right) \left[\begin{array}{l} 128\xi^8\left(\sqrt{\Delta x^2+\xi^2}-\xi\right) \\ +64\Delta x^2\xi^6\left(8\sqrt{\Delta x^2+\xi^2}-9\xi\right) \\ +48\Delta x^4\xi^4\left(16\sqrt{\Delta x^2+\xi^2}-21\xi\right) \\ +8\Delta x^6\xi^2\left(64\sqrt{\Delta x^2+\xi^2}-105\xi\right) \\ +\Delta x^8\left(128\sqrt{\Delta x^2+\xi^2}-315\xi\right) \end{array} \right] \end{array} \right\}. \tag{4.13}$$

Finally, we must integrate (4.13) for all values of x_s to find an expression for the total energy of the molecule U_m. To facilitate this we assume that the typical slope of the substrate surface is small, (i.e. $\delta/l \ll 1$, as in the main text) and write

$$w_s(x_s) \simeq w_s(x_b) + w_s'(x_b)(x_s - x_b), \tag{4.14}$$

with $w_s'(x_b) \ll 1$. We therefore have that

$$\xi(x_s) \simeq \xi(x_b) + w_s'(x_b)(x_s - x_b). \tag{4.15}$$

Substituting (4.15) into (4.13) and integrating finally gives the full interaction energy between a beam molecule and the entire substrate as

$$U_m = -C\rho_s\pi\left(\frac{1}{6\xi(x_b)^3} - \frac{D}{45\xi(x_b)^9}\right), \tag{4.16}$$

correct to $\mathcal{O}\left([w_s']^2\right)$. To obtain the interaction energy (per unit area) of a beam of thickness h, whose centreline is at a height $z = w(x)$, we integrate over the thickness of the beam, writing

$$\begin{aligned} U(x_b) &= -\pi C\rho\rho_s \int_{w(x_b)-h/2}^{w(x_b)+h/2} \left[\frac{1}{6(z_b - w_s(x_b))^3} - \frac{D}{45(z_b - w_s(x_b))^9}\right] \mathrm{d}z_b \\ &= -\frac{\pi}{12}C\rho\rho_s \left[\left(\frac{1}{(w(x_b) - w_s(x_b) - h/2)^2} - \frac{1}{(w(x_b) - w_s(x_b) + h/2)^2}\right) - \right. \\ &\quad \left. \frac{D}{30}\left(\frac{1}{(w(x_b) - w_s(x_b) - h/2)^8} - \frac{1}{(w(x_b) - w_s(x_b) + h/2)^8}\right)\right]. \end{aligned} \tag{4.17}$$

To determine the effective beam equation governing the shape of a beam subject to this interaction energy, we add the interaction energy in (4.17) to the bending energy of the

beam. Applying the Euler–Lagrange equation to the resulting energy functional, we find that the appropriate beam equation is

$$0 = \mathcal{B}\frac{\mathrm{d}^4 w}{\mathrm{d}x^4} + \frac{\pi}{6} C\rho\rho_s \left[\frac{1}{(y(x) - h/2)^3} - \frac{1}{(y(x) + h/2)^3} - \right. \tag{4.18}$$

$$\left. \frac{2D}{15} \left(\frac{1}{(y(x) - h/2)^9} - \frac{1}{(y(x) + h/2)^9} \right) \right], \tag{4.19}$$

where $y(x) = w(x) - w_s(x)$ is the distance between the centreline of the sheet and the surface of the substrate. Performing the same non-dimensionalization as above and defining the non-dimensional constants $\alpha = (\pi/6) l^4 C\rho\rho_s / \mathcal{B}\delta^4$ and $\beta = 2D/15\delta^6$ gives the final answer:

$$0 = \frac{\mathrm{d}^4 W}{\mathrm{d}X^4} + \alpha \left[\frac{1}{(Y - H/2)^3} - \frac{1}{(Y + H/2)^3} - \beta \left(\frac{1}{(Y - H/2)^9} - \frac{1}{(Y + H/2)^9} \right) \right]. \tag{4.20}$$

Chapter 5

Irreversible Stiction in Nanoelectromechanical Switches

Synopsis

We present a theoretical investigation of stiction in nanoscale electromechanical contact switches. We develop a mathematical model to describe the deflection of a cantilever beam in response to both electrostatic and van der Waals forces. Particular focus is given to the question of whether adhesive van der Waals forces cause the cantilever to remain in the 'ON' state even when the electrostatic forces are removed. In contrast to previous studies, our theory accounts for deflections with large slopes (i.e. geometrically nonlinear). We solve the resulting equations numerically to study how a cantilever beam adheres to a rigid electrode: transitions between free, 'pinned' and 'clamped' states are shown to be discontinuous and to exhibit significant hysteresis. Our findings are compared to previous results from linearized models and the implications for nanoelectromechanical cantilever switch design are discussed.

5.1. Introduction

As the size of electronic systems is scaled down further and further, nanoelectromechanical (NEM) devices are increasingly seen as the 'promised land' of truly nanoscale technology. The development of NEM contact switches is often taken to be the natural next step from conventional semiconductor systems and has received much attention in recent research – see Loh & Espinosa (2012) for an overview of this area.

The concept of (macroscopic) electromechanical contact switches dates back to the early days of the telephone. It is, perhaps, the simplest example of how electrical and mechanical forces interact: an externally applied voltage induces mechanical bending of an electrode and closes the circuit. Once the voltage is removed, the elasticity of the electrode causes the switch to open again. However, as the size of the system is reduced to micro and nano scales, a third force (in addition to the electrostatic and elastic forces) becomes significant: the short range van der Waals (vdW) attraction between the electrodes. If this attraction is sufficiently strong then, once driven into contact by electrostatic forces, the switch may become 'stuck' in the ON position and may not reopen – even when the voltage is removed. This phenomenon, known as *stiction failure*, is one of two main engineering difficulties in modern NEM switch design (the other being 'ablation', in which the tip of the electrode is damaged by repeated contact cycles).

In this study we present a model of the operation of a NEM switch that incorporates three aspects of the stiction problem that previously have been considered in isolation: (a) the pull-in/pull-out behaviour of contact switches, for coupled vdW-Coulomb interactions; (b) the different adhered states possible and the transition between these states; (c) the effect of geometric nonlinearities for systems that feature large deflections. We first review briefly the previous work on each of these aspects. A schematic overview of the studies discussed in the following paragraphs is presented in figure 5.2.

The ON/OFF cycle of a cantilever switch is characterized by the transition from the freely suspended state to a contact state (pull-in) and the transition from a contact state back to the free state (pull-out). The pull-in behaviour of microelectromechanical (MEM) switches was first studied by considering a beam responding to electrostatic forces alone (Osterberg & Senturia, 1997; Chan *et al.*, 1999). As the interest in NEM devices increased, these models were superseded by models of a beam subjected to a combination of vdW and Coulomb forces (Dequesnes *et al.*, 2002). This made it possible to obtain an analytical estimate of the pull-in voltage for carbon-nanotube (CNT) based NEM switches. Later, these models also accounted for capillary and non-classical effects such as combined vdW-Casimir interactions (Palasantzas, 2006; Rotkin, 2009). Much of the recent experimental and numerical work has been based on this vdW-Coulomb model (Kinaret *et al.*, 2003;

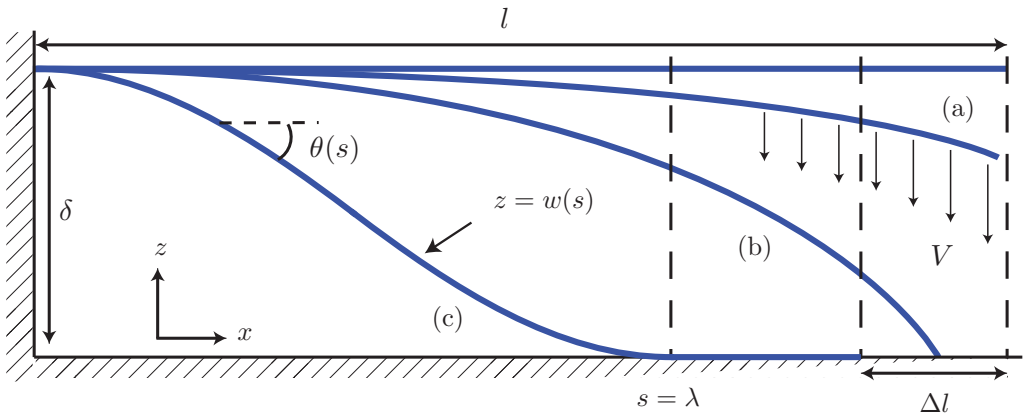

Figure 5.1.: Cantilever beam of length l, suspended at height δ and subjected to voltage V. The diagram highlights the three possible states of the beam: (a) freely suspended; (b) pinned at its free end; (c) adhered to the bottom electrode over a finite distance (detaching at $s = \lambda$). The free end of the beam is displaced by a horizontal distance Δl. The shape of the beam is characterised by intrinsic angle $\theta(s)$.

Dadgour *et al.*, 2008). However, the stiction conditions derived from this usually assume that the pull-out voltage is identical to the pull-in voltage (Dadgour *et al.*, 2008) and hence preclude the possibility of hysteresis due to adhesion. More recently, hysteretic adhesion was investigated by looking at a beam with a dimple at its free end (Chakraborty *et al.*, 2011). This gives rise to adhesion over a finite length (the length of the dimple) as soon as the beam makes contact with the substrate. Such a state is known as a 'clamped' state – (c) in figure 5.1. In the absence of a dimple, however, stiction can still occur even when the contact length tends to zero. The beam is then 'pinned' to the substrate at the end – state (b) in figure 5.1.

The two different modes of stiction for cantilever beams – 'pinned' and 'clamped' – were investigated in the context of stiction failure in MEM switches (Mastrangelo & Hsu, 1992; 1993; Mastrangelo, 1997). Stiction conditions for both pinned and clamped states have been presented, together with studies of the transition between them (De Boer & Michalske, 1999; de Boer *et al.*, 2000). These conditions give bounds for the design parameters of contact switches and can be used to estimate the strength of adhesion of an adhered beam (De Boer & Michalske, 1999; van Spengen *et al.*, 2002; Van Spengen *et al.*, 2003). Even though both clamped and pinned states are known to occur in NEM switches this earlier work is often ignored in later literature (Chan *et al.*, 1999; Loh *et al.*, 2011). More recently, adhesion transitions of multiple flexible sheets were investigated using a general approach (Evans & Lauga, 2009). This established a hysteresis loop between the different adhered (and non-adhered) states.

A common simplification in previous studies of cantilever switches is that the switch deformation has a small slope so that a linearised beam theory is appropriate. However,

examples in the literature suggest that many modern NEM contact switches feature large switch height/beam length aspect ratios (Loh *et al.*, 2011; Loh & Espinosa, 2012). In such cases, the assumption of small slopes is no longer appropriate – a nonlinear approach is called for. To our knowledge, large deflections have not been considered in previous studies of the stiction of contact switches (some studies, such as Ramezani *et al.* (2007) account for large deflections, but only up to pull-in). However, studies have considered nonlinear effects in systems that are related to the cantilever switch, including the peeling of a thin elastica from an adhesive substrate (Oyharcabal & Frisch, 2005), the folding of an elastica upon itself (Glassmaker & Hui, 2004) and the shape of large delamination blisters as discussed in chapter 2 (Wagner & Vella, 2013); these examples are reminiscient of a cantilever switch in its ON state.

	$\delta \ll l$			$\delta \sim l$	
	Pull in/ Pull out	Pinned Stiction	Clamped Stiction	Pull in/ Pull out	Stiction (Pin/ Clamp)
f_{vdw}		Mastrangelo & Hsu (1993) *doubly clamped beam, stretching* Mastrangelo (1997) *pinned/ free experiments, clamped analysis* de Boer et al (1999) *clamped states better to measure adhesion* de Boer & Michalske (1999) *transition between clamped and pinned* van Spengen et al (2002,2003) *surface roughness* Evans & Lauga (2009) *adhesion transition*	Loh & Espinoza (2011) *faulty adhesion*		Oyharcabal & Fritsch (2005) *peeling off an Elastica* Glassmaker & Hui (2004) *Elastica loops with self contact* Majidi (2007) *Elastica adhesion problems* Wagner & Vella (2013) *the 'Sticky Elastica'*
f_E	Osterberg (1997) *pull-in in MEM switch* Chan et al (1999) *find experimental hysteresis loop, no adhesion model* Chakraborty & Bhattacharyya (2010) *semi-analytical, to pull-in*	Gorthi et al (2006) *transition between states, stability analysis* Kinaret et al (2003), *precursor to Jonsson et al (2004)*	FQ Yang (2002) *considers clamped stiction*		
$f_{vdw}+f_E$	Dequesnes et al (2002) *original pull-in only* Rotkin (2009) *analytic pull-in* Dadgour & Cassell (2008) *up to pull-in + stiction (based on Dequesnes)* Shen et al (2011) *analytics up to pull-in* J Yang et al (2008) *nonlocal elasticity up to pull-in* Jonsson et al (2004) *surface forces, stiction, profile: simple cantilever beam* Chakraborty et al (2011) *incl casimir, pull-in & pull-out, beam with dimple*	present work	Zhang & Zhao (2004) *incl. stretching*	Ramezani et al (2008), *up to pull-in*	present work

Figure 5.2.: Overview of previous work on pull-in and stiction phenomena in contact switches. *Columns:* The studies have been grouped into linear ($\delta \ll l$) and nonlinear work ($\delta \sim l$) and further classified according to whether they look at pull-in/pull-out behaviour or at stiction processes. *Rows:* The listed publications are split into treatments that consider van der Waals forces only (f_{vdW}), electrostatic forces only (f_E) or a combination of the two ($f_{vdW} + f_E$).

In this chapter, we present a nonlinear model of a cantilever switch undergoing large elastic deflections due to a combination of vdW and Coulomb forces. We study how the suspended and adhered states change qualitatively with increasing and decreasing applied voltage and characterize the geometric and material conditions that result in permanent stiction.

The work presented in this chapter was performed under the guidance of Dominic Vella.

5.2. Theoretical formulation

5.2.1. Problem setup

We consider a naturally flat beam of length l and thickness h, acting as an electrode, suspended above a second, rigid electrode (the substrate). This setup is shown schematically in figure 5.1. The beam is clamped at height δ at one end and is free at the other. The system is subjected to an externally applied voltage, so that the beam experiences an electrostatic force that causes it to bend towards the bottom electrode. The voltage is increased until the beam makes contact with the substrate – at a critical pull-in voltage $V_{\text{p-i}}$. The switch is then said to be in its ON state, since it is now able to conduct. If the voltage is increased beyond $V_{\text{p-i}}$ the beam deflects further and becomes increasingly adhered (but still subject to free boundary conditions at its tip, whereas in the macroscopic picture it now evolves with pinned or clamped boundary conditions at the point of contact). It has been shown previously that a quasi-static approach is justified (Ramezani *et al.*, 2007), which allows us to ignore dynamic effects in what follows.

We assume that the material properties of the beam, namely its Young's modulus, E, and Poisson ratio, ν, are given, along with the strength of adhesion between beam and substrate, $\Delta\gamma$. The elastocapillary length may then be varied by changing the thickness of the beam (which changes the bending stiffness $\mathcal{B}$), but keeping $\Delta\gamma$ constant. The cantilever system thus features three geometric lengthscales that can be varied: the thickness of the beam, h, its length l and the clamping height, δ.

The deflection of the cantilever is determined by modelling the cantilever as an elastic beam. While we account for geometric nonlinearities, such a beam model is only valid when $h \ll l$ (Timoshenko & Goodier, 1970). With this restriction, there are only three possible separations of scale: $h \ll \delta \ll l$, $h \ll \delta \sim l$ and $h \sim \delta \ll l$. The first of these limits is that usually considered in theoretical studies of MEMS/NEMS contact switches. However, the latter two regimes are becoming increasingly relevant in many nano-scale applications (Loh *et al.*, 2011; Loh & Espinosa, 2012). Considering a geometrically nonlinear model

allows us to describe systems where $\delta \sim l$. To account for the case where $h \sim \delta$, it is also important to include the effect of finite beam thickness in the description of the vdW forces.

Our model considers both van der Waals and Coulomb forces. As discussed above, this combination has previously been considered in cantilever switch problems (Loh & Espinosa, 2012; Chakraborty *et al.*, 2011; Dequesnes *et al.*, 2002). However, the focus of these studies has been almost exclusively on estimating the pull-in voltage of a system, with little attention paid to the stiction process for voltages beyond pull-in. However, the volatility of stiction (whether stiction remains once the voltage is removed) is determined by the competition of bending moments in the deformed beam (which tend to restore the original flat state) and the attractive van der Waals (forcing the beam into an adhered state). It is therefore important to consider the effect of adhesion beyond pull-in.

5.2.2. Variational formulation

The bending energy per unit length of a beam is written as $U_B = \frac{1}{2}\mathcal{B}\theta_s^2$. We ignore stretching effects (considered, for example in Yin & Ya-pu (2004)), which amounts to neglecting friction – the validity of this assumption is discussed below.

In the previous chapter we derived the van der Waals interaction energy for a sheet (or beam, assuming uniformity across its width), whose mid-plane is at a height $z = w(s)$ above a non-polar substrate, for small angles, $\theta(s) \ll 1$. The effects of finite beam thickness and large deflections (where $\theta \sim 1$) are included by integrating the energy from $z = w - h/2\cos\theta$ to $z = w + h/2\cos\theta$, for a beam segment at an angle θ to the horizontal. The van der Waals energy per unit length may then be written as

$$U_{vdW} = -\frac{A_{\mathrm{H}}}{12\pi}\left[\left(\frac{1}{(w-h/2\cos\theta)^2} - \frac{1}{(w+h/2\cos\theta)^2}\right) - \frac{D}{30}\left(\frac{1}{(w-h/2\cos\theta)^8} - \frac{1}{(w+h/2\cos\theta)^8}\right)\right]. \tag{5.1}$$

The 'adhesion distance' is given by w_0 (discussed in section 1.3.2), with the van der Waals radius being $w^* = w_0 - h/2$, (1.9). Restricting ourselves to beams with thickness $h \gtrsim 3$ nm, we may again assume that $w^* \ll h$, (since $w^* \simeq 0.33$ nm, see chapter 4). This allows us to relate the strength of adhesion to the molecular constants via $\Delta\gamma = A_{\mathrm{H}}/16\pi w^{*2}$, as defined in (1.10) and write $D \simeq (15/2)w^{*6}$ (see section 1.3.2).

Defining $w_- \equiv w - h/2\cos\theta$ and $w_+ \equiv w + h/2\cos\theta$, we rewrite (5.1) as

$$U_{vdW} = -\frac{4}{3}\Delta\gamma\left\{\left(\frac{w^*}{w_-}\right)^2 - \left(\frac{w^*}{w_+}\right)^2 - \frac{1}{4}\left[\left(\frac{w^*}{w_-}\right)^8 - \left(\frac{w^*}{w_+}\right)^8\right]\right\}. \tag{5.2}$$

The Coulomb energy due to an externally applied voltage scales as $U_E \sim w(s)^{-1}$ (Israelachvili, 1992). This means that the electrostatic potential will be the driver of deflection wherever $w(s) \gg h$, but will be small compared to the vdW term when $w(s) \leq h$, i.e. when the beam is adhered. The fact that the U_E contribution is only significant when $w(s) \gg h$ suggests that we may neglect the finite thickness of the beam in the electrostatic term. The electrostatic energy (per unit length), defined as the work required to bring the beam from its original separation, where $z(s) = \delta$, to $z(s) = w(s)$, may be written

$$U_E(s) = -\tfrac{1}{2}\epsilon_0 V^2 \left(\frac{1}{w(s)} - \frac{1}{\delta}\right), \tag{5.3}$$

where ϵ_0 is the permittivity of free space. For simplicity, we ignore in this study the effects of fringing fields and do not consider dielectric layers which are commonly used in experimental setups (Osterberg & Senturia, 1997; Chowdhury *et al.*, 2005; Gorthi *et al.*, 2006; Yin & Ya-pu, 2004). However, our model could be modified to include these effects by adjusting the prefactor/adding a constant term in (5.3) accordingly (see, for example, Chowdhury *et al.* (2005); Gorthi *et al.* (2006)).

To obtain the total free energy of the suspended beam, the energies U_B, U_{vdW} and U_E are integrated over the total length of the beam. The equation of state of the system is then found by minimizing

$$U = \int_0^l \big[U_B(s) \ + \ U_{vdW}(s) + U_E(s) + F(s)(w_s - \sin\theta)\big]\mathrm{d}s, \tag{5.4}$$

where $F(s)$ is the Lagrange multiplier associated with the geometric relation

$$w(s) = \int_0^s \sin\theta(s')\ \mathrm{d}s'. \tag{5.5}$$

We shall see that $F(s)$ is related to the vertical component of the tension within the beam.

In what follows, it will be helpful to rescale all lengths by l, writing

$$d = \delta/l, \quad S = s/l, \quad H = h/l, \quad W = w/l, \quad \text{etc..} \tag{5.6}$$

We then obtain

$$\mathcal{U} = \int_0^1 \left\{ \tfrac{1}{2}\theta_S^2 - \frac{\alpha}{2}\left[\left(\frac{1}{W_-^2} - \frac{1}{W_+^2}\right) - \frac{\beta}{4}\left(\frac{1}{W_-^8} - \frac{1}{W_+^8}\right)\right] - \psi\left(\frac{1}{W} - \frac{1}{d}\right) + \eta(W_S - \sin\theta)\right\}\mathrm{d}S,$$

where, $\mathcal{U} = Ul/\mathcal{B}$ is the dimensionless Lagrangian functional and

$$\alpha \equiv A_{\mathrm{H}}/6\pi\mathcal{B}, \quad \beta \equiv 2D/15l^6, \quad \psi \equiv \epsilon_0 V^2 l/2\mathcal{B}, \quad \eta \equiv Fl^2/\mathcal{B}. \tag{5.7}$$

We define the dimensionless strength of adhesion $\Gamma \equiv l^2\Delta\gamma/\mathcal{B}$, such that $\alpha \simeq (8/3)W^{*2}\Gamma$ in the limit $W^* \ll H$, and $\beta \simeq W^{*6}$ as in the previous chapter. We simplify our notation by writing the sum of vdW and Coulomb energies as $\mathcal{G}(W,\theta) = \mathcal{U}_{vdW} + \mathcal{U}_E$.

Using the Calculus of Variations, we find that the functional $\mathcal{U}$ is extremized by functions satisfying (see section 1.3.1)

$$\begin{aligned} \theta_{SS} + \eta(S)\cos\theta + \mathcal{G}_\theta &= 0, \\ \eta_S - \mathcal{G}_W = 0, \quad W_S &= \sin\theta. \end{aligned} \tag{5.8}$$

Note that the vdW and Coulomb forces act purely vertically. This means that the beam experiences no horizontal stress, and explains why the Lagrange multiplier associated with the horizontal constraint in (1.1) is equal to zero and does not appear in (5.8).

Finally, our model neglects friction between the cantilever and the substrate. We neglect friction to simplify the treatment of contact regions. However, we note that experimental measurements of the friction coefficient of graphene layers yielded very low values (around 0.03, (Shin *et al.*, 2011)), so that frictional forces are always negligible in comparison to normal forces.

Equation (5.8) is a system of one second order ODE and two first order ODEs. Therefore, four boundary conditions are required to solve the system: these are given by

$$W(0) = d, \quad \theta(0) = 0, \quad \theta_S(1) = 0, \quad \eta(1) = 0. \tag{5.9}$$

The first two of these fix the beam to be clamped at a height d, at $S = 0$. The third and fourth impose free end boundary conditions at $S = 1$. Note that, since adhesion is modelled by an attractive potential, these free end conditions apply to all states of the switch – whether they are adhered or not. (In contrast, theoretical treatments without explicit vdW forces instead impose adhesion conditions at the stuck end of the beam, which modifies the boundary conditions (5.9) – such models are discussed below and are similar to those used for the Sticky Elastica.)

To compute the horizontal deflection of the free end, ΔL, for given input parameters d, H, ψ, we use the geometrical relationship

$$\Delta L = \int_0^1 (1 - \cos\theta)\ \mathrm{d}S, \tag{5.10}$$

once we have solved for the beam shape $\theta(S)$.

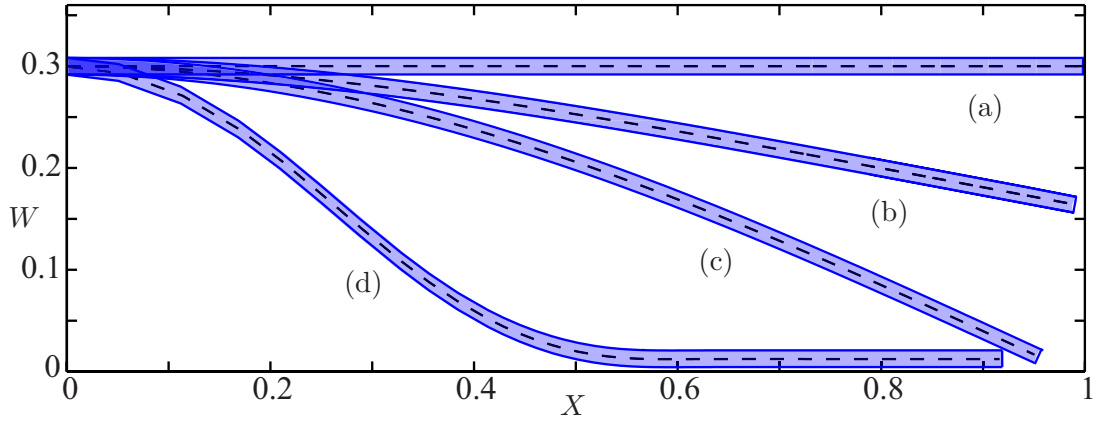

Figure 5.3.: Switch profiles for $d = 0.3$, $H = 0.01$ and different applied voltages, ψ: (a) $\psi = 0$, no deflection; (b) $\psi \approx \psi_{\text{p-i}}$, suspended state just before 'snap-through'; (c) pinned configuration, $\psi_{\text{pin}}^{(\text{min})} < \psi < \psi_{\text{pin}}^{(\text{max})}$; (d) clamped configuration, $\psi > \psi_{\text{clamp}}^{(\text{min})}$ (see text).

5.3. Numerical procedure and results

The system (5.8) subject to the boundary conditions (5.9) can readily be solved using the MATLAB boundary value problem solver `bvp4c`. As the applied voltage is increased or decreased, the evolution of states can be obtained using a straight-forward continuation scheme. Resulting deflection profiles are shown in figure 5.3.

We observe two distinct contact states: an arc-shaped, or *pinned*, state (profile (c) in figure 5.3), and a s-shaped, or *clamped*, state (profile (d)). We analyze the evolution of the switch as the applied voltage, ψ is varied, paying particular attention to the appearance of these adhered states. It is convenient to present this evolution in terms of the horizontal displacement of the free end, ΔL, since the transition between free, pinned and clamped states is marked by observable jumps in ΔL. Furthermore, in each of the observed states, ΔL evolves in qualitatively different ways with ψ: for the suspended beam, ΔL grows rapidly up to the pull-in voltage $\psi_{\text{p-i}}$; for the pinned state, ΔL decreases slightly with increasing ψ; finally, the clamped state features again a monotonic increase, where $\Delta L \to d$ as $\psi \to \infty$. (The decrease in ΔL for the pinned state is due to the increased attraction over the length of the beam, leading to the tip being pushed outwards.)

In general, the evolution of the switch with ψ runs along a hysteresis loop (illustrated in figures 5.5, 5.7 and 5.8): starting from a freely suspended beam, the system snaps to a pinned or clamped adhered state at $\psi_{\text{p-i}}$. Once pinned, the beam will transition to a clamped configuration at a critical voltage $\psi_{\text{pin}}^{(\text{max})}$ and remain in the clamped state as ψ is increased further. As ψ is reduced the beam will either remain in the clamped state or transition back to the pinned state and remain there as $\psi \to 0$, exhibiting non-volatile stiction in both cases. Otherwise, it will return to the freely suspended state for

$0 < \psi < \psi_{\text{pin}}^{(\text{min})}$ (volatile stiction). In the remainder of this section we will discuss the properties of this hysteresis loop in some detail.

We first consider the pull-in process as ψ is increased up to $\psi_{\text{p-i}}$ by looking at how the transition from suspended to adhered states is dependent on the switch parameters d and H. We then examine volatile and non-volatile stiction behaviour as ψ is decreased to zero.

We solve equations (5.8) – (5.9) for given values of the dimensionless parameters d, H, W^* and Γ. To guide the values of these parameters used in our calculations, we first consider a set of typical dimensional values for carbon-based NEM switch design. The strength of adhesion for graphene on different substrates has been reported to be $\Delta\gamma \simeq 0.04 - 0.3$ J/m^2 (Wang *et al.*, 2009; Zong *et al.*, 2010; Koenig *et al.*, 2011). We take $\Delta\gamma = 0.065$ J/m^2, which corresponds to typical carbon-carbon adhesion (Israelachvili, 1992), one of the scenarios discussed in Loh *et al.* (2011). The bending stiffness of few layered graphene can be approximated by $\mathcal{B} = bn^3$, where $b \simeq 18$ eV is the scaled bending stiffness and n is the number of molecular layers in the beam (Scharfenberg *et al.*, 2012). For example, a 30 layered graphene beam has thickness $h = 30h_1 \simeq 10$ nm (where $h_1 \simeq 0.33$ nm is the thickness of a graphene monolayer) and hence a bending stiffness $\mathcal{B} \simeq 7.8 \times 10^{-14}$ J. Typical beam lengths are $0.5 - 1.5$ μm (Loh *et al.*, 2011). Taking $l = 1$ μm we find $H = 0.01$ and a dimensionless strength of adhesion $\Gamma \simeq 0.08$. The dimensionless vdW radius is $W^* = 3.3 \times 10^{-4}$. In recent experiments, the switch height/beam length aspect ratio typically takes values $d \simeq 0.01 - 0.65$ (Chowdhury *et al.*, 2005; Scharfenberg *et al.*, 2012). In what follows, we will take the parameters $\Delta\gamma, b$ and w^* fixed to the values above. The only quantities that are varied are d and H (and later on l, to obtain figure 5.9).

5.3.1. Pull-in transitions

As ψ is increased, the initially straight beam gradually bends towards the bottom electrode, until it jumps to an adhered state at $\psi = \psi_{\text{p-i}}$. Whether this jump is to a pinned or to a clamped adhered state depends on both the switch height d and the beam thickness H.

In the limit $H \ll d$, the pinned state is extremely unstable. The reason for this is the following. The larger d, the greater the slope at the point of contact, $\theta(1)$. Consequently, the short range vdW forces act only on the very tip of the beam. As H becomes small, the contact region tends to zero, making a suspended-to-pinned transition less and less favourable (see figure 5.4).

We find that the stability of pinned states is also restricted in the limit $d \sim H \ll 1$. In this limit, the slope of the beam is small and the vdW forces act on a significant length

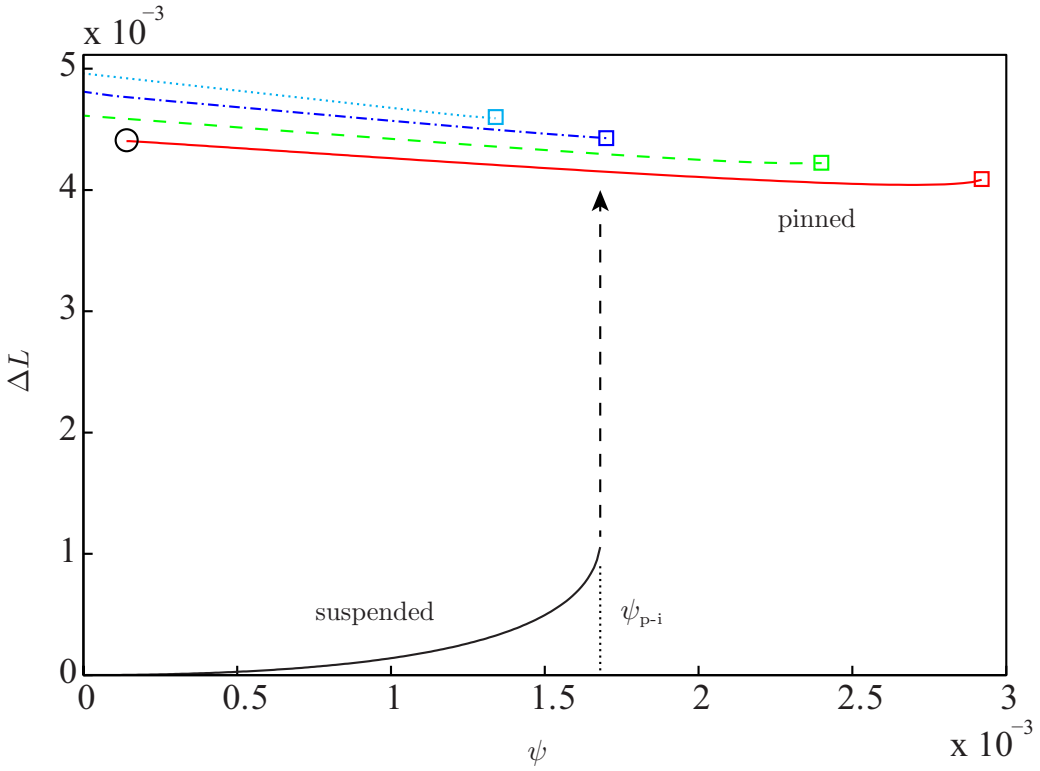

Figure 5.4.: $\Delta L(\psi)$ for four different beam thicknesses H, showing suspended and pinned states. Curves are shown for beams clamped at height $d = 0.1$ with thicknesses $H = 0.005$ (cyan dotted), $H = 0.007$ (blue dash-dotted), $H = 0.012$ (green dashed) and $H = 0.016$ (red solid). The squares mark the respective values for $\psi_{\text{pin}}^{(\max)}(H)$. The $\Delta L(\psi)$ dependence for freely suspended states is approximately independent of H, yielding indistinguishable curves for different thicknesses (black curve at base), with maximum value $\psi_{\text{p-i}}$. The dashed arrow marks the transition from suspended to pinned states. The black circle marks volatile pinned stiction for the thickest sheet.

of the beam. This causes the beam to 'zip up' and so the clamped configuration is again favoured over the pinned one (see figure 5.5). The dependence of these transitions on d and H can be quantified by looking at the critical voltages $\psi_{\text{p-i}}(d, H)$ and $\psi_{\text{pin}}^{(\max)}(d, H)$.

Our numerical results suggest that the pull-in voltage is approximately independent of H and scales as $\psi_{\text{p-i}} \sim d^3$. Computing a best fit power law gives $\psi_{\text{p-i}} \approx 1.702 d^3$ (represented by the solid line in figure 5.6 a). This scaling is in agreement with previous analytical estimates (Osterberg & Senturia, 1997; Dequesnes *et al.*, 2002) of $\psi_{\text{p-i}}(d)$, which calculated the (dimensional) pull-in voltage for a cantilever switch to be

$$V_{\text{p-i}} = \sqrt{\frac{32}{27}\left(\frac{2\mathcal{B}}{\epsilon_0 l}\right)\left(\frac{\delta}{l}\right)^3}. \tag{5.11}$$

In dimensionless terms this becomes $\psi_{\text{p-i}} = (\epsilon_0 l/2\mathcal{B}) V_{\text{p-i}}^2 \approx 1.185 d^3$. While the previously determined prefactor is lower than that found in our numerics, we note that in the deriva-

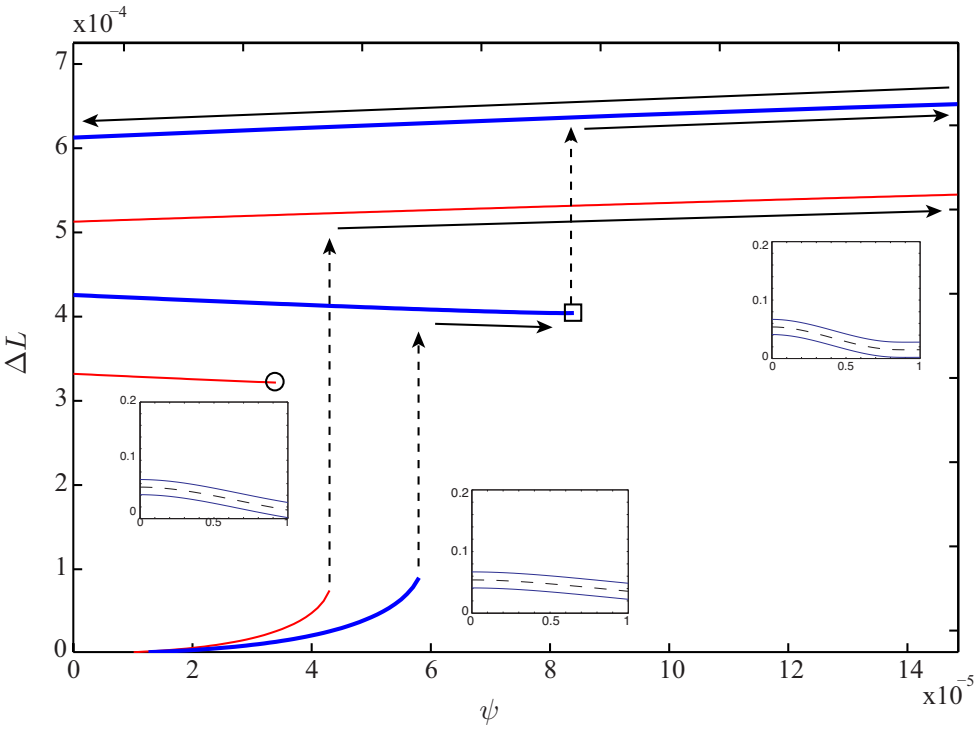

Figure 5.5.: The dependence of ΔL on ψ, for a beam of thickness $H = 0.012$ and suspended at heights $d = 0.030$ (red thin) and $d = 0.033$ (blue thick). The black circle and square correspond to the maximally adhered pinned states which are marked in figure 5.6. Dashed arrows show transitions between states, solid arrows illustrate the continuous evolution of each different state with varying voltage. Insets: profiles corresponding to the different (suspended, pinned, clamped) states.

tion of (5.11) the pull-in height is taken to be $w(l) = (2/3)\delta$. This value is based on the assumption that the electrostatic force, f_E, acts uniformly over the length of the beam, with its strength calculated based on the separation at the end of the beam. In reality, this overestimates f_E (and hence the pull-in height), since the free end is the point closest to the substrate; in fact f_E is significantly smaller towards the clamped end (at $s = 0$). Our model, on the other hand, computes pull-in explicitly, accounting for non-uniform f_E; as a rule of thumb, we find deflections consistently closer to $w(l) \simeq (1/2)\delta$.

Figures 5.4 and 5.5 show the evolution of $\Delta L(\psi)$. We find that transitions occur at $\psi = \psi_{\text{p-i}}$ and that the transition is from

$$\text{suspended} \to \text{pinned}, \quad \text{for} \quad \psi_{\text{p-i}}(d) < \psi_{\text{pin}}^{(\max)}(d, H),$$

but from

$$\text{suspended} \to \text{clamped}, \quad \text{for} \quad \psi_{\text{p-i}}(d) > \psi_{\text{pin}}^{(\max)}(d, H).$$

The functions $\psi_{\text{p-i}}(d)$ and $\psi_{\text{pin}}^{(\max)}(d)$ are shown in figure 5.6a, for $H = 0.012$. Critical

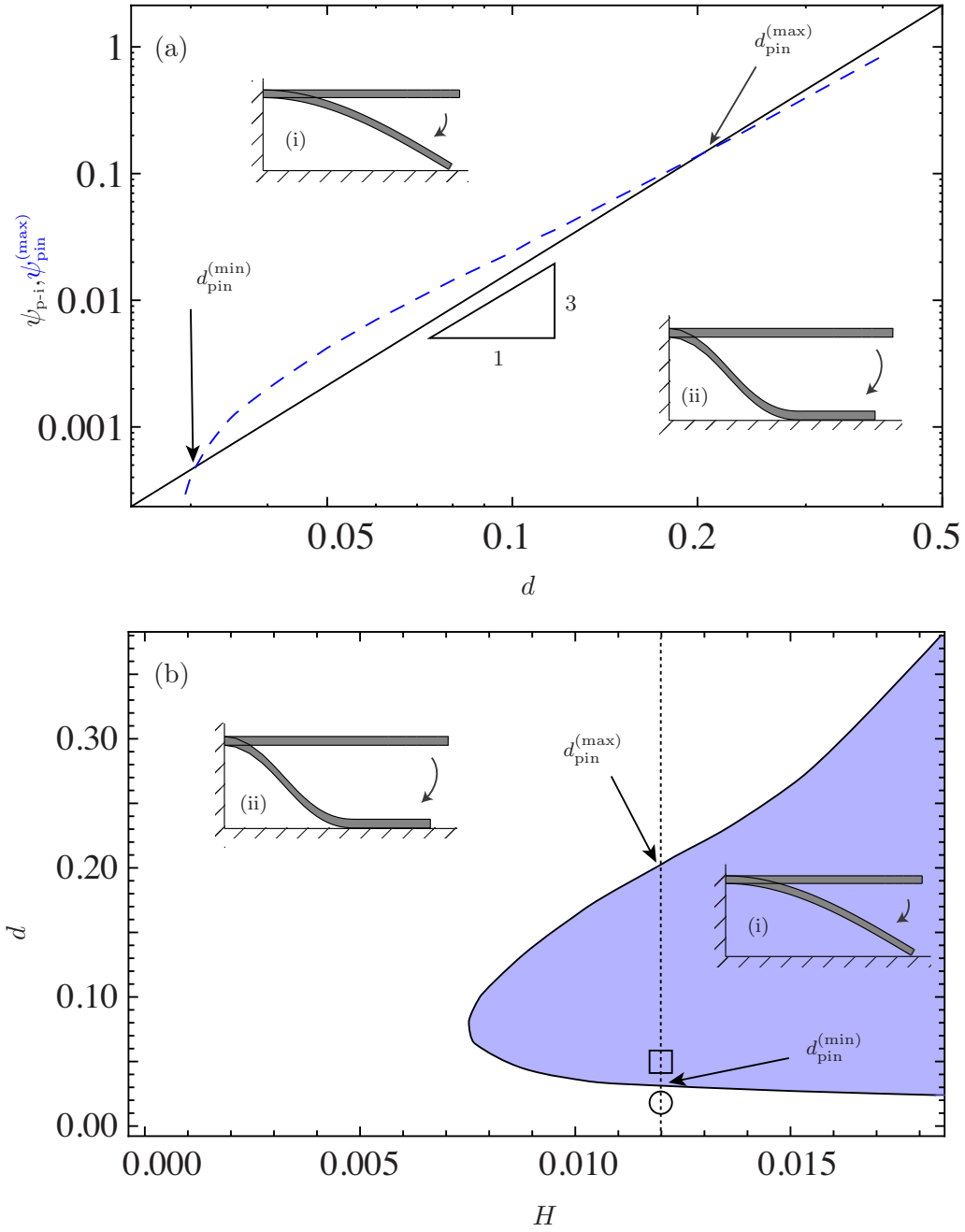

Figure 5.6.: (a) Log-log plots of transition voltages $\psi_{\text{p-i}}(d)$ (solid black) and $\psi_{\text{pin}}^{(\max)}(d)$ (blue dashed), for $H = 0.012$. When $\psi_{\text{pin}}^{(\max)} > \psi_{\text{p-i}}$, transitions from suspended to pinned states are observed – inset (i). When $\psi_{\text{pin}}^{(\max)} < \psi_{\text{p-i}}$, the system jumps straight from suspended to clamped states – inset (ii). Critical switch heights $d_{\text{pin}}^{(\min)}$ and $d_{\text{pin}}^{(\max)}$ are shown, demarcating the boundary between the two transitions. The scaling $\psi_{\text{p-i}} \sim d^3$ is illustrated. (b) regime diagram of pull-in transitions in (d, H) space. The blue area represents (d, H) values where the suspended-to-pinned transition is possible; the dotted line represents $H = 0.012$, with $d_{\text{pin}}^{(\max)}$ and $d_{\text{pin}}^{(\min)}$ as above. Circle and square correspond to the configurations shown in figure 5.5.

heights demarcating the modes of transition, are given by the solutions to

$$\psi_{\text{pin}}^{(\max)}(d, H) = \psi_{\text{p-i}}(d). \tag{5.12}$$

Interestingly, (5.12) has no solutions for thicknesses less than a critical value $H_{\text{pin}} \simeq 0.0072$, which means that for $H < H_{\text{pin}}$ the beam snaps from the freely suspended straight to the clamped state for all values of d. For $H = H_{\text{pin}}$, there is only one solution to (5.12), $d_{\text{pin}} \simeq 0.083$. For $H > H_{\text{pin}}$, there are two solutions, which we label $d_{\text{pin}}^{(\min)}$ and $d_{\text{pin}}^{(\max)}$. These results may be summarized in a regime diagram illustrating the parameter ranges for which each of the two contact (or adhesion) transitions occur – see figure 5.6b.

Figure 5.6 shows that the beam can only transition from suspended to pinned when $H > H_{\text{pin}}$ and $d_{\text{pin}}^{(\min)} < d < d_{\text{pin}}^{(\max)}$. Taking $H = 0.012$, we find $d_{\text{pin}}^{(\min)} = 0.031$, $d_{\text{pin}}^{(\max)} = 0.208$ and the two different scenarios are illustrated in figure 5.5: suspended $\rightarrow$ clamped for $d = 0.03$ (red thin) and suspended $\rightarrow$ pinned for $d = 0.033$ (blue thick).

5.3.2. Pull-out transitions: volatile and non-volatile stiction

The previous section was concerned with the process of pull-in as the voltage increases. In this section we examine the conditions under which contact remains when the applied voltage is removed; i.e. the conditions under which stiction failure occurs.

To study the limits of non-volatile stiction, we assume that the system is in its clamped state with a given maximum voltage $\psi_{\max}$. As the voltage is decreased the switch will remain in this state until it reaches $\psi_{\text{clamp}}^{(\min)}$. It will then transition to one of the other states as the voltage is decreased further (figure 5.7). Our numerical results suggest that $\psi_{\text{clamp}}^{(\min)} < \psi_{\text{pin}}^{(\max)}$ for all values of d and H, i.e. there is hysteresis between the two states. Since we also consistently find that $\psi_{\text{pin}}^{(\min)} < \psi_{\text{clamp}}^{(\min)}$, we observe that the clamped state will always transition to the pinned, rather than the suspended state. As the voltage is reduced to zero, we find that clamped stiction may remain, i.e. that $\psi_{\text{clamp}}^{(\min)}(d, H) < 0$ for some values of d and H. This is referred to as *non-volatile* clamped stiction, since stiction remains even when the voltage that caused it is removed. It is natural to ask, for a given thickness H, what is the minimum device height d needed to avoid non-volatile clamped stiction. This height d_{clamp} is found by solving

$$\psi_{\text{clamp}}^{(\min)}(d, H) = 0.$$

For $d < d_{\text{clamp}}$, the switch will remain in the clamped state when ψ is reduced to zero, whereas, for $d > d_{\text{clamp}}$, the state will transition to pinned when $\psi < \psi_{\text{clamp}}^{(\min)}$.

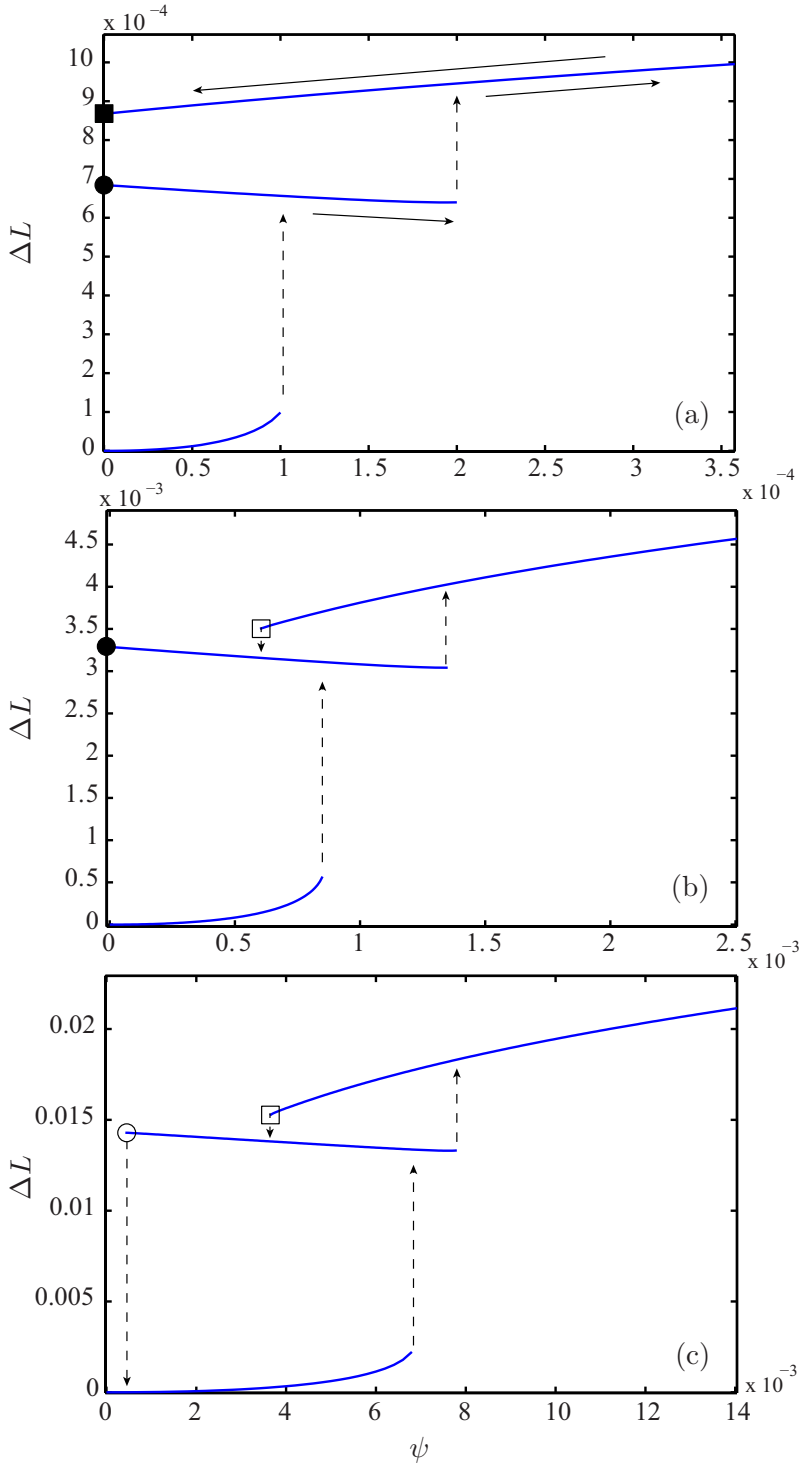

Figure 5.7.: The dependence of ΔL on ψ, for beam thickness $H = 0.012$: (a) $d = 0.04$, (b) $d = 0.08$ and (c) $d = 0.16$. Different curves in each subfigure correspond to suspended, pinned and clamped states, as illustrated in figure 5.5. Transitions between states are marked as dashed arrows, solid arrows in (a) highlight the hysteresis loop for increasing and decreasing voltages. Solid squares and circles mark states with non-volatile clamped and pinned stiction, respectively. Empty squares and circles mark clamped and pinned states exhibiting volatile stiction.

As ψ is further decreased below $\psi_{\text{clamp}}^{(\text{min})}$ the system remains in its pinned state until $\psi = \psi_{\text{pin}}^{(\text{min})}$. Again, if $\psi_{\text{pin}}^{(\text{min})} < 0$ we expect non-volatile stiction and the solution of $\psi_{\text{pin}}^{(\text{min})} = 0$ gives rise to a minimum device height to avoid non-volatile pinning, d_{pin}. For $0 < \psi < \psi_{\text{pin}}^{(\text{min})}$, the switch will be released and return to its freely suspended state. Volatile stiction is thus observed whenever $\psi_{\text{pin}}^{(\text{min})} > 0$. This hysteresis loop is shown in figures 5.7 and 5.8. Figure 5.7 illustrates the different stiction scenarios: (a) clamped for $d < d_{\text{clamp}}$; (b) pinned for $d_{\text{clamp}} < d < d_{\text{pin}}$ and (c) free when $d > d_{\text{pin}}$.

Figure 5.8 illustrates the behaviour of the switch in the large deflection regime, i.e. $d = \mathcal{O}(1)$, for the specific case $d = 0.5$ and $H = 0.012$. The evolution of $\Delta L(\psi)$ is found to be qualitatively similar to that already discussed for the limit $d \ll 1$. As argued above (and illustrated in figure 5.6), we observe a suspended-to-clamped transition in this case, since $d > d_{\text{pin}}^{(\text{max})}$.

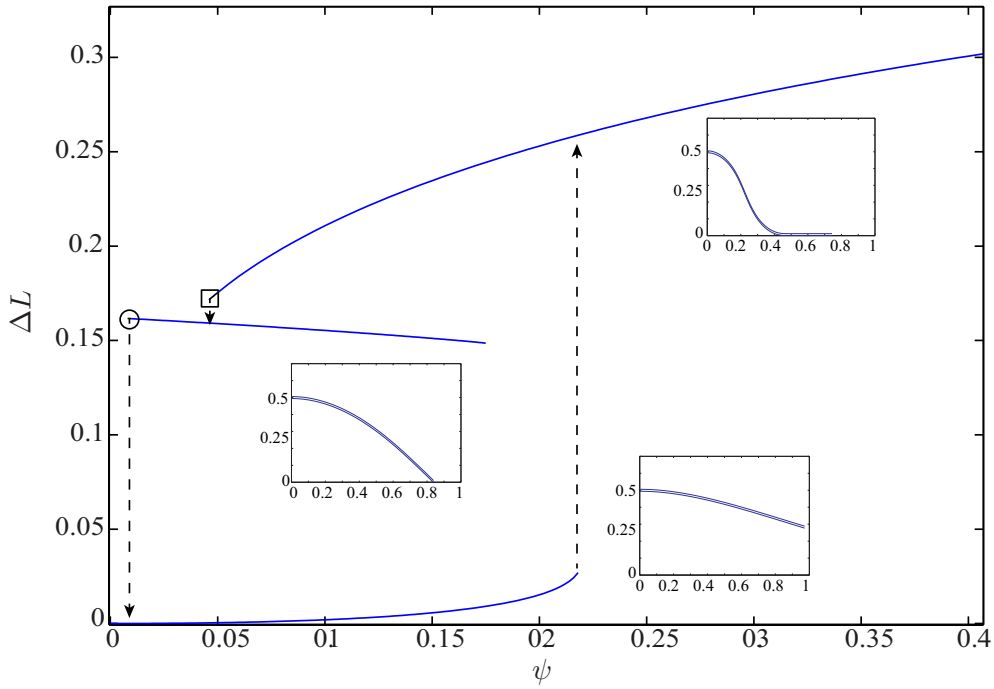

Figure 5.8.: $\Delta L(\psi)$ for the large deflection case, $d = 0.5$ ($H = 0.012$). Empty squares and circles again mark volatile clamped and pinned stiction, respectively. Insets show example profiles of the beam in each of the three possible states.

From an experimental point of view d_{pin} is likely to be the most important parameter, since systems with $d > d_{\text{pin}}$ will exhibit volatile stiction, while those with $d < d_{\text{pin}}$ will exhibit some form of non-volatile stiction. By fixing ℓ_{ec} (i.e. $\mathcal{B}$ and $\Delta\gamma$) and varying the switch length l, we can compute dimensional values for boundary heights $\delta_{\text{clamp}}(l)$ and $\delta_{\text{pin}}(l)$ (figure 5.9). These conditions specify the minimum height of a switch required to avoid stiction failure (for given material parameters and beam length).

5.4. Linear stiction boundaries

We have seen that the question of most practical interest is whether a system undergoes volatile or non-volatile stiction, i.e. when does the beam's state at zero external voltage remain adhered? To gain physical and analytical insight, we consider the small deformation limit (where $\mathrm{d}w/\mathrm{d}x \ll 1$). In this limit, the shape of the cantilever satisfies the beam equation

$$\mathcal{B}w'''' = 0. \tag{5.13}$$

In the case of clamped adhesion, the boundary conditions are $w(\lambda) = w'(\lambda) = 0$, where λ is the x-coordinate of the point at which contact first occurs (see figure 5.1). At the origin, the boundary conditions remain the same as for the nonlinear theory, namely $w(0) = \delta$, $w'(0) = 0$.

For the clamped adhered state, the profile of the beam is then found by solving (5.13), subject to clamped boundary conditions (Mastrangelo & Hsu, 1992)

$$w(x) = \begin{cases} \delta\left[1 - \frac{x^2}{\lambda^2}\left(3 - 2\frac{x}{\lambda}\right)\right], & 0 \le x < \lambda \\ 0, & \lambda \le x \le l. \end{cases} \tag{5.14}$$

Since the point of delamination λ is not known a priori we need to impose the familiar delamination condition (1.19), which in this case reduces to $w''(\lambda) = \sqrt{2}/\ell_{ec}$, since the substrate is flat. This gives $\lambda = \left(3\sqrt{2}\delta\ell_{ec}\right)^{1/2}$.

Having determined λ for a given value of l, we are able to predict whether the beam will remain in the clamped state after the voltage is removed: if $\lambda < l$, stiction is expected to occur, whereas for $\lambda > l$, the beam will be released or transition to the pinned state. It is a simple matter to derive an expression of critical switch dimensions for given material characteristics. This calculation was performed by Mastrangelo & Hsu (1992) who found:

$$\delta_{\text{clamp}} = (\sqrt{2}/6)l^2/\ell_{ec}. \tag{5.15}$$

5.4.1. The pinned delamination condition

For a pinned state we have $\lambda = l$ and the boundary conditions are $w(l) = w''(l) = 0$, since the sheet is no longer flat at $x = l$ but instead experiences zero moment at the point of pinning. In this section we derive an analogue of the clamped delamination condition (5.15) appropriate for a pinned boundary condition. This is done by balancing the shear force acting on the beam at the point of pinning with the explicit van der Waals force acting near $x = l$.

We solve (5.13) subject to clamped conditions at $x = 0$ and pinned conditions at $x = l$, to find

$$w(x) = \delta \left[1 + \tfrac{1}{2} \left(\frac{x}{l} \right)^2 \left(\frac{x}{l} - 3 \right) \right]. \tag{5.16}$$

For the angle and the shear force at the pinning point we have

$$\varphi \simeq w'(l) = -3\delta/2l, \qquad F_{shear} = \mathcal{B}w'''(l) = 3\mathcal{B}\delta/l^3. \tag{5.17}$$

We aim to relate this shear force to the the van der Waals force, F_{vdW} by utilizing the earlier result (1.10) which relates the macroscopic concept of adhesion to the short range vdW interaction. For pinned states, we expect these forces to cancel each other. Let us consider the van der Waals force per unit length, f_{vdW}. From (5.2) and (1.10), we find that in the linear limit (and for $w^* \ll h$)

$$f_{vdW} = -\tfrac{8}{3}\Delta\gamma w^{*2} \left\{ w_-^{-3} - w_+^{-3} - w^{*6} \left[w_-^{-9} - w_+^{-9} \right] \right\}, \tag{5.18}$$

where $w_- = w - h/2$ and $w_+ = w + h/2$. To get the total vdW force acting on the beam, F_{vdW}, we integrate over the length of the beam. We assume that near contact (the only region where the van der Waals force is significant) the profile of the beam can be written as

$$w = w^* + h/2 + \varphi(l - x), \tag{5.19}$$

i.e. a straight line with contact distance of the mid plane $w(l) = w^* + h/2$ and a slope φ. This is justified since there is no bending moment acting on the pinned end and all angles are taken to be small. Substituting (5.19) into (5.18) and integrating from $x = -\infty$ to 0, we obtain an analytic, but cumbersome, expression for $F_{vdW} = F_{vdW}(\Delta\gamma, h, w^*)$. Since the vdW force is only significant very close to the pinning point the integral converges, even for small values of φ.

Performing a series expansion in w^*, we find

$$F_{vdW} = \frac{\Delta\gamma}{\varphi} \left[1 - \frac{4}{3} \left(\frac{w^*}{h} \right)^2 + \frac{8}{3} \left(\frac{w^*}{h} \right)^3 - ... \right]. \tag{5.20}$$

But since $w^* \ll h$, this gives to a good approximation $F_{vdW} \simeq \Delta\gamma/\varphi$.

We postulate that the boundary of non-volatile pinning is found at equilibrium between the shear force due to bending, F_{shear} and the short range vdW force acting at the pinned end, F_{vdW}. Thus combining (5.17) and (5.20) and rearranging suitably gives following pinning condition:

$$|w'''(l)w'(l)| = 1/\ell_{ec}^2. \tag{5.21}$$

Substituting this into (5.16) yields an expression for the critical pinning height:

$$\delta_{pin} = (\sqrt{2}/3)l^2/\ell_{ec}. \tag{5.22}$$

Comparing this to the critical clamping height, (5.15) we finally find $\delta_{pin} = 2\delta_{clamp}$. This means that the switch has to be twice as high as the clamping stiction condition predicts to avoid pinned stiction.

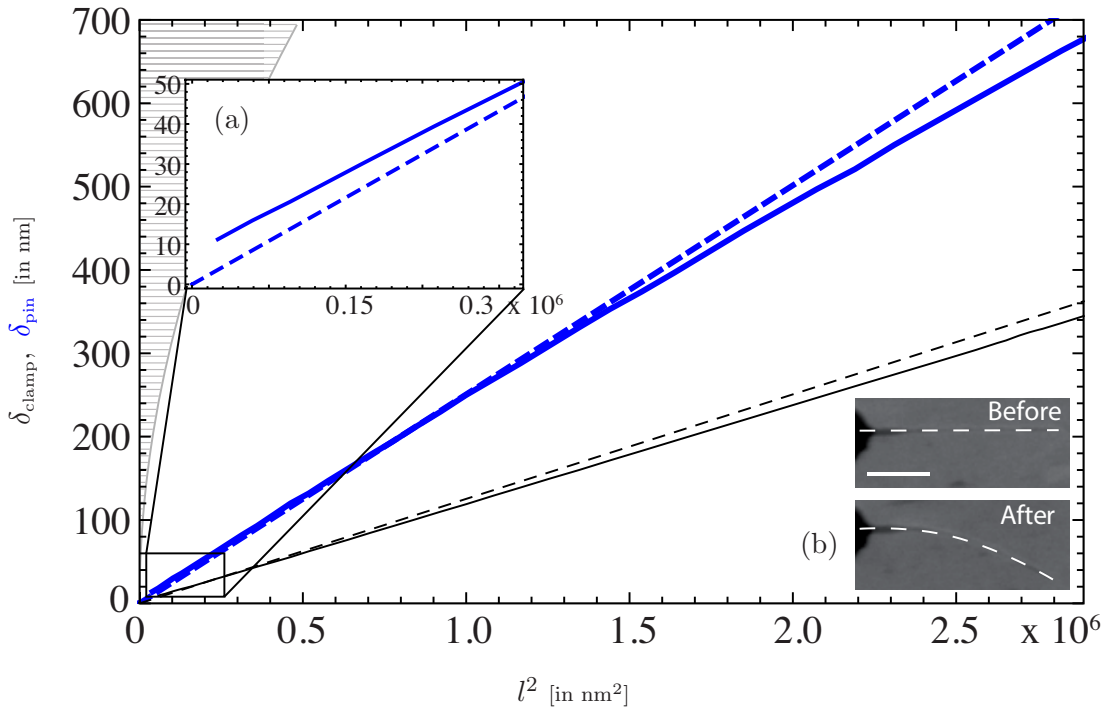

Figure 5.9.: Stiction boundaries for pinned (blue thick) and clamped (black thin) states. The dashed curves give the linear asymptotic results. The lined region represents the geometrically inaccessible region $\delta > l$. Inset (a): detail of the limit $H \sim d$. Inset (b): pinned non-volatile stiction shown on scanning electron micrographs, scale bar is 500 nm (reproduced from (Loh *et al.*, 2011), dashed lines added by the author to highlight the beam shape).

The critical stiction heights were derived previously by Mastrangelo & Hsu (1992), who arrived at the result (5.22) by considering shear deformation near the tip when the beam is clamped, letting $\lambda \to l$. However, I believe that the pinning condition (5.21) is novel.

5.4.2. Comparison to the nonlinear model

In the regime $h \ll \delta \ll l$, the asymptotic results give numbers that are in good agreement with the numerical results of the nonlinear model, as described in the previous sections. In particular, results for the limits at which the different modes of non-volatile stiction are observed are illustrated in figure 5.9. It is interesting to observe that good agreement is

obtained for relatively large aspect ratios $d = \delta/l$: the upper limit of figure 5.9 corresponds to $d = 0.3$. This suggests that the boundary conditions (5.15), (5.22) may be applied with reasonable confidence to experimental settings where d is not necessarily small. However, beyond $d \approx 0.3$ the differences between the results of the linear and nonlinear models become increasingly significant.

Figure 5.9, inset (a) highlights the divergence of asymptotic and numerical results when $h \sim \delta$. This is due to the effects of the finite beam thickness on the vdW forces. The lined region in figure 5.9 represents the geometric constraint $\delta > l$, where contact between beam and substrate is geometrically impossible.

A scanning electron micrograph is shown in figure 5.9, inset (b), reproduced from Loh *et al.* (2011), which highlights, firstly, that deflections in modern applications are not necessarily small and, secondly, that pinning is possibly the most relevant state when assessing stiction failure of a NEM switch. This is further supported by other experiments featuring pinned states such as the one shown in figure 1.2.

5.4.3. Comparison to experimental data

Finally, we compare the stiction boundaries presented here to experimental data, published in Loh *et al.* (2011) and reproduced in Loh & Espinosa (2012). This experimental data was obtained using multiwalled carbon-nanotube (CNT) cantilever switches. Continuum beam models like that developed here can be applied to CNT switches for nanotubes with more than $\sim$4-5 layers (Ru, 2000; Dequesnes *et al.*, 2002). In the experiments, typical CNTs had $\sim$25 layers with a 0.33 nm interlayer spacing. The height of the switch took values $\delta = 30-800$ nm and the beam length ranged from $l = 470-1580$ nm. Following the earlier comparison to experiments (section 5.3), we set the parameters in our numerical model to be $w^* = 0.33$ nm and $h = 8$ nm.

We reproduce the experimental data for a carbon beam-carbon substrate switch in figure 5.10 (Loh *et al.*, 2011), together with the scaling law presented in the original paper, $\delta_{\text{clamp}} \sim l^4$ (dotted line). This scaling law was based on the assumption that stiction is determined by the total adhesive energy stored in the adhered segment of the beam, for a given point of delamination, λ (Loh *et al.*, 2011). However, as discussed above, λ is not known a priori. In fact, stiction boundaries should be found by solving for λ, which is dependent on the geometric and material parameters of the system. The resulting clamped and pinned stiction conditions (5.15), (5.22) are shown in figure 5.10 (dashed and solid, respectively). Since the strength of carbon-carbon adhesion is not precisely known the figure shows a range of possible values for $\Delta\gamma$ in the range $0.01 \leq \Delta\gamma \leq 0.1$ J/m^2. We find generally good agreement between the experimental data and the stiction boundaries presented here.

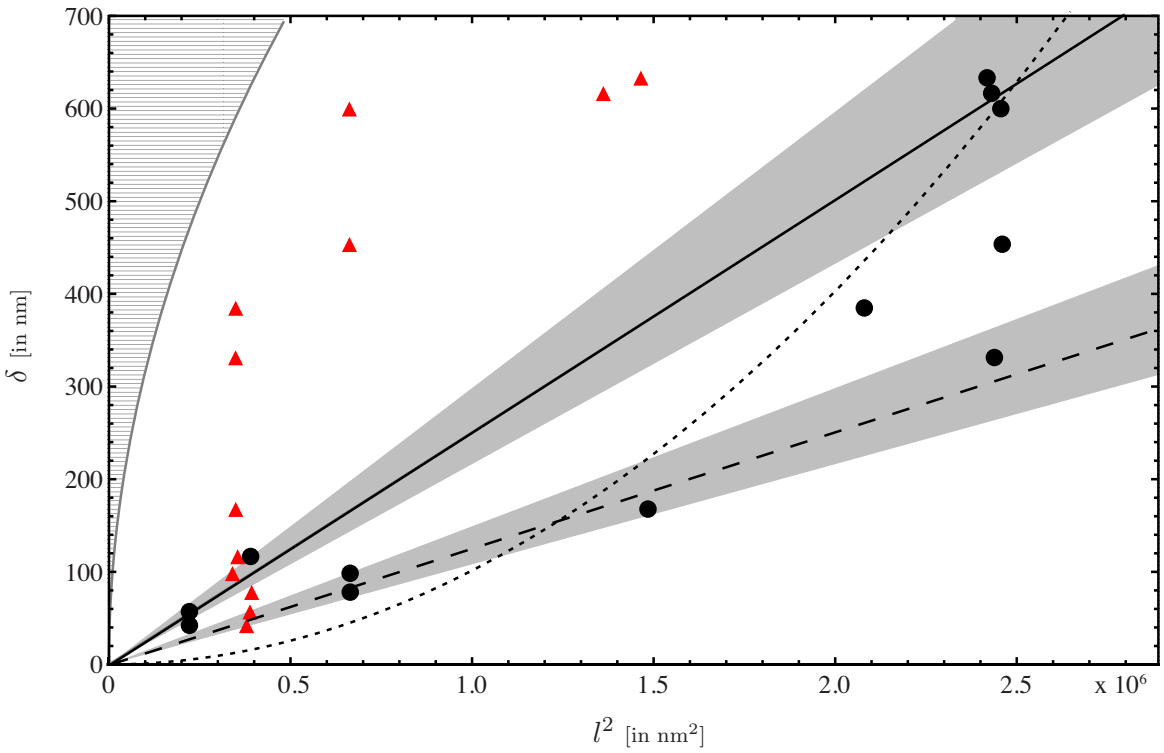

Figure 5.10.: Stiction boundaries δ_{pin} (solid) and δ_{clamp} (dashed), plotted as functions of l^2, giving straight lines, as suggested by (5.15) and (5.22). The shaded regions around the boundaries account for the uncertainty in $\Delta\gamma$ and range from $\Delta\gamma = 0.1$ (top limit) to 0.01 J/m^2 (bottom limit). Red triangles represent experimental data points of systems that exhibit volatile stiction, while black circles represent systems with non-volatile stiction. The dotted line corresponds to the scaling law $\delta \sim l^4$, presented in Loh *et al.* (2011).

5.5. Conclusions

We have presented a theoretical, quasi-static study of stiction processes in contact switches. Incorporating the effects of geometrically non-linear deflections and finite beam thickness, we discussed in detail the hysteresis loop that describes the closing/opening processes of a contact switch as the applied voltage is ramped up or down.

The hysteresis loop was found to consist of two kinds of processes: (a) the continuous evolution of a given state (freely suspended, pinned adhered or clamped adhered) and (b) discontinuous jumps between these three states at critical values of the applied voltage.

We found that pull-in (the transition from freely suspended to a contacting regime) can result in either a pinned or a clamped state. Suspended-to-pinned transitions are found to occur only for sufficiently thick sheets, and when the switch height is larger than a critical value. Outside this range, the beam will snap from the suspended state straight to a clamped configuration. We believe that the mode of transition may have important

implications for the second main failure mechanism in NEM contact switches: ablation. In ablation the beam tip is damaged and the beam gradually shortens as the switch undergoes repeated ON/OFF cycles. Whether the initial contact with the bottom electrode occurs with a 'flat' or an angled tip is likely to affect this damage process. However, ablation failure is very much governed by the dynamic behaviour of the switch and hence is beyond the scope of this chapter.

The pull-out behaviour of a system (the transition back to a free state) was shown to be governed by the critical heights $\delta_{\text{pin}}(l)$ and $\delta_{\text{clamp}}(l)$. If $\delta < \delta_{\text{clamp}}$, the switch will get stuck in the clamped state. For $\delta_{\text{clamp}} < \delta < \delta_{\text{pin}}$, the switch is expected to suffer non-volatile pinned stiction. If $\delta > \delta_{\text{pin}}$, on the other hand, the switch will return to its original open configuration once the voltage is removed and the stiction is volatile, as usually desired.

By considering a linearized framework, analytical estimates of these critical heights were presented and compared to the results of our numerical model. We found close agreement between the two for a large range of switch aspect ratios. In particular, the commonly used analytic results present a practical and valid solution for values of δ/l up to ~ 0.3. It also emerged that the stiction conditions are in good agreement with recent experimental data.

We further considered the critical pull-out voltages $\psi_{\text{pin}}^{(\text{min})}$ and $\psi_{\text{clamp}}^{(\text{min})}$. Since these minimum voltages were found to be consistently lower than the pull-in voltage, $\psi_{\text{p-i}}$, it is clear that significant hysteresis between free and adhered states exists. Also, the minimum clamped voltage, $\psi_{\text{clamp}}^{(\text{min})}$ was observed to be always lower than the pinned-to-clamped transition voltage, $\psi_{\text{pin}}^{(\text{max})}$, suggesting further hysteresis between the two adhered states. This lends further support to the idea that the dynamics of the respective transitions may play an important role with respect to the stability of the different states. We conclude that a study of the dynamic processes of the switch cycle would present an interesting starting point for future work.

Chapter 6

Epilogue

6.1. Summary of results

In this thesis we have studied the adhesion of thin elastic sheets in contact with an underlying substrate. The focus of this thesis has been on the interplay between material and geometric properties of a system and how this interplay determines the equilibrium states of the sheet. A recurring theme in these studies was the effect of geometrically nonlinear deformations. Furthermore, each chapter presented a modelling problem that was inspired by applications in modern technology.

Chapters 2 and 3 were concerned with two of the simplest scenarios of a thin adhered sheet that is subjected to a compressive stress. In Chapter 2 the sheet of interest is deposited on a rigid substrate – the 'Sticky Elastica'. In Chapter 3 we considered the case of a sheet floating on a liquid – the 'Floating Carpet'. Both problems are concerned with the shape of the delamination blisters that were formed as a response to compression of the sheet. The key difference between the two setups lies in the geometry of the sheet at the contact point: for a rigid substrate, a discontinuity in curvature is observed but for a liquid, the curvature is continuous. In the case of the Sticky Elastica, the discontinuity in curvature is related to the elastocapillary length of the system; this allowed us to present expressions for the elastocapillary length in terms of the width and height of a typical blister. From asymptotic considerations we showed that the elastocapillary length can

be estimated from the typical curvature and the aspect ratio of the delamination blister alone. This presents a generalization of existing linear asymptotic results and is found to be accurate for blisters undergoing large compressions, even up to the point of self contact. Whereas the Sticky Elastica is pertinent for understanding the final equilibrium state of delamination blisters, the study of 'Floating Carpets' in Chapter 3 focused on when blisters form in the first place. It is well known that, for an initially adhered sheet, delamination blisters can supersede wrinkles at a critical compression. Since studying this transition is a difficult problem when the substrate is made of elastic material, we considered the case of a sheet floating on a liquid. From energetic considerations we were able to compute the critical compression at which blisters are energetically favourable. We established a 'blistering inequality' that demarcates the wrinkled and blistered regimes for given material and geometric parameters. Finally, we observed that for both the Sticky Elastica and the Floating Carpets, the blister size evolves non-monotonically as the compression is increased. This is a feature that is not accounted for by the linearized analyses that have been presented previously. This feature is also absent from the classical elastica; it occurs because the additional physics present in both of these examples gives rise to an evolving arc-length of de-adhered material as the compression is increased.

In Chapter 4 we investigated the deposition of thin sheets onto rigid, corrugated substrates. This was motivated by recent experiments which made the somewhat unexpected observation that graphene flakes would either rest completely flat on top of a corrugated substrate or fully conform to the shape of that substrate. Intermediate, partially conformal configurations were not observed. By means of an analytical (small deformation) model and again considering the relation of material and geometric properties, we were able to offer an explanation for this so-called 'snap-through' behaviour: for given material properties, the curvature near the peaks of the substrate needs to be smaller than a critical value (given by the delamination condition of section 1.3.3) to allow for partial conformity. For substrates with curvatures larger than this critical value, the energetic penalty in bending outweighs the energetic benefit of adhering over an intermediate length. We found that the sinusoidal substrate shape (considered in the experiments above) indeed features curvatures that are too large to allow for partial adhesion. We further presented a substrate, qualitatively similar to the sinusoidal one, which does allow for partial conformity. Finally, we suggested a class of substrates that features an entirely smooth transition from flat to conformal states. This might be of particular interest to experimentalists, since, if the substrate shape is known, the elastocapillary length can be inferred from the adhered region in a single experiment rather than multiple experiments with few layer graphene sheets of various thicknesses.

A detailed model of a particular technological application was the subject of Chapter 5: the nanoelectromechanical contact switch. With the continued downsizing of electronic

devices van der Waals forces play an increasingly important role in system design and can lead to irreversible stiction – a major engineering obstacle in nanoelectromechanical switches. We developed a theoretical model that accounts for non-linear deflections to study the adhesion behaviour of a cantilever switch as it goes through its ON/OFF cycle. Previous work had focused only on one or the other of two processes: the deformation up to the point of pull-in, or the possible stiction phenomena beyond pull-in. Our aim was to complete this picture by looking in detail at the transitions between free and adhered states. In agreement with previous work, two qualitatively different adhered states were found, namely a 'pinned' and a 'clamped' one. Our numerical analysis produced a hysteresis loop between free, pinned and clamped states, which suggests that the dynamics of the switch cycle may play an important role in the problem. Two modes of pull-in were found: depending on switch geometry and material properties, the switch would either transition from freely suspended states to pinned states or from suspended straight to clamped states. Which of these transitions occurs may be important for the commonly observed ablation of the beam tip over repeated ON/OFF cycles. The pull-out behaviour, on the other hand, is likely to always be determined by the pinned state, which can cause stiction for much lower voltages than its clamped counterpart. This is important, since it suggests that one should consider the pinned stiction boundary when looking for switch geometries that avoid stiction, rather than the commonly considered clamped stiction boundary.

6.2. Future work

The work presented in this thesis is only the first step towards a full understanding of the systems at hand. In the following paragraphs, I highlight some of the major open questions that might prove interesting to consider in further studies. In the last section a possible future project is introduced, which in many ways is an obvious continuation to the problems studied and promises to shed further light on the adhesion and deformation processes of thin sheets: the 'Curly Peel Test'.

6.2.1. From static to dynamic systems

In the studies above, we have only considered static (or quasi-static) scenarios. The evolution of a physical system, however, is never static – in particular, the transitions between different states are often governed by the dynamic nature of the system. As pointed out before, the hysteretic behaviour that we commonly observed suggests that dynamic processes may play a crucial role in these systems – a role that is important to understand better.

Local energy minima can cause significant hysteresis: for example, in the case of a sheet stuck to an elastic substrate the transition from wrinkled to blistered states occurs at a large critical compression, resulting in a discontinuous transition from wrinkles to blisters with a finite size. However, as the compression is subsequently reduced, the reverse transition from blisters to wrinkles has been observed to be almost smooth (Vella *et al.*, 2009*a*). For a sheet resting on a liquid surface, on the other hand, very little hysteresis is observed, as discussed in Chapter 3. The reasons behind these different hysteretic behaviours are yet to be uncovered and promise to be an interesting starting point for a study into the dynamics of wrinkling and blistering.

A related question is how blisters appear in the first place. For a floating sheet they are found to nucleate at the sheet edge and one can observe the blister gradually propagating towards the centre. A similar phenomenology is found for blisters on solid substrates, although the crack opening usually happens too fast to be observed by the naked eye. It is an open question how this gradual growth affects the wrinkling to blistering transition and what its relative importance is for different substrate and sheet configurations.

Similarly, graphene nanotubes brought into self-contact are known to first stick at a certain point and then 'zip-up' into a fully adhered configuration (Cohen & Mahadevan, 2003). In our study of graphene on a grooved substrate we observed that there is often more than one possible adhered or partially adhered state (for a given set of parameters and geometric constraints). The state that the system adopts is therefore determined by the way the sheet is deposited (i.e. by the system's initial state) or by the dynamic process of crack propagation. Further studies into the stability of the individual states and the role of the dynamics of adhesive processes promise to shed light on the physics that governs the deposition of graphene.

In much the same way, we found significant hysteresis in NEM switches between freely suspended and adhered states. This is directly linked to the second major engineering issue in switch design (next to stiction failure): ablation of the tip of the switch over repeated ON/OFF cycles. We suspect that some transitions from free to adhered states are less damaging than others. In our work so far we developed static boundaries between possible states. But to obtain a full understanding of the closing/opening mechanisms of a NEM switch, dynamic processes again need to be considered. This is aimed at yielding better geometric and material parameters that allow for switch design that avoids stiction and ablation.

6.2.2. The 'Curly Peel Test'

A problem that I believe could prove a particularly interesting continuation of the projects described in this thesis is the 'Curly Peel Test'. Peel tests are an established method to

characterize adhesive bonds. In a peel test, a thin sheet that is initially fully adhered to a substrate is partially peeled off by applying a pulling force to one of its ends (Kendall, 1973; Maugis, 1992). For known material properties of the sheet, measuring the applied force together with the resulting geometry gives insight into the strength of adhesion between sheet and substrate.

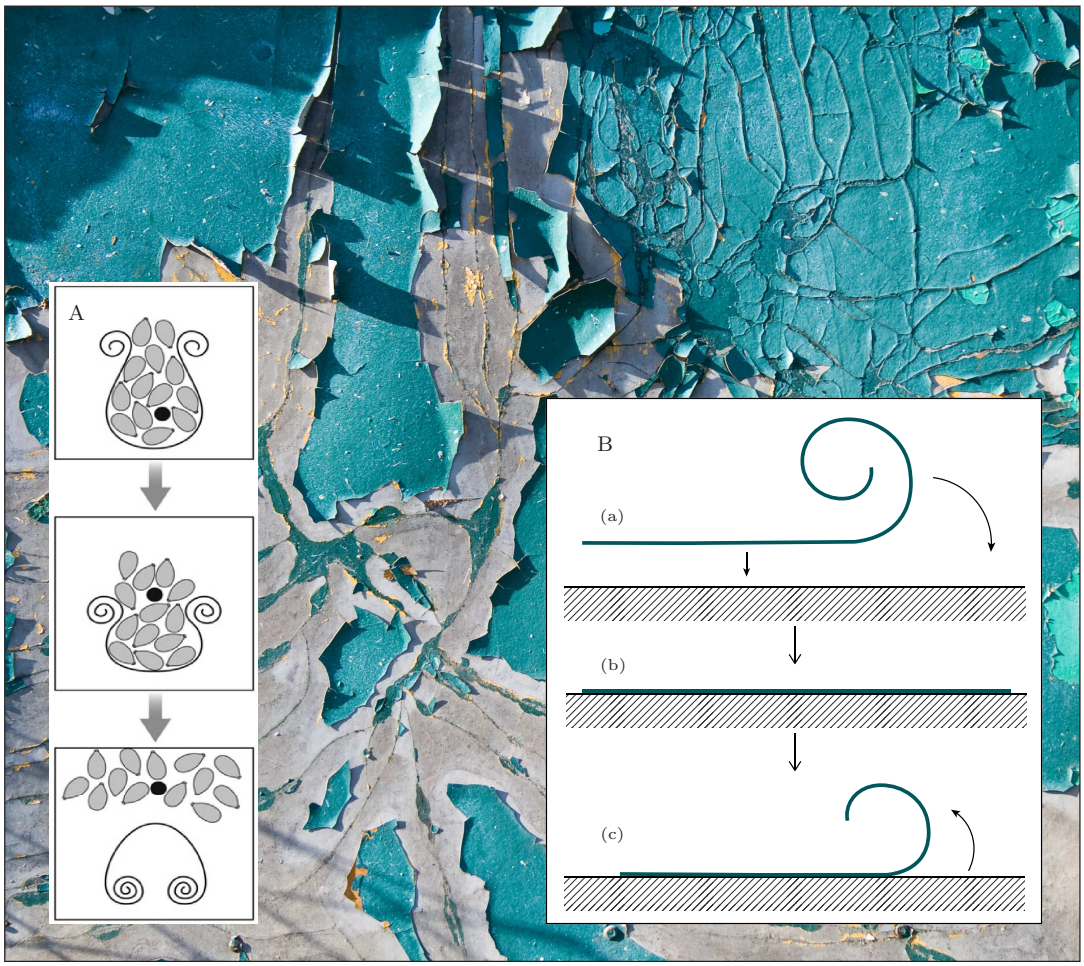

Figure 6.1.: Peeling paint. Inset A: schematic of curling-buckling vesiculation of the membrane in red blood cells (reproduced from Lew (2011)). Inset B: diagram of a 'curly peel test' – (a) a naturally curved elastica is brought into contact with an adhesive substrate; (b) the sheet is forced into adhesion over its entire length; (c) delamination occurs upon release due to the natural curvature of the sheet.

We propose to study a slightly modified version of the conventional peel test. Instead of looking at the usual case of a flat sheet, the idea is to look at the peeling of a naturally curved elastica: instead of having to apply a controlled force, the peeling is now driven solely by the intrinsic curvature of the sheet, as illustrated in figure 6.1 B. This would enable us to infer the strength of adhesion from the bending rigidity of the shell and the final system geometry alone – without having to apply and measure an additional external

force. The idea was motivated by recent work on curling (Callan-Jones *et al.*, 2012) and by the multitude of curved elastica in nature, such as cell membranes, curly hair or dry, peeling paint, as shown in figure 6.1 (Mabrouk *et al.*, 2009; Lew, 2011). Naturally curved sheets have further received attention with regards to applications in modern technologies (Yu *et al.*, 2003) and phenomena such as graphene 'scrolling' are subjects of much current research (Shioyama, 2001; Viculis *et al.*, 2003). On one hand, the 'curly peel test' promises to give insight into how naturally curved sheets adhere to a substrate in general. On the other hand, the proposed test might make it possible to measure the strength of adhesion of materials that fail in conventional peel tests, such as fragile sheets that cannot support the required pulling force.

Bibliography

Aitken, Z. H. & Huang, R. 2010 Effects of mismatch strain and substrate surface corrugation on morphology of supported monolayer graphene. *J. Appl. Phys.* **107** (12), 123531.

Aoyanagi, Y., Hure, J., Bico, J. & Roman, B. 2010 Random blisters on stickers: metrology through defects. *Soft Matter* **6** (22), 5720–5728.

Armand 2008 *Potassium Carbonate Handbook*. Armand Products Company.

Audoly, B. & Pomeau, Y. 2010 *Elasticity and Geometry*. Oxford University Press.

Balkcom, D. & Mason, M. 2008 Robotic origami folding. *Int. J. Robot. Res.* **27** (5), 613–627.

Bernoulli, J. 1692 Quadratura curvae, e cujus evolutione describitur inflexae laminae curvatura. *Die Werke von Jakob Bernoulli* pp. 223–227.

Bico, J., Roman, B., Moulin, L. & Boudaoud, A. 2004 Elastocapillary coalescence in wet hair. *Nature* **432**, 690.

Bodetti, N., Koenig, S., Xiao, J., Bunch, S. & Dunn, M. 2012 Graphene blister adhesion mechanics. *Bull. Am. Phys. Soc.* .

de Boer, M., Knapp, J., Michalske, T., Srinivasan, U. & Maboudian, R. 2000 Adhesion hysteresis of silane coated microcantilevers. *Acta Mater.* **48** (18), 4531–4541.

Bouville, M., Chi, D. & Srolovitz, D. J. 2007 Grain-boundary grooving and agglomeration of alloy thin films with a slow-diffusing species. *Phys. Rev. Lett.* **98**, 085503.

Bowden, N., Brittain, S., Evans, A. G., Hutchinson, J. W. & Whitesides, G. M. 1998 Spontaneous formation of ordered structures in thin films of metals supported on an elastomeric polymer. *Nature* **393** (6681), 146–149.

Brau, F., Vandeparre, H., Sabbah, A., Poulard, C., Boudaoud, A. & Damman, P. 2011 Multiple-length-scale elastic instability mimics parametric resonance of nonlinear oscillators. *Nature Phys.* **7**, 56–60.

Brotchie, J. & Silvester, R. 1969 On crustal flexure. *J. Geophys. Res.* **74** (22), 5240–5252.

Callan-Jones, A., Brun, P. T. & Audoly, B. 2012 Self-Similar Curling of a Naturally Curved Elastica. *Phys. Rev. Lett.* **108** (17), 174302.

Cao, Y. & Hutchinson, J. 2012 Wrinkling phenomena in neo-hookean film/substrate bilayers. *J. Appl. Mech.* **79** (3), 1019.

Cerda, E. & Mahadevan, L. 2003 Geometry and physics of wrinkling. *Phys. Rev. Lett.* **90** (7), 74302.

Chakraborty, S., Bhattacharya, A. & Bhattacharyya, T. 2011 Experimental analysis of pull-out voltage of electrostatically actuated microcantilever beam based on contact-stiction model. *Micro Nano Lett.* **6** (1), 43–47.

Chan, E., Garikipati, K. & Dutton, R. 1999 Characterization of contact electromechanics through capacitance-voltage measurements and simulations. *J. Microelectromech. S.* **8** (2), 208–217.

Chen, Z., Cotterell, B. & Wang, W. 2002 The fracture of brittle thin films on compliant substrates in flexible displays. *Eng. Fract. Mech.* **69**, 597–603.

Cheng, H., Wu, J., Li, M., Kim, D. H., Kim, Y. S., Huang, Y., Kang, Z., Hwang, K. C. & Rogers, J. A. 2011 An analytical model of strain isolation for stretchable and flexible electronics. *Appl. Phys. Lett.* **98**, 061902.

Chopin, J., Vella, D. & Boudaoud, A. 2008 The liquid blister test. *Proc. R. Soc. A* **464**, 2887–2906.

Chowdhury, S., Ahmadi, M. & Miller, W. 2005 A closed-form model for the pull-in voltage of electrostatically actuated cantilever beams. *J. Micromech. Microeng.* **15** (4), 756.

Cohen, A. E. & Mahadevan, L. 2003 Kinks, rings, and rackets in filamentous structures. *Proc. Natl. Acad. Sci. USA* **100** (21), 12141.

Conti, S. & Maggi, F. 2008 Confining thin elastic sheets and folding paper. *Arch. Ration. Mech. An.* **187** (1), 1–48.

Cotterell, B. & Chen, Z. 2000 Buckling and cracking of thin films on compliant substrates under compression. *Int. J. Fracture* **104** (2), 169–179.

Dadgour, H., Cassell, A. & Banerjee, K. 2008 Scaling and variability analysis of cnt-based nems devices and circuits with implications for process design. In *Electron Devices Meeting, 2008*, pp. 1–4. IEEE.

De Boer, M. & Michalske, T. 1999 Accurate method for determining adhesion of cantilever beams. *J. Appl. Phys.* **86** (2), 817–827.

De Gennes, P., Brochard-Wyart, F. & Quéré, D. 2003 *Capillarity and wetting phenomena: drops, bubbles, pearls, waves*. Springer.

Dequesnes, M., Rotkin, S. & Aluru, N. 2002 Calculation of pull-in voltages for carbon-nanotube-based nanoelectromechanical switches. *Nanotechnology* **13** (1), 120.

Diamant, H. & Witten, T. 2011 Compression induced folding of a sheet: An integrable system. *Phys. Rev. Lett.* **107** (16), 164302.

Diamant, H. & Witten, T. A. 2010 Instability of infinitesimal wrinkles against folding. *arxiv:* p. 1009.2487.

Diamant, H., Witten, T. A., Ege, C., Gopal, A. & Lee, K. Y. C. 2001 Topography and instability of monolayers near domain boundaries. *Phys. Rev. E* **63** (6), 061602.

Domokos, G., Fraser, W. B. & Szeberényi, I. 2003 Symmetry-breaking bifurcations of the uplifted elastic strip. *Physica D: Nonlinear Phenomena* **185** (2), 67–77.

Ebata, Y., Croll, A. B. & Crosby, A. J. 2012 Wrinkling and strain localizations in polymer thin films. *Soft Matter* pp. 9086–9091.

Euler, L. 1744 *Methodus inveniendi lineas curvas*. Bousquet.

Evans, A. A. & Lauga, E. 2009 Adhesion transition of flexible sheets. *Phys. Rev. E* **79**, 066116.

Faulhaber, S., Mercer, C., Moon, M. W., Hutchinson, J. W. & Evans, A. G. 2006 Buckling delamination in compressed multilayers on curved substrates with accompanying ridge cracks. *J. Mech. Phys. Solids* **54** (5), 1004–1028.

Gao, W. & Huang, R. 2011 Effect of surface roughness on adhesion of graphene membranes. *J. Phys. D: Appl. Phys.* **44**, 452001.

Gelfand, I. M. & Fomin, S. V. 2000 *Calculus of Variations*. Dover, New York.

Gioia, G. & Ortiz, M. 1997 Delamination of compressed thin films. *Adv. Appl. Mech.* **33**, 119–192.

Giovannetti, G., Khomyakov, P. A., Brocks, G., Karpan, V. M., Van den Brink, J. & Kelly, P. J. 2008 Doping graphene with metal contacts. *Phys. Rev. Lett.* **101** (2), 26803.

Glassmaker, N. J. & Hui, C. Y. 2004 Elastica solution for a nanotube formed by self-adhesion of a folded thin film. *J. Appl. Phys.* **96**, 3429.

Gorthi, S., Mohanty, A. & Chatterjee, A. 2006 Cantilever beam electrostatic mems actuators beyond pull-in. *J. Micromech. Microeng.* **16** (9), 1800.

Greve, R. & Blatter, H. 2009 *Dynamics of ice sheets and glaciers*. Springer.

Groenewold, J. 2001 Wrinkling of plates coupled with soft elastic media. *Physica A* **298**, 32–45.

Hawkes, E., An, B., Benbernou, N., Tanaka, H., Kim, S., Demaine, E., Rus, D. & Wood, R. 2010 Programmable matter by folding. *Proc. Natl. Acad. Sci. USA* **107** (28), 12441–12445.

Horiuchi, S., Gotou, T., Fujiwara, M., Asaka, T., Yokosawa, T. & Matsui, Y. 2004 Single graphene sheet detected in a carbon nanofilm. *Appl. Phys. Lett.* **84** (13), 2403–2405.

Huang, R. 2011 Graphene: Show of adhesive strength. *Nature Nanotech.* **6** (9), 537.

Huang, R. & Suo, Z. 2002 Wrinkling of a compressed elastic film on a viscous layer. *J. Appl. Phys.* **91** (3), 1135 –1142.

Hutchinson, J. W. & Suo, Z. 1992 Mixed mode cracking in layered materials. *Adv. Appl. Mech.* **29** (63), 191.

Israelachvili, J. N. 1992 *Intermolecular and Surface Forces*. Academic, London.

Jensen, B., Huang, K., Chow, L. & Kurabayashi, K. 2005 Adhesion effects on contact opening dynamics in micromachined switches. *J. Appl. Phys.* **97** (10), 103535.

Jensen, H. M. 1991 The blister test for interface toughness measurement. *Eng. Fract. Mech.* **40**, 475–486.

Jensen, H. M. 1998 Analysis of mode mixity in blister tests. *Int. J. Fracture* **94**, 79–88.

Jiang, H., Khang, D., Song, J., Sun, Y., Huang, Y. & Rogers, J. 2007*a* Finite deformation mechanics in buckled thin films on compliant supports. *Proc. Natl. Acad. Sci. USA* **104** (40), 15607–15612.

Jiang, H., Sun, Y., Rogers, J. & Huang, Y. 2007*b* Mechanics of precisely controlled thin film buckling on elastomeric substrate. *Appl. Phys. Lett.* **90** (13), 133119–133119.

Kendall, K. 1973 The Shapes of Peeling Solid Films. *J. Adhesion* **5** (2), 105–117.

Khang, D. Y., Rogers, J. A. & Lee, H. H. 2009 Mechanical buckling: mechanics, metrology, and stretchable electronics. *Adv. Funct. Mater.* **19** (10), 1526–1536.

Kim, E.-A. & Castro Neto, A. H. 2008 Graphene as an electronic membrane. *EPL* **84**, 57007.

Kinaret, J., Nord, T. & Viefers, S. 2003 A carbon-nanotube-based nanorelay. *Appl. Phys. Lett.* **82** (8), 1287–1289.

Koenig, S. P., Boddeti, N. G., Dunn, M. L. & Bunch, J. S. 2011 Ultrastrong adhesion of graphene membranes. *Nature Nanotech.* **6** (9), 543–546.

Kolinski, J. M., Aussillous, P. & Mahadevan, L. 2009 Shape and motion of a ruck in a rug. *Phys. Rev. Lett.* **103**, 174302.

Kusminskiy, S. V., Campbell, D. K., Neto, A. H. C. & Guinea, F. 2011 Pinning of a two-dimensional membrane on top of a patterned substrate: The case of graphene. *Phys. Rev. B* **83** (16), 165405.

Landau, L. D. & Lifschitz, E. M. 1970 *The Theory of Elasticity*. Pergamon.

Leahy, B. D., Pocivavsek, L., Meron, M., Lam, K.-L., Salas, D., Viccaro, P. J., Lee, K. Y. C. & Lin, B. 2010 Geometric stability and elastic response of a supported nanoparticle film. *Phys. Rev. Lett.* **105**, 058301.

Lee, C., Wei, X., Kysar, J. W. & Hone, J. 2008 Measurement of the elastic properties and intrinsic strength of monolayer graphene. *Science* **321**, 385–388.

Levien, R. 2008 The Elastica: A mathematical history. *Tech. Rep.*. EECS Department, University of California, Berkeley.

Lew, V. L. 2011 Malaria: Surprising Mechanism of Merozoite Egress Revealed. *Current Biology* **21** (9), R314–R316.

Li, Z., Cheng, Z., Wang, R., Li, Q. & Fang, Y. 2009 Spontaneous formation of nanostructures in graphene. *Nano Lett.* **9** (10), 3599–3602.

Lipp, M. M., Lee, K. Y. C., Takamoto, D. Y., Zasadzinski, J. A. & Waring, A. J. 1998 Coexistence of buckled and flat monolayers. *Phys. Rev. Lett.* **81**, 1650–1653.

Loh, O. & Espinosa, H. 2012 Nanoelectromechanical contact switches. *Nature Nanotech.* **7** (5), 283–295.

Loh, O., Wei, X., Ke, C., Sullivan, J. & Espinosa, H. 2011 Robust carbon-nanotube-based nano-electromechanical devices: Understanding and eliminating prevalent failure modes using alternative electrode materials. *small* **7** (1), 79–86.

Love, A. E. H. 1944 *A Treatise on the Mathematical Theory of Elasticity*. Dover, New York.

Lundgren, P. 2012 Characterization of a nanoelectromechanical switch. *www.chalmers.se /mc2/EN/education/degree-project/characterization* .

Ma, Z. 2011 An electronic second skin. *Science* **333** (6044), 830–831.

Mabrouk, E., Cuvelier, D., Brochard-Wyart, F., Nassoy, P. & Li, M. H. 2009 Bursting of sensitive polymersomes induced by curling. *Proc. Natl. Acad. Sci. USA* **106** (18), 7294–7298.

Majidi, C. 2007 Remarks on formulating an adhesion problem using Euler's elastica (draft). *Mech. Res. Comm.* **34** (1), 85–90.

Mansfield, E. H. 1989 *The Bending and Stretching of Plates*. Cambridge University Press.

Mastrangelo, C. 1997 Adhesion-related failure mechanisms in micromechanical devices. *Tribology Lett.* **3** (3), 223–238.

Mastrangelo, C. & Hsu, C. 1992 A simple experimental technique for the measurement of the work of adhesion of microstructures. In *Hilton Head*, pp. 208–212. IEEE.

Mastrangelo, C. & Hsu, C. 1993 Mechanical stability and adhesion of microstructures under capillary forces. i. basic theory. *J. Microelectromech. S.* **2** (1), 33–43.

Maugis, D. 1992 Adhesion of spheres: The JKR-DMT transition using a dugdale model. *J. Coll. Interface Sci.* **150** (1), 243–269.

Maupertuis, P. 1744 1744 accord de différentes lois de la nature qui avaient jusquici paru incompatibles. *Mém. As. Sc. Paris* **417**.

Mei, H., Huang, R., Chung, J. Y., Stafford, C. M. & Yu, H.-H. 2007 Buckling modes of elastic thin films on elastic substrates. *Appl. Phys. Lett.* **90**, 151902.

Meyer, J., Geim, A., Katsnelson, M., Novoselov, K., Booth, T. & Roth, S. 2007 The structure of suspended graphene sheets. *Nature* **446** (7131), 60–63.

Obreimoff, J. W. 1930 The splitting strength of mica. *Proc. R. Soc. A* **127** (805), 290–297.

Olver, F. W., Lozier, D. W., Boisvert, R. F. & Clark, C. W. 2010 *NIST Handbook of Mathematical Functions*, 1st edn. Cambridge University Press.

Osterberg, P. & Senturia, S. 1997 M-test: A test chip for mems material property measurement using electrostatically actuated test structures. *J. Microelectromech. S.* **6** (2), 107–118.

Oyharcabal, X. & Frisch, T. 2005 Peeling off an elastica from a smooth attractive substrate. *Phys. Rev. E* **71** (3), 036611.

Palasantzas, G. 2006 Capillary condensation and quantum vacuum effects on the pull-in voltage of electrostatic switches with self-affine rough plates. *J. Appl. Phys.* **100** (5), 054503.

Park, S., Xiong, Y., Kim, R., Elvikis, P., Meitl, M., Kim, D., Wu, J., Yoon, J., Yu, C., Liu, Z. *et al.* 2009 Printed assemblies of inorganic light-emitting diodes for deformable and semitransparent displays. *Science* **325** (5943), 977–981.

Parry, G., Colin, J., Coupeau, C., Foucher, F., Cimetière, A. & Grilhé, J. 2005 Effect of substrate compliance on the global unilateral post-buckling of coatings: AFM observations and finite element calculations. *Acta Mater.* **53**, 441–447.

von Payer, J. 1876 *The Austro-Hungarian North Pole Expedition of 1869 to 1874", Vienna, 1876*. Vienna.

Pocivavsek, L., Dellsy, R., Kern, A., Johnson, S., Lin, B., Lee, K. Y. C. & Cerda, E. 2008 Stress and fold localization in thin elastic membranes. *Science* **320**, 912.

Poot, M. & van der Zant, H. S. J. 2008 Nanomechanical properties of few-layer graphene membranes. *Appl. Phys. Lett.* **92**, 063111.

Ramberg, H. & Stephansson, O. 1964 Compression of floating elastic and viscous plates affected by gravity, a basis for discussing crustal buckling. *Tectonophysics* **1**, 101–120.

Ramezani, A., Alasty, A. & Akbari, J. 2007 Closed-form approximation and numerical validation of the influence of van der waals force on electrostatic cantilevers at nano-scale separations. *Nanotechnology* **19** (1), 015501.

Reis, P. M., Corson, F., Boudaoud, A. & Roman, B. 2009 Localization through surface folding in solid foams under compression. *Phys. Rev. Lett.* **103**, 045501.

Ribe, N. 2009 Bending mechanics and mode selection in free subduction: A thin-sheet analysis. *Geophys. J. Int.* **180** (2), 559–576.

Rogers, J. & Huang, Y. 2009 A curvy, stretchy future for electronics. *Proc. Natl. Acad. Sci. USA* **106** (27), 10875–10876.

Rogers, J. A., Someya, T. & Huang, Y. 2010 Materials and mechanics for stretchable electronics. *Science* **327**, 1603–1607.

Rotkin, S. 2009 Nanotube mems: Modeling extreme nanoscale devices. In *Proc. of SPIE*, pp. 731806–1. SPIE.

Ru, C. 2000 Effective bending stiffness of carbon nanotubes. *Phys. Rev. B* **62** (15), 9973.

Scharfenberg, S., Mansukhani, N., Chialvo, C., Weaver, R. L. & Mason, N. 2012 Observation of a snap-through instability in graphene. *Appl. Phys. Lett.* **100**, 021910.

Schniepp, H. C., Kudin, K. N., Li, J. L., Prudhomme, R. K., Car, R., Saville, D. A. & Aksay, I. A. 2008 Bending properties of single functionalized graphene sheets probed by atomic force microscopy. *ACS nano* **2** (12), 2577–2584.

Schwesig, C., Poupyrev, I. & Mori, E. 2004 Gummi: a bendable computer. In *Proceedings of the SIGCHI conference on Human factors in computing systems*, pp. 263–270. ACM.

Sen, D., Novoselov, K., Reis, P. & Buehler, M. 2010 Tearing graphene sheets from adhesive substrates produces tapered nanoribbons. *small* **6** (10), 1108–1116.

Shin, Y. J., Stromberg, R., Nay, R., Huang, H., Wee, A. T., Yang, H. & Bhatia, C. S. 2011 Frictional characteristics of exfoliated and epitaxial graphene. *Carbon* **49** (12), 4070 – 4073.

Shioyama, H. 2001 Cleavage of graphite to graphene. *J. Mat. Sci. Lett.* **20** (6), 499–500.

Skotheim, J. & Mahadevan, L. 2004 Soft lubrication. *Phys. Rev. Lett.* **92** (24), 245509.

van Spengen, W., Puers, R. & De Wolf, I. 2002 A physical model to predict stiction in mems. *J. Micromech. Microeng.* **12** (5), 702.

Stafford, C. M., Harrison, C., Beers, K. L., Karim, A., Amis, E. J., Vanlandingham, M., Kim, H.-C., Volksen, W., Miller, R. D. & Simonyi, E. E. 2004

A buckling-based metrology for measuring the elastic moduli of polymeric thin films. *Nature Mater.* **3**, 545–550.

Stuart, I. M. 1966 A loop test for bending length and rigidity. *Brit. J. Appl. Phys.* **17**, 1215–1220.

Style, R. W. & Worster, M. G. 2005 Surface transport in premelted films with application to grain-boundary grooving. *Phys. Rev. Lett.* **95**, 176102.

Sun, Y., Choi, W. M., Jiang, H., Huang, Y. Y. & Rogers, J. A. 2006 Controlled buckling of semiconductor nanoribbons for stretchable electronics. *Nature Nanotech.* **1**, 201–207.

Timoshenko, S. & Goodier, J. 1970 Theory of elasticity. *McGraw-Hill, New York* .

Van Spengen, W., Puers, R. & De Wolf, I. 2003 The prediction of stiction failures in mems. *IEEE Trans. Device Mater. Rel.* **3** (4), 167–172.

Vella, D. 2007 *The fluid mechanics of floating and sinking*. PhD Thesis, University of Cambridge.

Vella, D., Aussillous, P. & Mahadevan, L. 2004 Elasticity of an interfacial particle raft. *Europhys. Lett.* **68**, 212–218.

Vella, D., Bico, J., Boudaoud, A., Roman, B. & Reis, P. M. 2009*a* Macroscopic delamination of thin films from soft substrates. *Proc. Natl. Acad. Sci. USA* **106**, 10901–10906.

Vella, D., Boudaoud, A. & Adda-Bedia, M. 2009*b* Statics and inertial dynamics of a ruck in a rug. *Phys. Rev. Lett.* **103**, 174301.

Viculis, L., Mack, J. & Kaner, R. 2003 A chemical route to carbon nanoscrolls. *Science* **299** (5611), 1361.

Wagner, T. J. W. & Vella, D. 2011 Floating carpets and the delamination of elastic sheets. *Phys. Rev. Lett.* **107**, 044301.

Wagner, T. J. W. & Vella, D. 2012 The sensitivity of graphene snap-through to substrate geometry. *Appl. Phys. Lett.* **100** (23), 233111.

Wagner, T. J. W. & Vella, D. 2013 The 'Sticky Elastica': delamination blisters beyond small deformations. *Soft Matter* **9**, 1025–1030.

Wan, K. & Lim, S. 1998 The bending to stretching transition of a pressurized blister test. *Int. J. Fracture* **92** (4), 43–47.

Wan, K. T. 1999 Fracture mechanics of a shaft-loaded blister test–transition from a bending plate to a stretching membrane. *J. Adhes.* **70** (3-4), 209–219.

Wang, C. Y. 1986 A critical review of the heavy elastica. *Int. J. Mech. Sci.* **28**, 549–559.

Wang, S., Xiao, J., Song, J., Ko, H. C., Hwang, K.-C., Huang, Y. & Rogers, J. A. 2010 Mechanics of curvilinear electronics. *Soft Matter* **6**, 5757–5763.

Wang, S., Zhang, Y., Abidi, N. & Cabrales, L. 2009 Wettability and surface free energy of graphene films. *Langmuir* **25** (18), 11078–11081. PMID: 19735153.

Wong, W. & Salleo, A. 2009 *Flexible electronics: materials and applications*. Springer.

Yin, Z. & Ya-pu, Z. 2004 Static study of cantilever beam stiction under electrostatic force influence. *Acta Mech. Solida Sin.* **17** (2), 104–112.

Yu, H.-H. & Hutchinson, J. W. 2002 Influence of substrate compliance on buckling delamination of thin films. *Int. J. Fracture* **113**, 39–55.

Yu, Y., Nakano, M. & Ikeda, T. 2003 Directed bending of a polymer film by light. *Nature* **425** (6954), 145.

Zhang, Z. & Li, T. 2011 Determining graphene adhesion via substrate-regulated morphology of graphene. *J. Appl. Phys.* **110**, 083526.

Zong, Z., Chen, C., Dokmeci, M. & Wan, K. 2010 Direct measurement of graphene adhesion on silicon surface by intercalation of nanoparticles. *J. App. Phys.* **107** (2), 026104.